

Earth as an Exoplanet

Tyler D. Robinson

Northern Arizona University

Christopher T. Reinhard

Georgia Institute of Technology

Earth is the only planet known to harbor life and, as a result, the search for habitable and inhabited planets beyond the Solar System commonly focuses on analogs to our planet. However, Earth’s atmosphere and surface environment have evolved substantially in the last 4.5 billion years. A combination of *in situ* geological and biogeochemical modeling studies of our planet have provided glimpses of environments that, while technically belonging to our Earth, are seemingly alien worlds. For modern Earth, observations from ground-based facilities, satellites, and spacecraft have yielded a rich collection of data that can be used to effectively view our planet within the context of exoplanet characterization. Application of planetary and exoplanetary remote sensing techniques to these datasets then enables the development of approaches for detecting signatures of habitability and life on other worlds. In addition, an array of models have been used to simulate exoplanet-like datasets for the distant Earth, thereby providing insights that are often complementary to those from existing observations. Understanding the myriad ways Earth has been habitable and inhabited, coupled with remote sensing approaches honed on the distant Earth, provides a key guide to recognizing potentially life-bearing environments in other planetary systems.

Look again at that dot. That’s here. That’s home. That’s us. [...] [E]very saint and sinner in the history of our species lived there — on a mote of dust suspended in a sunbeam. - Carl Sagan

1. INTRODUCTION

The quest for both habitable and inhabited worlds beyond Earth is key to understanding the potential distribution of life in the Universe. This ongoing search seeks to answer profound questions: Are we alone? How unique is Earth? Should the hunt for life beyond Earth uncover a multitude of habitable worlds and few (if any) inhabited ones, humanity would begin to understand just how lonely and fragile our situation is. On the other hand, if our hunt yields a true diversity of inhabited worlds, then we would learn something fundamental about the tenacity of life in the cosmos.

But how will we recognize a distant habitable world, and how would we know if this environment hosts some form of life? A key opportunity for understanding the remote characterization of habitability and life comes from studying our own planet — Earth will always be our best example of a habitable and inhabited world. Thus, by studying our planet within the context of exoplanet exploration and characterization, we develop ideas, approaches, and tools suitable for remotely detecting the signs of (near) global surface habitability and a vigorous planet-wide biosphere. While habitable exoplanets are unlikely to look exactly like Earth, these worlds will probably share some important characteristics with our own, including the presence of oceans, clouds, surface inhomogeneities, and, potentially, life. Studying globally-averaged observations of Earth within the context of remote sensing therefore provides insights into the ideal

measurements to identify planetary habitability from data-limited exoplanet observations.

Of course, Earth is not a static environment. Life emerged on our planet into an environment completely unlike the Earth we understand today. The subsequent evolution of our planet — an intimate coupling between life and geochemical processes — produced worlds seemingly alien to modern Earth. Ranging from ice-covered “Snowball Earth” scenarios to the likely oxygen-free and, potentially, intermittently hazy atmosphere of the Archean (3.8–2.5 giga-annum [Ga]), each evolutionary stage of our planet offers a unique opportunity to understand habitable, life-bearing worlds distinct from the present Earth.

The chapter presented here summarizes studies of Earth within the context of exoplanet characterization. Following a brief synopsis of the current state of exoplanet science, we review our understanding of the evolution of Earth, and its associated appearance, over the last four billion years. Then, using this understanding of Earth through time, we review how key remotely-detectable biosignatures for our planet may have changed over geological timescales. We then shift our emphasis to modern Earth, where existing observational datasets and modeling tools that can be used to explore ideas related to characterizing Earth-like planets from a distance. Finally, we present an overview of what has been learned by studying Earth as an exoplanet, summarizing approaches to remote characterization of potentially habitable or inhabited worlds. For further reading, we note

that an entire book on studies of the distant Earth has been published by Vázquez et al. (2010).

1.1. Current State of Exoplanet Science

Following the first detection of an exoplanet around a Sun-like star (Mayor & Queloz 1995) and of an exoplanet atmosphere (Charbonneau et al. 2002) over a decade ago, the field of exoplanetary science has been marked by two clear trends — the steady discovery of increasingly smaller worlds on longer-period orbits, and the ever-increasing quality of observational data suitable for characterizing worlds around other stars. Due to advances in exoplanet detection using a variety of techniques, we now know that, on average, every star in the Milky Way galaxy hosts at least one exoplanet (Cassan et al. 2012). Furthermore, due in large part to the success of the *Kepler* mission (Borucki et al. 2010), we understand that occurrence rates of potentially Earth-like worlds orbiting within the Habitable Zone of Main Sequence stars are relatively large, with estimates spanning roughly 10–50% (Dressing & Charbonneau 2013; Petigura et al. 2013; Batalha 2014; Foreman-Mackey et al. 2014; Burke et al. 2015; Dressing & Charbonneau 2015; Kopparapu et al. 2018). Excitingly, and especially for low-mass stellar hosts, surveys have revealed a number of nearby potentially Earth-like exoplanets, such as Proxima Centauri b (Anglada-Escudé et al. 2016) or the worlds in the TRAPPIST-1 system (Gillon et al. 2016, 2017).

The subsequent characterization of exoplanet atmospheres has largely been accomplished using transit and/or secondary eclipse spectroscopy (for a review, see Kreidberg 2018). The former relies on the wavelength-dependent transmittance of an exoplanet atmosphere (Seager & Saselov 2000; Brown 2001; Hubbard et al. 2001), which causes a transiting world to block more (for lower transmittance) or less (for higher transmittance) light when crossing the disk of its host. By comparison, secondary eclipse spectroscopy measures the planet-to-star flux ratio by observing the combined star and exoplanet spectrum prior to the planet disappearing behind its host star (i.e., secondary eclipse). As with any burgeoning field, some findings related to exoplanet atmospheres remain controversial or have undergone substantial revision (Line et al. 2014; Hansen et al. 2014; Diamond-Lowe et al. 2014). Nevertheless, using these techniques astronomers have probed the atmospheres of a striking variety of exoplanets, spanning so-called hot Jupiters (Grillmair et al. 2008; Swain et al. 2008; Pont et al. 2008; Swain et al. 2009; Sing et al. 2009; Madhusudhan & Seager 2009), as well as mini-Neptunes and super-Earths (Stevenson et al. 2010; Bean et al. 2010; Line et al. 2013; Kreidberg et al. 2014; Knutson et al. 2014a,b; Ehrenreich et al. 2014; Fraine et al. 2014; Sing et al. 2016; Stevenson 2016; de Wit et al. 2018).

Unfortunately, transit or secondary eclipse spectroscopy is not well-suited to studying the atmospheres of potentially

Earth-like planets orbiting within the Habitable Zone of their Sun-like¹ hosts, due to the long orbital periods, small transit probabilities, and low signal sizes for such worlds. Here, direct (or high-contrast) imaging will likely be the leading observational approach, and, as a result, the material below focuses primarily on directly observing Earth (in both reflected light and thermal emission). For exoplanets, direct imaging involves blocking the light of a bright central host star in order to resolve and observe faint companions to that star (Traub & Oppenheimer 2010). Both internal and external occulting technologies are under active study (Guyon et al. 2006; Cash et al. 2007; Shaklan et al. 2010; Mawet et al. 2012), and ground-based telescopes equipped with coronagraphs already enable the characterization of hot gas giant exoplanets orbiting young, nearby stars (Marois et al. 2008; Skemer et al. 2012; Macintosh et al. 2015).

1.2. The Future of Rocky Exoplanets

A number of planned or under-study missions will improve and expand our ability to characterize exoplanet atmospheres and surfaces. Foremost among these is NASA’s *James Webb Space Telescope (JWST)* (Gardner et al. 2006), which is expected to provide high-quality transit and secondary eclipse spectra of many tens of targets over the duration its designed five year mission (Beichman et al. 2014). Some of these observations will probe lower-mass, potentially rocky exoplanets (Deming et al. 2009; Batalha et al. 2015). Critically, *JWST* may even be capable of characterizing temperate Earth-sized planets orbiting low-mass stars (Kaltenegger & Traub 2009; Cowan et al. 2015; Barstow et al. 2016), though the ability to conduct such studies depends largely on the behavior and size of systematic noise sources (Greene et al. 2016).

Following *JWST*, NASA will launch the Wide-Field InfraRed Survey Telescope (*WFIRST*; Spergel et al. 2013). It is anticipated that *WFIRST* will be equipped with a Coronagraphic Instrument (CGI) capable of visible-light imaging and, potentially, spectroscopy or spectro-photometry of exoplanets (Noecker et al. 2016). Key outcomes of this mission will include a demonstration of high-precision coronagraphy in space, as well as the study of a small handful of cool, gas giant exoplanets (Marley et al. 2014; Hu 2014; Burrows 2014; Lupu et al. 2016; Traub et al. 2016; Nayak et al. 2017). However, the planned capabilities of *WFIRST/CGI* will make observations of Earth-like planets extremely unlikely (Robinson et al. 2016).

Exoplanet direct imaging missions that could build on the technological successes of *WFIRST* are already un-

¹“Sun-like” typically refers to main sequence stars with spectral type F, G, or K. Such stars range from 30% larger and 6× more luminous than our Sun down to 30% smaller and 13× less luminous than the Sun. Sun-like stars are often contrasted to “late type” stars, which are red, cool main sequence M stars that can be smaller than 10% the size of our Sun and can have luminosities as small as 1–2% that of the Sun.

der investigation. Included here are the *WFIRST* starshade rendezvous concept (Seager et al. 2015), the Habitable Exoplanet (HabEx) imaging mission (Mennesson et al. 2016; Gaudi et al. 2018), and the Large Ultraviolet-Visible-Infrared (LUVOIR) explorer (Peterson et al. 2017; Roberge & Moustakas 2018). While the scope and capabilities of these mission concepts are varied (Stark et al. 2016), a central goal unites these designs — to detect and characterize Pale Blue Dots around our nearest stellar neighbors.

2. EARTH AS AN EVOLVING EXOPLANET

Earth, however, has not always been the Pale Blue Dot we see today. Indeed, the Earth system has evolved considerably over time (Figure 1). These changes have in turn impacted both the habitability of Earth surface environments (e.g., Kasting & Catling 2003) and the remote detectability of Earth’s biosphere (Kaltenegger et al. 2007; Meadows 2008; Reinhard et al. 2017a; Rugheimer & Kaltenegger 2018). In particular, the atmospheric abundances of almost all potential biosignature gases (e.g., CH_4 , O_2 , O_3 , N_2O , CO_2) have changed by many orders of magnitude throughout Earth’s history. The timing and magnitude of these changes have been controlled by often complex interactions between biological, geologic, and stellar factors. At the same time, Earth’s climate system and surface habitability have changed significantly, as influenced by both long-term trends in solar energy flux, catastrophic climate destabilization during low-latitude “Snowball Earth” glaciations, and major impact events.

Despite these dramatic changes, all life on Earth appears to share a single origin that is perhaps nearly as ancient as Earth itself (Fox et al. 1980; Hedges 2002). Earth’s history thus allows us to explore the long-term evolutionary factors controlling the production and maintenance of remotely detectable signatures of habitability and life against the backdrop of a continuously inhabited planet. Fully illuminating this history requires integration of geologic observations, geochemical data, and constraints from theoretical models — and provides a unique opportunity to develop predictive frameworks that can be leveraged in the search for living planets beyond Earth.

In this section, our focus is on observations and models aimed at constraining surface habitability and atmospheric composition through time on Earth, with a particular eye toward key habitability indicators and atmospheric biosignatures. Critically, data and models can be used to constrain the surface habitability and atmospheric composition of Earth through time, enabling an assessment of the strength of different biosignature features and habitability markers and how these may change through planetary evolution. In addition, Earth’s geologic history provides a series of empirical tests of our understanding of Earth-like planets as integrated systems — with different periods of Earth’s evolutionary history serving as analogs for alien, yet

habitable, worlds for which we have biological and geological constraints.

2.1. Geological Constraints on Evolving Climate

Understanding the evolution of Earth’s climate system is critical for diagnosing how potential observational discriminants of Earth’s habitability may have changed with time. Interestingly, with some notable exceptions (see below) Earth’s climate appears to have been clement for the vast majority of its history. For instance, isotopic evidence from the oldest minerals on Earth suggest the presence of liquid water at Earth’s surface by 4.3 billion years ago (Ga) (Mojzsis et al. 2001; Ushikubo et al. 2008), and a consistent if fragmentary marine sedimentary rock record attests to a large-scale fluid-mediated rock cycle for the last 3.8 billion years (e.g., Rosing et al. 1996). Other lines of evidence (Knauth & Epstein 1976; Robert & Chaussidon 2006; Gaucher et al. 2008) have been used to suggest that surface temperatures during much of the Archean Eon (3.8–2.5 Ga) were hot, perhaps as high as 70°C. More recent estimates suggest much cooler (but still quite warm) temperatures between 25–40°C (Hren et al. 2009; Blake et al. 2010).

Geologic evidence for glacial deposits can provide first-order information about evolving climate, particularly if the approximate location and altitude of glacial activity can be constrained. The most well-established sedimentary evidence for early glacial activity near sea level is found in the Mozaan Group, South Africa at ~2.9 Ga (Young et al. 1998). Given existing paleolatitude constraints of around 45–50° (Kopp et al. 2005), these deposits suggest a climate similar to or colder than that of the Pleistocene Earth (a relatively cold epoch of repeated glaciations spanning 2.59–0.012 mega-annum [Ma]). More recently, sedimentological evidence of glacial activity has been reported from the ~3.5 Ga Overwacht Group, Barberton Greenstone Belt, South Africa (de Wit & Furnes 2016), although their glacial origin is less definitive than that of the Mozaan Group sediments (e.g., Viljoen & Viljoen 1969). The reconstructed paleolatitudes of these deposits are between ~20–40°, so if they are indeed glaciogenic in origin they would imply a relatively cold early Archean climate.

Firm evidence for glacial activity near sea level does not reappear until after the Archean-Proterozoic boundary, with a series of glacial deposits observed in North America (Young 2001) and South Africa (Rasmussen et al. 2013) between ~2.4 – 2.3 Ga. Glaciogenic deposits found on the Kaapval craton, South Africa, recently dated to 2.426 ± 0.003 Ga (Gumsley et al. 2017), show evidence for being deposited at low latitudes (Evans et al. 1997), leading to the suggestion that these deposits record a Paleoproterozoic “Snowball Earth” — classically envisaged as a catastrophic destabilization of the climate system during which runaway ice-albedo feedback causes the advance of ice sheets to the tropics, and a virtual shutdown of the hydrologic cycle (Budyko 1969; Sellers 1969). The temporal

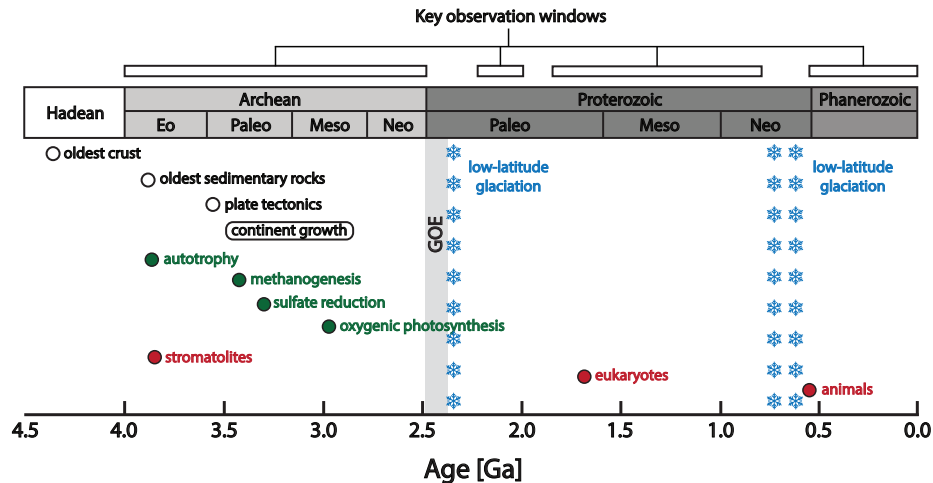


Fig. 1.— Summary timeline of geologic history for Earth, with major divisions of the geologic timescale (top) related to quantitative ages (bottom) according to billions of years before the present (Ga). Major early geologic events are shown by open white circles, including the development of the oldest crust and sedimentary rocks, the emergence of plate tectonics, and an interval of significant growth/exposure of continental crust above sea level. Filled green circles denote approximate geochemical constraints on major metabolic innovations, including carbon fixation (autotrophy), methane production, sulfate reduction, and oxygenic photosynthesis. A subset of major events from the fossil record is given by filled red circles, including the first putative stromatolites (layered sedimentary structures induced by microorganisms), the emergence of eukaryotes (large, complex cells with a membrane-bound nucleus), and the first multicellular animal fossils. Also shown are the initial oxygenation of Earth’s atmosphere — the Great Oxidation Event (GOE) — and three occurrences of unusually intense low-latitude glaciation (‘Snowball Earth’ events). Above the geologic timeline we summarize our key ‘observation windows’ examined in Figure 2 and Table 1.

correspondence between this apparently intense ice age and the initial accumulation of O_2 in Earth’s atmosphere (Figure 1) has led to the intriguing suggestion that the climate system was transiently destabilized by a sharp drop in atmospheric CH_4 attendant to rising atmospheric O_2 (Kasting 2005).

Recent evidence suggests that these intense ice ages were followed by a transient period of atmospheric oxygenation, after which the climate system appears to have been relatively stable with little firm evidence for glaciation between $\sim 1.8 - 0.8$ billion years ago (here referred to as the ‘mid-Proterozoic’). A notable exception to this comes in the form of putative glacial deposits from the Vazante Group, east-central Brazil (Azmy et al. 2008; Geboy et al. 2013), though their age is somewhat enigmatic (Geboy et al. 2013; Rodrigues et al. 2012). These deposits indicate that at least portions of the mid-Proterozoic were not entirely ice-free, but their deposition at relatively high paleolatitude (Tohver et al. 2006) renders their broader climatic implications somewhat difficult to interpret.

The close of the Proterozoic Eon (2.5–0.541 Ga) bore witness to perhaps the most severe climate perturbations in Earth’s history, the Neoproterozoic “Snowball Earth” events (Hoffman et al. 1998). Recent high-resolution geochronology delineates two major glacial episodes, the protracted Sturtian glaciation (lasting between 717–660 Ma) and the shorter Marinoan glaciation (terminating at 635 Ma), with a relatively brief interglacial period lasting less than 25 million years (Rooney et al. 2015). While un-

derstanding the intensity, dynamics, and biogeochemical impacts of these glaciations remain areas of active research [extensively reviewed in Hoffman & Schrag (2002), Pierrehumbert et al. (2011), and Hoffman et al. (2017)], it is clear that this period marks a dramatic perturbation to planetary climate and would have represented a significant and protracted shift in the remotely detectable indicators of Earth’s habitability.

The Phanerozoic Eon (e.g., the last 541 million years) has been marked by at least three large-scale ice ages (Delabroye & Vecoli 2010; Veevers & Powell 1987; Zachos et al. 2001). These events have been linked with faunal turnover and mass extinction (Raymond & Metz 2004), and in some cases reflect major milestones in the evolution of Earth’s biosphere such as the earliest colonization of the land surface by simple plant life at ~ 470 Ma (Lenton et al. 2012) and the extensive production and burial of organic matter by burgeoning terrestrial ecosystems around 300 Ma (Feulner 2017). At the same time, the most recent half-billion years of Earth’s history shows evidence for significant transient perturbations to Earth’s carbon cycle and climate system on a wide range of timescales (Zachos et al. 2008; Hönisch et al. 2012), often associated with dramatic changes to the diversity and abundance of macroscopic life (Erwin 1994; Payne et al. 2004). Nevertheless, despite large changes to carbon fluxes into and out of the ocean-atmosphere system, Phanerozoic Earth’s climate has consistently avoided the sort of catastrophic climate destabilization witnessed during the late Proterozoic.

In sum, Earth’s geologic record suggests that the establishment of a robust hydrosphere, with liquid water oceans and low-temperature aqueous weathering of exposed crust, occurred very shortly after Earth’s formation. In addition, surface temperatures have generally been stable and relatively warm for the vast majority of Earth’s history, despite long-term changes in solar insolation and dramatic changes to atmospheric composition (see below). However, this history also highlights the importance of internal feedbacks within the climate system in structuring planetary habitability on Earth (and thus the likelihood of remote detection) over time. For example, the “Snowball Earth” glaciations suggest that an Earth-like planet that spends its lifetime safely within the Habitable Zone of its host star can still undergo catastrophic climate destabilization, and that both the timing and duration of these events can be unpredictable (e.g., Rooney et al. 2015). This is in marked contrast to the regular, periodic mode of climate instability predicted for Earth-like planets near the outer edge of the Habitable Zone (Haqq-Misra et al. 2016). In addition, the contrasting timescales of the two Neoproterozoic glaciations imply a wide range of potential effects on the long-term maintenance of remotely detectable biosignatures, placing significant impetus on better understanding the large-scale biogeochemistry of “Snowball Earth” conditions (see below).

2.2. Geological Constraints on Evolving Atmospheric Chemistry

Geologic and geochemical data also provide a window into the dramatic evolution of Earth’s atmospheric chemistry, with implications for both the habitability of surface environments and the remote detectability of atmospheric biosignatures. For the last ~ 2 million years, atmospheric composition on Earth can be tracked directly by analyzing the composition of volatiles trapped in ice (Wolff & Spahn 2007). Prior to this, biogeochemists and planetary scientists seeking to reconstruct the composition of Earth’s atmosphere must rely on some form of ‘proxy’ — an indirect indicator of atmospheric composition. For example, in many species of plant the spatial density of cells on the leaf that are used to exchange gases with the environment — ‘stomata’ — scales coherently with the abundance of CO_2 in the growth environment (e.g., Royer 2001). Paleobotanists can thus use the stomatal density of fossil plant leaves as a proxy for atmospheric CO_2 abundance in Earth’s past. Our focus in this chapter is on major changes to atmospheric gas species that are important for regulating global climate (e.g., CO_2 , CH_4 , N_2 , and possibly H_2) and species that are potentially promising biosignature gases (e.g., O_2 , O_3 , CH_4 , N_2O). Some species, most notably methane and organic hazes, serve dual roles as both arbiters of climate and potential biosignatures.

There are four broad temporal intervals of Earth’s evolutionary history that are relevant to our purposes: the Archean (4.0 – 2.5 Ga), the early Paleoproterozoic (more

specifically the interval between 2.2 – 2.0 Ga), the mid-Proterozoic (specifically the interval between 1.8 – 0.8 Ga), and the Phanerozoic (roughly 0.5 Ga to the present) (see Figure 1). It is important to bear in mind that these all represent extremely long periods of time, and that there is likely to be higher-order variability within each interval. Nevertheless, model-derived spectra of Earth during these key evolutionary stages demonstrate how varying atmospheric compositions have led to dramatically different spectral appearances for our planet over time (Figure 3).

2.2.1. Atmospheric Oxygen (O_2) and Methane (CH_4) on Earth Through Time

The atmospheric abundances of O_2 CH_4 on Earth have changed considerably over time (Figure 2). In particular, the abundant O_2 in Earth’s modern atmosphere is a relatively recent phenomenon — atmospheric O_2 abundance has increased over Earth’s history by many orders of magnitude, from the very low levels of the Hadean/Archean, through a period of intermediate values during the Proterozoic, eventually rising to the high levels we observe on Earth today. Because both O_2 and CH_4 are largely generated and recycled through biological processes, and are spectrally active, they both represent potentially useful atmospheric biosignatures. Levels of O_2 and CH_4 are also linked mechanistically through the redox state of Earth’s atmosphere, such that periods of Earth’s history characterized by low atmospheric O_2 tend to feature elevated atmospheric CH_4 , and vice-versa (Figure 2). In this section, we discuss the evolution of atmospheric O_2 and CH_4 on Earth as constrained by a range of geologic and geochemical indicators, with an eye toward better understanding how the detectability of Earth’s biosphere has changed over time.

Sulfur (S) isotope distributions in marine sedimentary rocks of Archean age suggest extremely low atmospheric O_2 levels, constrained to an upper limit of $\sim 10^{-6}$ bar (Farquhar et al. 2000; Pavlov & Kasting 2002) but most likely below $\sim 10^{-8}$ bar (Claire et al. 2006; Zahnle et al. 2006). These anomalies also suggest high abundance of some reducing gas for effective production of S_8 in the atmosphere, with CH_4 as the most likely candidate (Zahnle et al. 2006). More recently, coherent time-dependent changes in S isotope systematics have been tied to the transient production and breakdown of atmospheric organic hazes during the late Archean (Zerkle et al. 2012; Izon et al. 2017). Given the surface CH_4 fluxes required to maintain persistent organic hazes, their presence may serve as an effective biosignature in reducing planetary atmospheres such as that of the Archean Earth (Arney et al. 2018). This isotopic evidence for a broadly reducing, low- O_2 ocean-atmosphere system is consistent with a wide range of other geochemical and sedimentological observations (Rye & Holland 1998; Rasmussen & Buick 1999; Planavsky et al. 2010; Crowe et al. 2014).

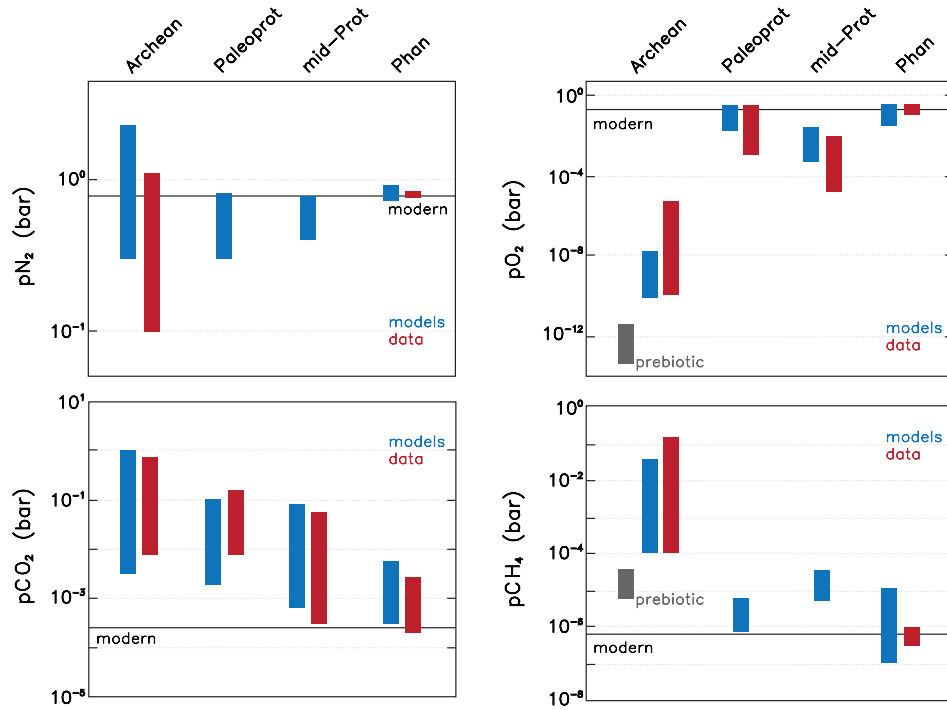


Fig. 2.— Summary of theoretical and empirical constraints on the abundances of N_2 , O_2 , CO_2 , and CH_4 in Earth's atmosphere for the four major time periods discussed in the text (Archean, Paleoproterozoic, mid-Proterozoic, and Phanerozoic). Blue bars show reconstructions from models, while red bars show inferences based on empirical data. Also shown for the Archean are model-based estimates of prebiotic O_2 and CH_4 levels (grey bars). The ranges are meant to be inclusive, and some of the variability in a given time period should be considered to arise from time-dependent variability rather than uncertainty [e.g., Olson et al. (2018b)]. Constraints are as described in Table 1.

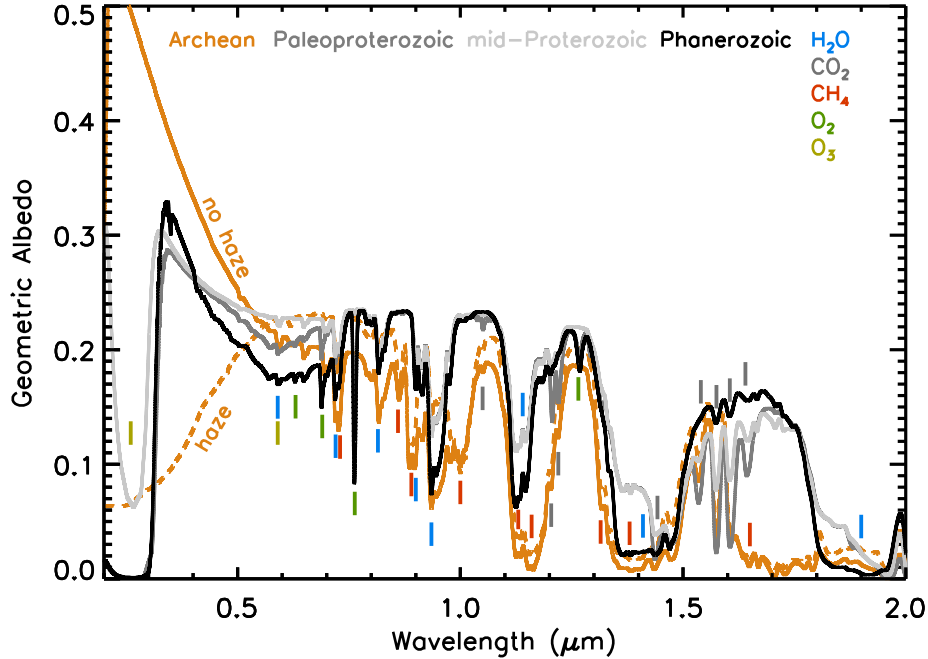


Fig. 3.— Simulated spectra of Earth at key evolutionary stages. Colors indicate time period: Archean (orange), Paleoproterozoic (dark gray), mid-Proterozoic (light gray), and Phanerozoic (black). Both hazy and haze-free Archean models are shown, and all models include fractional water cloud coverage. Key absorption features are indicated. Original sources for spectra are Arney et al. (2016, Archean), Robinson et al. (2011, Phanerozoic), and E. Schwieterman (personal communication, Paleoproterozoic and mid-Proterozoic).

Sedimentological and isotopic evidence records the initial accumulation of O_2 in Earth's atmosphere during the "Great Oxidation Event" (GOE) at ~ 2.3 billion years ago (e.g., Holland 1984, 2002; Luo et al. 2016) (Figure 1). More recently, geologic and geochemical evidence has led to the hypothesis of a protracted, but ultimately transient, period of ocean-atmosphere oxygenation following the GOE (reviewed in Lyons et al. 2014). In particular, marine sedimentary carbonate rocks record an extended interval of ^{13}C enrichment — the so-called 'Lomagundi Event' (Karhu & Holland 1996; Bekker 2001; Melezhik et al. 2007) — which implies a massive release of O_2 to the ocean-atmosphere system according to conventional models of Earth's carbon cycle (Kump & Arthur 1999). This period also records the earliest extensive marine deposits of sulfate-bearing evaporite minerals (Schröder et al. 2008), increasingly large sulfur (S) isotope fractionations (Canfield 2005), a dramatic increase in the ratio of oxidized iron in marine shales (Bekker & Holland 2012), significant enrichments of redox-sensitive metals in anoxic marine sediments (Canfield et al. 2013; Partin et al. 2013; Reinhard et al. 2013), and the first economic phosphorite deposits (Lepland et al. 2014).

A wide range of geochemical proxies point to a subsequent return to relatively low ocean-atmosphere oxygen levels during the mid-Proterozoic, between $\sim 1.8 - 0.8$ billion years ago, perhaps to levels that would have rendered O_2 difficult to detect remotely (see Section 3). In particular, the disappearance of sulfate evaporites and large phosphorite deposits from the rock record (Schröder et al. 2008; Reinhard et al. 2017b), a drop in ferric to total iron ratios in marine shales (Bekker & Holland 2012), the S isotope systematics of marine sedimentary rocks (Planavsky et al. 2012; Scott et al. 2014), and the incomplete retention of Fe and Mn in ancient soil horizons (Zbinden et al. 1988) all point to a decrease in ocean-atmosphere oxygen levels following the Lomagundi Event. More recent geochemical observations have buttressed this view (Planavsky et al. 2014b; Cole et al. 2016; Hardisty et al. 2017; Tang et al. 2016a; Partin et al. 2013; Reinhard et al. 2013; Sheen et al. 2018; Bellefroid et al. 2018). The majority of geochemical observations are consistent with a background pO_2 value at or well below $\sim 10^{-2}$ bar (Lyons et al. 2014). However, sulfur isotopic anomalies in sedimentary rocks characteristic of the Archean do not return during this interval, suggesting that atmospheric pO_2 remained above $\sim 10^{-6}$ bar, atmospheric pCH_4 remained well below $\sim 10^{-2} - 10^{-3}$ bar, or both (e.g., Zahnle et al. 2006). Precisely quantifying atmospheric pO_2 during this period remains a significant outstanding challenge, and Archean oxygen levels, perhaps paradoxically, are perhaps better constrained than those of the Proterozoic.

The late Proterozoic bore witness to significant changes to ocean-atmosphere redox, before, during, and after the "Snowball Earth" glaciation events (reviewed in Lyons et al. 2014). Indeed, there is some evidence for a shift in ocean-atmosphere redox immediately preceding the first low-latitude glaciation (Planavsky et al. 2014b; Thomson

et al. 2015), implicating time-dependent changes to Earth's oxygen cycle as a potentially important component of climate destabilization in both the Paleoproterozoic and Neoproterozoic (Figure 1). The ultimate result of these upheavals appears to have been an oxygenation of the ocean-atmosphere system to a degree approaching that of the modern Earth. For most of Phanerozoic time (541 million years ago to the present), atmospheric pO_2 appears to have remained within the fire window² of between $\sim 0.15 - 0.35$ bar (Belcher & McElwain 2008; Glasspool & Scott 2010), although atmospheric pO_2 during the Paleozoic prior to the rise of land plants is somewhat poorly constrained and may have been below 0.1 bar (e.g., Bergman 2004; Lenton et al. 2018). However, essentially all available geologic, geochemical, and biological observations are consistent with a well-oxygenated ocean-atmosphere system for the last 500–600 million years (Lyons et al. 2014).

2.2.2. Atmospheric Carbon Dioxide (CO_2) on Earth Through Time

The abundance of CO_2 in Earth's atmosphere has also changed by orders of magnitude throughout Earth's history (Figure 2). These changes are deeply intertwined with Earth's overall habitability through the carbonate-silicate cycle, or "Walker feedback" (Walker et al. 1981), which is hypothesized to regulate atmospheric CO_2 levels through temperature-dependent weathering of the silicate crust. The operation of such a feedback is central to our understanding of planetary habitability, and indeed forms the basis for the "Habitable Zone" concept (Kasting et al. 1993). Earth's history provides some evidence in favor of this framework, with atmospheric CO_2 abundance generally decreasing over time in the face of a long-term increase in solar luminosity (Figure 2). However, more precisely quantifying the strength and transient dynamics of this feedback, and the boundary conditions under which it may break down, are critical ongoing tasks for researchers with an interest in planetary habitability. In this section, we discuss geologic and geochemical constraints on atmospheric CO_2 abundance on Earth through time, while Section 2.4 below discusses models of the long-term carbon cycle and the impact of evolving atmospheric CO_2 on global climate.

Archean atmospheric pCO_2 is not very well-constrained, though all existing data are consistent with values that were elevated above those of the modern Earth, perhaps by 2–3 orders of magnitude. Mineral assemblages observed within riverine sediments provide a lower limit on atmospheric pCO_2 of roughly 10^{-3} bar at 3.2 Ga (Hessler et al. 2004), but these observations are also consistent with CO_2 levels

²The "fire window" refers to a range of atmospheric pO_2 levels that are constrained by widespread charcoal in the Phanerozoic geologic record as well as the persistence of plant life in this same record. At the lower bound of the window, burning of plant material would be rare and charcoal would not be widely produced. At the upper bound of the window, plant burning would be global and could not be extinguished (Scott & Glasspool 2006).

an order of magnitude or more higher than this. Similarly, secondary mineral assemblages in ancient soil horizons (paleosols) that formed between ~ 2.7 – 2.5 Ga have been interpreted to indicate $p\text{CO}_2$ values between $\sim 10^{-3}$ – 10^{-2} bar during the late Archean (Rye et al. 1995; Sheldon 2006). A more recent model suggests much higher Archean $p\text{CO}_2$, up to or exceeding $\sim 10^{-1}$ bar (Kanzaki & Murakami 2015), though estimates according to this method can vary over many orders of magnitude at any given time due to uncertainties in assumed soil formation timescales.

Broadly, geologic observations tend to suggest a drop in atmospheric CO_2 levels between the Paleoproterozoic and the mid-Proterozoic. Paleosols formed between 2.5–1.8 Ga yields a somewhat more consistent picture, with estimates from both of the most recent $p\text{CO}_2$ reconstruction techniques yielding values on the order of $\sim 10^{-3}$ – 10^{-2} bar (Sheldon 2006; Kanzaki & Murakami 2015), although the estimates of Kanzaki & Murakami (2015) for similarly aged paleosols are in general a factor of 2–5 higher than those of Sheldon (2006). There is only one well-studied paleosol near the Archean-Proterozoic boundary, making it difficult to establish with confidence whether significant changes in atmospheric $p\text{CO}_2$ occurred transiting the Archean-Proterozoic boundary. Moving into the mid-Proterozoic, reconstructions based on paleosols (Sheldon 2013), carbon isotopes (Kaufman & Xiao 2003), and fossils of cyanobacteria (Kah & Riding 2007) are all broadly consistent with atmospheric $p\text{CO}_2$ values on the order of $\sim 3 \times 10^{-3}$ bar, though individual estimates vary between values roughly equivalent to the modern Earth to high values of $\sim 10^{-2}$ bar.

A much wider range of potential $p\text{CO}_2$ proxies exists for the Phanerozoic, including a higher-resolution paleosol record, the carbon isotope compositions of plant and phytoplankton fossils, the density of stomata on fossilized leaves, and geochemical proxies of ocean pH (reviewed in Royer 2014). Although these approaches are all undergoing continual refinement, they generally point to a range for atmospheric $p\text{CO}_2$ during the Phanerozoic between roughly $\sim 10^{-4}$ – 10^{-3} bar, with significant time-dependent shifts associated with major biospheric innovations and changes in climate (see above). An important caveat to this record is that constraints become very patchy during early Paleozoic time (e.g., prior to round 400 million years ago), a period during which Earth system models indicate atmospheric CO_2 levels were higher than at any other time during the Phanerozoic (Berner & Kothavala, 2001). However, recent model inversions suggest that atmospheric $p\text{CO}_2$ has never been significantly above $\sim 5 \times 10^{-3}$ bar during the last 500 million years (Royer et al. 2014; Lenton et al. 2018) (see Section 2.3).

2.2.3. Atmospheric Nitrogen (N_2) on Earth Through Time

Earth’s modern atmosphere is $\sim 80\%$ molecular nitrogen (N_2) by volume. A range of geologic processes could

potentially lead to large changes in atmospheric N_2 on Earth, but the empirical trajectory of N_2 levels is poorly known at present. This is important, because on Earth the abundance of N_2 in the atmosphere largely controls overall atmospheric pressure, which can significantly impact overall atmospheric opacity to infrared radiation through pressure-induced broadening of absorption lines for greenhouse gases, linking atmospheric pressure and global surface temperature (e.g., Goldblatt et al. 2009). In addition, one of the few known mechanisms for producing an abiotic O_2 -rich planetary atmosphere, and thus a potential biosignature “false positive” for O_2 (Meadows 2018), relies on low atmospheric pressure (Wordsworth & Pierrehumbert 2014). As a result, there is strong impetus to better understand the evolutionary history of N_2 on Earth as a means to better understand the factors controlling planetary N_2 cycling on other Earth-like planets.

A current frontier in reconstructing the evolution of Earth’s atmosphere is developing constraints on atmospheric pressure, as linked most directly with changes in atmospheric N_2 abundance. As discussed in Section 2.3, mass balance calculations suggest that N_2 levels may have varied significantly from the present level of ~ 0.8 bar, with potentially non-trivial impacts on climate (Goldblatt et al. 2009). Recent approaches toward reconstructing overall atmospheric pressure have included estimating air density based on the diameter of fossilized raindrop imprints in a 2.7-billion-year-old tuff from the Ventersdorp Supergroup, South Africa (Som et al. 2012), and estimating total barometric pressure via the size distribution of vesicles in a lava flow from roughly the same age preserved in the Pilbara Craton, Australia (Som et al. 2016). The technique based on raindrop imprints implies that atmospheric pressure at 2.7 Ga was between ~ 0.5 – 2.0 bar, though placing an upper limit with this method is difficult (Kavanagh & Goldblatt 2015). The vesicle approach provides a much more stringent upper limit of around 0.5 bar. Marty et al. (2013) attempted to estimate $p\text{N}_2$ directly by analyzing the isotopic composition of nitrogen and argon in 3.5 and 3.0 billion-year-old fluids trapped in hydrothermal quartz from the Pilbara craton, Australia, deriving mixing arrays between end-member hydrothermal fluids of variable composition with a single end-member for air-saturated Archean seawater. Their analysis indicates that $p\text{N}_2$ was not significantly above ~ 0.5 – 1.0 bar during the early Archean. Nishizawa et al. (2007) provide a $p\text{N}_2$ estimate of ~ 3 bar from fluid inclusions in the same unit, but the $\text{N}_2/^{36}\text{Ar}$ values from their samples indicate that their data do not capture the low- N_2 end-member analyzed by Marty et al. (2013) and thus likely overestimate ambient $p\text{N}_2$. In any case, uncertainties in all current approaches and the fragmentary nature of the archives required for their application are such that current data are consistent with atmospheric N_2 abundance a factor of two or more above/below modern, rendering the potential climate impacts of N_2 somewhat enigmatic at present but important to consider (see below).

TABLE 1
EMPIRICAL AND THEORETICAL CONSTRAINTS ON EARTH’S EVOLVING ATMOSPHERIC COMPOSITION

Period	Case	$p\text{N}_2$ [bar]	$p\text{O}_2$ [bar]	$p\text{CO}_2$ [bar]	$p\text{CH}_4$ [bar]	Source(s)
<i>prebiotic</i>						
	model high	—	$3.0 \times 10^{-12\dagger}$	—	3.0×10^{-5}	1,2
	model low	—	$3.0 \times 10^{-14\dagger}$	—	5.0×10^{-6}	1,3
	data high	—	—	—	—	—
	data low	—	—	—	—	—
<i>Archean</i>						
	model high	2.3	2.0×10^{-8}	1.0×10^0	3.5×10^{-2}	4-12
	model low	0.3	1.0×10^{-10}	3.0×10^{-3}	1.0×10^{-4}	5-13
	data high	1.1	2.0×10^{-6}	7.0×10^{-1}	$1.4 \times 10^{-1 }$	14-16
	data low	0.1^ℓ	—	7.0×10^{-3}	1.0×10^{-4}	7,17-19
<i>Paleoproterozoic</i>						
	model high	0.8	3.0×10^{-1}	1.0×10^{-1}	5.0×10^{-6}	8-10,13,20,21
	model low	0.3	2.0×10^{-2}	2.0×10^{-3}	7.0×10^{-7}	8-10,13,21
	data high	—	3.0×10^{-1}	1.5×10^{-1}	—	16,22
	data low	—	1.0×10^{-3}	7.0×10^{-3}	—	18,22,23
<i>mid-Proterozoic</i>						
	model high	0.8	2.0×10^{-2}	8.0×10^{-2}	3.0×10^{-5}	8-10,13,24-26
	model low	0.4	6.0×10^{-4}	6.0×10^{-4}	$5.0 \times 10^{-6\zeta}$	8-10,13,25,27
	data high	—	8.0×10^{-3}	5.5×10^{-2}	—	23,28,29
	data low	—	2.0×10^{-5}	3.0×10^{-4}	—	30,31
<i>Phanerozoic</i>						
	model high	0.9	3.0×10^{-1}	5.5×10^{-3}	1.0×10^{-5}	32-36
	model low	0.7	4.0×10^{-2}	2.8×10^{-4}	1.0×10^{-7}	32-36
	data high	0.8	1.5×10^{-1}	2.8×10^{-3}	8.0×10^{-7}	37-39
	data low	0.8	3.0×10^{-1}	1.9×10^{-4}	3.5×10^{-7}	39-41

References. — ¹Haqq-Misra et al. (2011), ²Emmanuel & Ague (2007), ³Tian et al. (2011), ⁴Goldblatt et al. (2009), ⁵Claire et al. (2006), ⁶Zahnle et al. (2006), ⁷Kurzweil et al. (2013), ⁸Kasting (1987), ⁹Halevy & Bachan (2017), ¹⁰Krissansen-Totton et al. (2018), ¹¹Kharecha et al. (2005), ¹²Ozaki et al. (2018), ¹³Stüeken et al. (2016), ¹⁴Marty et al. (2013), ¹⁵Pavlov & Kasting (2002), ¹⁶Kanzaki & Murakami (2015), ¹⁷Som et al. (2016), ¹⁸Sheldon (2006), ¹⁹Driese et al. (2011), ²⁰Bachan & Kump (2015), ²¹Harada et al. (2015), ²²Bekker & Holland (2012), ²³Rye & Holland (1998), ²⁴Laakso & Schrag (2017), ²⁵Catling et al. (2007), ²⁶Zhao et al. (2018), ²⁷Olson et al. (2016), ²⁸Kaufman & Xiao (2003), ²⁹Kah & Riding (2007), ³⁰Planavsky et al. (2014b), ³¹Sheldon (2013), ³²Berner (2006), ³³Royer (2014), ³⁴Lenton et al. (2018), ³⁵Bartdorff et al. (2008), ³⁶Beerling et al. (2009), ³⁷Belcher & McElwain (2008), ³⁸Royer (2014), ³⁹Wolff & Spahn (2007), ⁴⁰Glasspool & Scott (2010), ⁴¹Galbraith & Eggleston (2017)

[†] Assumes $p\text{CO}_2 = 2$ bar.

[‡] Assumes $p\text{CO}_2 = 0.02$ bar.

^{||} Assuming data high $p\text{CO}_2$ and $\text{CH}_4/\text{CO}_2 = 0.2$.

^ℓ Assuming predominantly N_2 atmosphere.

^ζ Assuming $p\text{O}_2 = 10^{-3}$ bar, $[\text{SO}_4^{2-}] = 500$ mol/kg.

NOTE.—All values are approximate. See primary references for assumptions and caveats not noted here.

2.3. Model Constraints on Evolving Climate

Standard stellar evolution models (Gough 1981) predict that the Sun was 20–30% less luminous than it is today during the Hadean and Archean. With a planetary greenhouse effect equivalent to that of the modern Earth, this would lead to below-freezing global average surface temperatures prior to ~ 2 Ga, in stark contrast to observations from Earth’s rock record — an inconsistency often referred to as the “Faint Young Sun Paradox” (Sagan & Mullen 1972; Feulner 2012). The observation of a generally clement or even warm climate during the Hadean and Archean (see above) thus implies that the composition of Earth’s atmosphere was very different from that of the modern (barring major changes in orbital parameters or non-chemical albedo effects). Indeed, as discussed above, there is persuasive geological and geochemical evidence that the composition of Earth’s atmosphere was very different during the Hadean, Archean, and Proterozoic.

The most prominent solutions to this problem invoke a larger inventory of greenhouse gases in Earth’s early atmosphere. Sagan & Mullen (1972) explored a reducing NH_3 – CH_4 – H_2S – H_2O – CO_2 greenhouse, with a dominant role for NH_3 . However, the rapid photolysis of NH_3 in the upper atmosphere would have required a very large source at Earth’s surface, and would have in turn resulted in the production of rather extreme amounts of N_2 on geologically rapid timescales (Kuhn & Atreya 1979). More recently, it has been suggested that the photolysis of NH_3 in the upper atmosphere may have been mitigated somewhat by absorption of UV photons by a fractal organic haze (Wolf & Toon 2010), an idea that warrants additional scrutiny of the relative altitudes of peak NH_3 photolysis and haze absorption in future work (Wolf & Toon 2010). In any case, subsequent work has tended to focus on CH_4 – CO_2 – H_2O greenhouses and, more recently, the possible radiative effects of high H_2 (Kasting 2005; Haqq-Misra et al. 2008).

The factors regulating planetary climate on the prebiotic Earth are not particularly well-understood. Direct constraints are few, but models predict that the abundance of CH_4 in Earth’s prebiotic atmosphere would have been low (Kasting 2005; Emmanuel & Ague 2007), while a recent inversion using a geologic carbon cycle model yields a median $p\text{CO}_2$ estimate of 0.3 bar with a 95% confidence interval of 0.03–1.0 bar (Krissansen-Totton et al. 2018). Greenhouses dominated by H_2O and CO_2 with $p\text{CO}_2$ values on the lower end of this range would be unlikely to exhibit clement surface temperatures under Hadean or early Archean solar luminosity, but both 1-D radiative-convective and 3-D global climate models predict that values at the upper end of this range would result in surface temperatures well above freezing under early and late Archean solar luminosity (Kasting & Ackerman 1986; Kasting 1987; Charnay et al. 2013; Wolf & Toon 2013, 2014). Significant additional warming may have been provided by collision-induced absorption by H_2 – N_2 under plausible prebiotic con-

ditions (Wordsworth & Pierrehumbert 2013), though the strength of this would have depended strongly on atmospheric H_2 and N_2 abundance, both of which are poorly constrained for the prebiotic atmosphere.

The emergence of a biosphere on Earth would have had a significant impact on atmospheric chemistry and climate. In particular, primitive microbial metabolisms such as methanogenesis, acetogenesis, and anoxygenic photosynthesis would have dramatically increased fluxes of CH_4 to Earth’s atmosphere. The implications of this for climate are twofold. First, CH_4 is an important greenhouse gas in its own right, providing another means toward offsetting decreased solar luminosity that would be particularly effective in a reducing atmosphere (Pavlov et al. 2000; Haqq-Misra et al. 2008). Second, the potential for large biogenic CH_4 fluxes introduces an additional feedback on climate via formation of an organic haze in the atmosphere (Zahnle 1986; Pavlov et al. 2001; Haqq-Misra et al. 2008). Photochemical models (Haqq-Misra et al. 2008; Zerkle et al. 2012; Arney et al. 2016) and laboratory experiments (DeWitt et al. 2009; Trainer et al. 2004, 2006) predict that once the CH_4/CO_2 ratio of the atmosphere increases beyond ~ 0.1 hydrocarbon aerosols will begin to form, with optical thicknesses at visible and UV wavelengths that increase rapidly at CH_4/CO_2 values between ~ 0.1 –1 (Domagal-Goldman et al. 2008; Haqq-Misra et al. 2008). The formation of these hazes can lead to significant cooling, even at relatively low CH_4/CO_2 values of ~ 0.1 –0.2 (Arney et al. 2016). These combined effects would have been important in regulating climate and surface temperature during both the Archean and Proterozoic.

Taken together, models suggest that clement or even warm surface temperatures could have been maintained on the prebiotic Earth by a CO_2 – H_2O greenhouse, potentially supplemented by collision- and pressure-induced warming at greater H_2 and N_2 abundance (Kasting 1987; Goldblatt et al. 2009; Wordsworth & Pierrehumbert 2013; Krissansen-Totton et al. 2018). Following the emergence of a surface biosphere, 1-D radiative-convective and 3-D global climate models, coupled ecosystem-biogeochemistry models, and the geologic record are all consistent in suggesting that surface temperatures well above freezing could have been maintained throughout the Archean with a CH_4 – H_2O – CO_2 greenhouse and optically thin haze (Haqq-Misra et al. 2008; Zerkle et al. 2012; Charnay et al. 2013; Wolf & Toon 2013; Izon et al. 2017; Ozaki et al. 2018; Krissansen-Totton et al. 2018). However, additional factors beyond changes to the atmospheric greenhouse may also have been important, and together could lead to significant warming. For example, changes to the average size of cloud droplets attendant to fewer cloud condensation nuclei (CCN) in the early atmosphere would have resulted in more effective rainout and fewer low clouds at low-mid latitudes (Charnay et al. 2013; Wolf & Toon 2014) and possibly thinner clouds overall (Goldblatt & Zahnle 2011; Charnay et al. 2013), both of which would have resulted in significant warming. Maintaining a habitable climate during Earth’s

earliest history is thus not particularly challenging, as all of these factors were potentially in play. However, achieving the highest estimates of Archean temperature with plausible atmospheric CO₂ and CH₄ levels remains a challenge.

Existing models of the long-term carbon cycle and surface temperature are broadly consistent with geochemical evidence for elevated *p*CO₂ during the Paleoproterozoic (e.g., Halevy & Bachan 2017; Krissansen-Totton et al. 2018). However, the initial rise of atmospheric O₂ at ~2.3 Ga would have destabilized the Archean atmospheric greenhouse (Claire et al. 2006; Zahnle et al. 2006; Haqq-Misra et al. 2008), potentially leading to dramatic effects on climate during the earliest Paleoproterozoic (see above). Understanding climate dynamics and coherently modeling climate and biogeochemistry during and after the GOE and through the Lomagundi Event remain outstanding challenges, but existing models suggest large changes to Earth surface temperature, the global carbon cycle, and atmospheric composition (Claire et al. 2006; Harada et al. 2015).

There is limited geologic evidence for glacial conditions during the mid-Proterozoic (see above), despite a solar luminosity ~10% lower than that of the modern Earth (Gough 1981). Recent coupled 3-D climate modeling indicates that global glaciation should occur under these conditions if atmospheric *p*CO₂ drops to around 10⁻³ bar (Fiorella & Sheldon 2017), and extensive glaciation at high and middle latitudes should occur even above *p*CO₂ values an order of magnitude higher than the modern Earth unless surface temperatures are buffered by some other greenhouse gas. Nitrous oxide (N₂O) would be unlikely to provide the requisite radiative forcing on its own, given the relatively low atmospheric *p*O₂ during the mid-Proterozoic and the large biological nitrogen fluxes required (Roberson et al. 2011), but may have a marginal impact on surface temperatures (Buick 2007; Stanton et al. 2018). Methane (CH₄) is another candidate, but 3-D models of ocean biogeochemistry (Olson et al. 2016) interpreted in light of 3-D climate modeling (Fiorella & Sheldon 2017) indicate that an ocean-only CH₄ cycle would have been unable to maintain an ice-free climate during the mid-Proterozoic. One possible solution to this would be a significant microbial CH₄ flux from terrestrial ecosystems (Zhao et al. 2018). Alternatively, atmospheric *p*CO₂ may have been somewhat higher than geochemical proxies suggest (Krissansen-Totton et al. 2018), or other changes to factors like cloud droplet radius or surface albedo may have contributed to stabilizing relatively warm temperatures (Fiorella & Sheldon 2017). Lastly, at least periods of the mid-Proterozoic may not have been entirely ice-free (see above). In any case, climate models, geochemical proxies, and models of marine/terrestrial biogeochemistry yield a picture of a relatively weak H₂O–CO₂ greenhouse buffered by CH₄ levels on the order of ~10⁻⁵ bar or slightly less, depending on the importance of terrestrial CH₄ cycling.

The dynamics of Earth's climate during the intense ice ages of the late Proterozoic are much more well-studied than their Paleoproterozoic counterparts, and the reader is

here referred to two recent comprehensive reviews on the subject (Pierrehumbert et al. 2011; Hoffman et al. 2017). However, the biogeochemical dynamics associated with these perturbations are more poorly understood, particularly with regard to Earth's O₂ and CH₄ cycles, and this represents an important topic of future work. For example, although impacts to the Earth's "oxidized" carbon cycle have been explored in a range of models (Le Hir et al. 2008b,a; Mills et al. 2011), it remains unclear what role Earth's CH₄ cycle may have played in the inception or recovery from low-latitude glaciation, if any (Schrag et al. 2002; Pierrehumbert et al. 2011; Olson et al. 2016). In any case, the Sturtian glacial episode in particular is estimated to have lasted for roughly 50 million years (Rooney et al. 2014), with the attendant impacts on atmospheric biosignatures and the remote detectability of any surviving biosphere almost completely unknown.

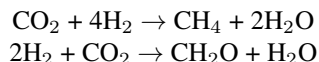
The Phanerozoic climate system, though perhaps relatively stable in the scope of Earth's entire history, has been extremely dynamic, with at least three major ice ages and intervening periods of relatively warm, largely ice-free conditions (see above). Though they differ in their tectonic boundary conditions, scope/intensity, and overall biological impact these climate shifts are generally considered to have been driven primarily by variations in atmospheric CO₂, together with internal climate system feedbacks and modulated by changes in Earth's orbital parameters (Zachos et al. 2001; Royer et al. 2004; Herrmann et al. 2004; Montañez & Poulsen 2013). The Phanerozoic climate system is thus thought to have been controlled largely by an H₂O–CO₂ greenhouse, buffered by volcanic outgassing, organic carbon weathering under a high-O₂ atmosphere, and solar luminosity roughly equivalent to that of the modern Earth. A notable exception to this may have occurred during the Carboniferous 'coal swamp' era roughly 300 million years ago, during which biogeochemical and climate models predict significant radiative forcing from atmospheric CH₄ (Bartdorff et al. 2008; Beerling et al. 2009). Taken together, low-order and 3-D climate models are consistent with geologic and geochemical records in indicating that Earth's surface has been consistently habitable for the last ~500 million years, with long-term average surface temperatures largely within the range of ~15 – 25°C (Royer et al. 2004; Lenton et al. 2018).

2.4. Model Constraints on Evolving Atmospheric Chemistry

Theoretical models have also provided a great deal of insight into the evolving redox state and major background gas composition of Earth's atmosphere. Earth's prebiotic atmosphere is generally thought to have been mildly reducing, composed predominantly of N₂–CO₂–H₂O, with variable H₂ and CH₄ and only trace amounts of species like O₂, O₃, and N₂O. Photochemical models assuming that hydrogen escaped the Archean atmosphere at the diffusion limit

(e.g., Hunten 1973) predict that ground-level atmospheric O_2 would have been on the order of $\sim 10^{-14}$ - 10^{-12} bar, with H_2 on the order of $\sim 10^{-4}$ - 10^{-3} bar depending on the assumed volcanic outgassing rate (Kasting & Walker 1981; Haqq-Misra et al. 2011). However, it has been suggested that lower exobase temperatures in an O_2 -poor, CO_2 -rich atmosphere would have significantly decreased the efficiency of thermal (Jeans) escape at the top of the atmosphere, with the result that rates of hydrogen escape would have been controlled instead by extreme ultraviolet (EUV) energy fluxes from the young Sun (Tian et al. 2005). Balancing these “energy-limited” escape rates with plausible volcanic H_2 outgassing rates results in H_2 mixing ratios as high as ~ 0.3 bar, with important ramifications for prebiotic chemistry (Tian et al. 2005) and early climate (Wordsworth & Pierrehumbert 2013). There remains some debate as to whether heating of the exobase by gases other than O_2 and/or other nonthermal escape processes could promote more efficient escape (Catling 2006; Tian et al. 2006). Nevertheless, it remains plausible that Earth’s prebiotic atmosphere was relatively H_2 -rich.

The evolution of the earliest biosphere would have dramatically transformed atmospheric chemistry. In particular, the emergence of microbial methanogenesis and the evolution of the most primitive forms of anoxygenic photosynthesis, both of which are thought to be very ancient based on geochemical (Tice & Lowe 2004; Ueno et al. 2006) and phylogenetic (Xiong et al. 2000; Wolfe & Fournier 2018) evidence, would have consumed H_2 through reactions such as:

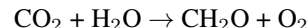


Both processes would have the net effect of decreasing the atmospheric H_2/CH_4 ratio, to an extent that would be limited by the availability of energy and nutrients (Kharecha et al. 2005; Ozaki et al. 2018). In particular, globally integrated rates of anoxygenic photosynthesis would most likely have been limited by the availability of electron donors (H_2 , Fe^{2+} , H_2S), in contrast to oxygenic photosynthesis which can use water as an electron donor (see below). Models of the Earth’s primitive biosphere can produce extremely high atmospheric CH_4 levels, on the order of $\sim 10^{-2}$ bar (Figure 2), depending on electron donor flux, levels of available nutrients, and photosynthetic community assemblage (Kharecha et al. 2005; Ozaki et al. 2018). However, these models neglect microbial anaerobic oxidation of methane (AOM), under the presumption that Archean seawater sulfate levels were extremely low (e.g., Crowe et al. 2014), and to some extent plausible upper limits on atmospheric CH_4 are constrained by the climate effects of hydrocarbon haze formation at elevated CH_4/CO_2 ratios such that atmospheric CH_4 should not be treated in isolation (Ozaki et al. 2018). Nevertheless, existing models consistently predict that the emergence of Earth’s earliest biosphere would have dramatically shifted the atmospheric

CH_4/H_2 ratio, readily supporting atmospheric CH_4 levels that would have the potential for remote observation (Reinhard et al. 2017a; Arney et al. 2018).

Mass balance calculations (Goldblatt et al. 2009) and time-dependent biogeochemical models (Stüeken et al. 2016) are consistent with elevated atmospheric N_2 throughout the Archean, but can also accommodate long-term decrease in pN_2 through the Hadean and Archean depending on the assumed history of CO_2 outgassing and the mechanics coupling organic C and N burial (Stüeken et al. 2016). Similarly, existing models of the carbon cycle that are coupled to long-term stellar evolution are broadly consistent with geochemical data in indicating high atmospheric pCO_2 and a secular decline through the Hadean and Archean (Kasting 1987; Sleep & Zahnle 2001; Halevy & Bachan 2017; Charnay et al. 2017; Krissansen-Totton et al. 2018). The particular trajectories depend on assumptions regarding secular changes in heat flow, the mechanisms regulating seafloor weathering, and the timing and magnitude of major changes to the Earth surface CH_4 cycle. Fully understanding the impact of atmospheric N_2 and CO_2 on the detectability of habitability markers and atmospheric biosignatures on the Hadean/early Archean Earth will require both more precise geochemical/paleobarometric constraints and further development of approaches that effectively couple models of long-term biogeochemistry and climate to dynamic models of ocean-atmosphere redox.

The evolution of oxygenic photosynthesis resulted in an autotrophic biosphere that could use water as an electron donor, freeing global autotrophy from electron donor limitation and dramatically increasing the potential energy flux through the biosphere:



The timing of this event is still debated, but is likely to have occurred at some point prior to the late Archean (Kurzweil et al. 2013; Planavsky et al. 2014a; Magnabosco et al. 2018). Following the emergence of biological oxygen production, atmospheric chemistry would have been controlled largely by the balance of fluxes between O_2 and CH_4 produced by the surface biosphere and the consumption of O_2 by reducing volcanic/metamorphic gases and weathering reactions with reduced phases in Earth’s upper crust (Catling & Claire 2005). Low-order biogeochemical models and 1-D models of atmospheric chemistry are consistent with constraints from the geologic record (discussed above) in suggesting low atmospheric pO_2 , on the order of $\sim 10^{-10}$ – 10^{-8} bar, and relatively high atmospheric pCH_4 , around 10^{-4} – 10^{-3} bar, on the Archean Earth after the emergence of an oxygenic biosphere (Goldblatt et al. 2006; Claire et al. 2006; Zahnle et al. 2006; Daines & Lenton 2016).

A number of potential drivers have been suggested for the GOE, including secular tectonic processes (Kump & Barley 2007; Holland 2009; Gaillard et al. 2011), changes in global biological fluxes (Kopp et al. 2005; Konhauser

et al. 2009), and time-integrated hydrogen escape from the atmosphere (Catling et al. 2001; Claire et al. 2006). It is likely that to some extent all of these factors were important. Atmospheric $p\text{O}_2$ may have changed by many orders of magnitude moving across the GOE, with most models predicting a geologically instantaneous rise from $\sim 10^{-8}$ bar to as high as $\sim 10^{-2}$ bar regardless of the underlying mechanism (Claire et al. 2006; Goldblatt et al. 2006). Both the timing and magnitude of this event are consistent with existing isotopic records (e.g., Luo et al. 2016). However, biogeochemical models suggest that the imbalance in the global redox budget required to transit the GOE need not necessarily have been large (Claire et al. 2006; Goldblatt et al. 2006).

The GOE effectively represented a shift in the trace redox gas in Earth's atmosphere from O_2 to CH_4 . Although models do indeed predict an initial drop in atmospheric $p\text{CH}_4$ during the GOE, the ultimate establishment of a substantial stratospheric O_3 layer attendant to rising ground-level $p\text{O}_2$ is predicted to shield CH_4 from destruction in the troposphere. This allows atmospheric CH_4 levels to rebound in photochemical models to $\sim 10^{-4}$ bar in the Proterozoic (Claire et al. 2006; Goldblatt et al. 2006). However, models that include ocean biogeochemistry and microbial consumption of CH_4 with O_2 and SO_4^{2-} generally result in lower steady-state atmospheric $p\text{CH}_4$ following the GOE, typically on the order of $\sim 10^{-5}$ bar or lower (Catling et al. 2007; Daines & Lenton 2016; Olson et al. 2016). These results depend strongly on assumed atmospheric $p\text{O}_2$ and the ocean reservoir of SO_4^{2-} (Olson et al. 2016), and are not currently equipped to deal with the potentially important impacts of a terrestrial biosphere (Zhao et al. 2018). A full exploration of this problem will require coupled, open-system models of photochemistry and ocean/terrestrial microbial metabolism. Nevertheless, the abundance of CH_4 in Earth's atmosphere following the GOE was likely significantly lower than that of the Archean Earth, and in particular would have been orders of magnitude below that of the earliest Archean and Hadean Earth prior to the evolution of oxygenic photosynthesis (Kharecha et al. 2005; Ozaki et al. 2018). Unfortunately, a quantitative geologic or geochemical indicator of atmospheric $p\text{CH}_4$ at levels below those of the Archean has not yet been developed, and atmospheric $p\text{CH}_4$ is very difficult to track empirically throughout the remainder of Earth's history.

Although the differences in mean state before and after the GOE are relatively well understood, the dynamics of climate and atmospheric chemistry in the immediate aftermath of the GOE are not. Some models predict that this change to Earth's surface redox balance would have had significant climate impacts (Claire et al. 2006; Haqq-Misra et al. 2008), one result of which may have been an ultimately transient but quantitatively dramatic elevation in atmospheric $p\text{O}_2$ (Harada et al. 2015). This scenario would be consistent with emerging geochemical evidence for elevated atmospheric O_2 (and thus O_3), possibly for 100-million-year timescales, during the Paleoproterozoic (see above). The protracted,

but ultimately transient, rise in atmospheric $p\text{O}_2$ implies a significant drop in atmospheric CH_4 levels (Harada et al. 2015), and potentially a substantial drop in atmospheric $p\text{CO}_2$ unless buffered by a sedimentary rock cycle very different from that of the modern Earth (e.g., Bachan & Kump 2015). In any case, long-term (e.g. mean state) carbon cycle and climate models that are entirely uncoupled or only implicitly coupled to the O_2 cycle are broadly consistent with the current geochemical constraints for atmospheric $p\text{CO}_2$ during the Paleoproterozoic discussed above (Sleep & Zahnle 2001; Halevy & Bachan 2017; Krissansen-Totton et al. 2018).

The initial accumulation of O_2 in Earth's atmosphere appears to have been followed by a subsequent return to relatively low ocean-atmosphere oxygen levels during the mid-Proterozoic (between $\sim 1.8 - 0.8$ billion years ago). However, the absence of non-mass-dependent S isotope fractionations in marine sediments and the apparent absence of reduced detrital minerals in fluvial settings indicate atmospheric $p\text{O}_2$ remained above $\sim 10^{-6}$ bar. On long timescales, the modern atmospheric O_2 level is maintained dynamically by the balance between net O_2 sources (principally the burial of organic carbon and reduced sulfur into the Earth's upper crust) and net O_2 sinks (largely the subsequent exhumation and oxidative weathering of organic carbon and reduced sulfur, along with reactions between O_2 and reduced metamorphic and volcanic gases). However, there are strong nonlinearities in the scaling relationships between these fluxes and the amount of O_2 in the atmosphere. In addition, the major sink fluxes on the modern Earth decrease in magnitude as atmospheric $p\text{O}_2$ drops, while the major source fluxes increase. As a result, not all atmospheric $p\text{O}_2$ values are equally stable, and understanding the internal processes and feedbacks capable of maintaining atmospheric O_2 levels above those characteristic of the Archean but well below those of the modern Earth remains an outstanding question (Lyons et al. 2014; Daines et al. 2017).

As discussed above, models of mid-Proterozoic climate and biogeochemistry suggest a relatively weak $\text{H}_2\text{O}-\text{CO}_2$ greenhouse buffered by modest CH_4 levels (Figure 2, Table 1). In particular, long-term carbon cycle models suggest atmospheric $p\text{CO}_2$ of around $\sim 10^{-3}-10^{-2}$ bar during the mid-Proterozoic, while models of marine/terrestrial biogeochemistry suggest atmospheric $p\text{CH}_4$ values on the order of $\sim 10^{-6}-10^{-5}$ bar, together consistent with most geochemical constraints and a largely ice-free climate state (Fiorella & Sheldon 2017). That said, some paleosol reconstructions approach roughly modern $p\text{CO}_2$ values (e.g., Sheldon 2013), which is difficult to reconcile with evidence for a largely ice-free Earth surface for most of the mid-Proterozoic unless Earth's greenhouse was impacted strongly by fluxes of CH_4 from a terrestrial microbial biosphere (Zhao et al. 2018). A full picture of Earth's mid-Proterozoic atmosphere awaits a comprehensive model that couples open-system carbon cycling with a balanced redox budget and dynamic O_2 - CH_4 cycle, but existing data and

models are consistent with this period of Earth’s history representing a potential “false negative” for conventional biosignature techniques (e.g., Reinhard et al. 2017a) — a period through which the spectral features of most canonical biosignature gases would have been relatively weak, perhaps for geologic timescales.

Though there is accumulating geologic and geochemical evidence that the extreme low-latitude glaciations of the late Proterozoic were associated with significant changes to ocean-atmosphere redox and atmospheric chemistry (Hoffman et al. 1998; Canfield et al. 2007; Sahoo et al. 2012; Cox et al. 2013; Planavsky et al. 2014b; Thomson et al. 2015; Hoffman et al. 2017), the relative timing and mechanistic links remain somewhat obscure. Simple biogeochemical models indicate that low-latitude glacial episodes can readily drive a secular transition from low- to high-oxygen steady states at sufficiently high $p\text{CO}_2$ thresholds for deglaciation (Laakso & Schrag 2017). For example, a deglaciation threshold of $p\text{CO}_2 \sim 0.1$ bar is sufficient to drive a permanent transition in atmospheric $p\text{O}_2$ from 10^{-3} to 10^{-1} bar (Laakso & Schrag 2017) during deglaciation. Glacial CO_2 levels of this order are readily achievable even in models that allow for efficient ocean-atmosphere gas exchange and seafloor weathering (e.g., Le Hir et al. 2008b). Efforts to better understand the temporal polarity and mechanistic details linking climate destabilization and nonlinear changes to atmospheric chemistry during both the Paleoproterozoic and Neoproterozoic represent an important avenue of future work. Nevertheless, significant changes in the redox state of Earth’s ocean-atmosphere system are strongly implicated as having been both cause and consequence of sporadic perturbations to Earth’s habitability.

Biogeochemical models are generally consistent in suggesting a high- O_2 , low- CH_4 , and moderate CO_2 atmosphere throughout the Phanerozoic (541 Ma to the present). Both atmospheric O_2 and atmospheric CO_2 have been controlled by the combined effects of roughly modern solar luminosity, time-dependent variability in volcanic degassing, rock uplift, changes to the major ion chemistry of seawater, and the emergence and expansion of terrestrial ecosystems (Berner 1991, 2006; Royer et al. 2014; Lenton et al. 2018). Long-term atmospheric CH_4 levels have been controlled largely by the evolutionary and climate dynamics controlling biogenic CH_4 fluxes from terrestrial ecosystems (Bartdorff et al. 2008). Despite some discrepancies between different models in estimates of atmospheric $p\text{O}_2$ during the earliest part of the Phanerozoic, most models indicate ranges for atmospheric $p\text{O}_2$, $p\text{CO}_2$, and $p\text{CH}_4$ between $\sim 0.1 - 0.3$ bar, $\sim 10^{-4} - 10^{-3}$ bar, and $\sim 10^{-7} - 10^{-5}$ bar, respectively, all of which are consistent with existing geologic and geochemical constraints (Figure 2, Table 1). Similar models for atmospheric $p\text{N}_2$ through time suggest values close to that of the modern Earth for most of the Phanerozoic, though direct geologic constraints on this are lacking for all but the most recent periods of Earth’s history.

Observations from the geologic record and results from quantitative models are united in suggesting extensive

changes to the Earth system over time, including the chemistry of the ocean-atmosphere system, the dynamics of long-term climate, and the size and scope of Earth’s biosphere. The contours of this evolution provide important information for exoplanet characterization efforts. In particular, simulating and predicting observations across the spectrum of habitable worlds represented in Earth’s evolutionary history provides a series of test cases for evaluating putative discriminants of habitability and life on Earth-like planets beyond our solar system, and can potentially provide important insight into the challenges associated with deciphering exo-Earth observations.

3. REMOTE DETECTABILITY OF EARTH’S BIOSPHERE THROUGH TIME

How would Earth’s evolving climate and atmospheric chemistry have appeared to a remote observer? We focus here on a subset of the most prominent biosignatures that may be remotely detectable — namely, atmospheric oxygen (O_2), its photochemical byproduct ozone (O_3), methane (CH_4), hydrocarbon haze, and nitrous oxide (N_2O) (e.g., Schwieterman et al. 2018). We also include two major habitability indicators — water vapor (H_2O) and carbon dioxide (CO_2) — the latter of which is required for climate system stabilization via the carbonate-silicate geochemical cycle (Walker et al. 1981). The true detectability of any particular biosignature or habitability indicator will depend on the magnitude of the signal produced (related to, e.g., a species’ atmospheric abundance and the atmospheric opacity produced by a specific feature), the parameters controlling observational precision (e.g., stellar host, distance to the target, instrument and astrophysical noise sources), and the wavelength range accessible to the instrument being used. Our discussion is thus not meant to be exhaustive or definitive, but is instead meant to provide some context for motivating remote observations of the modern Earth and simulated observations of different periods of Earth’s evolutionary history. As a guide to this discussion, Table 2 contains a detailed listing of the wavelengths, widths, and strengths of spectral features for key biosignature and habitability indicator gases.

The most prominent features of molecular oxygen (O_2) are at 0.76 and 0.69 μm , the Fraunhofer A and B bands, respectively. The Fraunhofer A band is the stronger of the two bands, but is likely to be relatively weak unless atmospheric $p\text{O}_2$ is above the few percent level (Des Marais et al. 2002; Reinhard et al. 2017a; Schwieterman et al. 2018). When considered in the context of Earth’s evolution, it is clear that O_2 spectral features were likely non-existent during the Archean, and may have been weak during much of the Proterozoic. However, absorption by O_2 at both the Fraunhofer A and B bands would have been relatively strong through essentially all of Phanerozoic time and possibly during a protracted interval in the Paleoproterozoic.

TABLE 2
SPECTRAL FEATURE DETAILS FOR KEY BIOSIGNATURE AND HABITABILITY INDICATOR GASES

Species	λ^a (μm)	$\Delta\lambda^b$ (μm)	$\lambda/\Delta\lambda$	Opacity ^c ($\text{cm}^2 \text{ molecule}^{-1}$)	Optical Depth ^d
O ₂	0.629	3.0×10^{-3}	210	1.5×10^{-25}	6.7×10^{-1}
O ₂	0.689	4.1×10^{-3}	170	3.9×10^{-24}	$1.7 \times 10^{+1}$
O ₂	0.762	5.1×10^{-3}	150	5.8×10^{-23}	$2.6 \times 10^{+2}$
O ₂	0.865	6.6×10^{-3}	130	1.6×10^{-27}	7.3×10^{-3}
O ₂	1.07	4.3×10^{-3}	250	2.7×10^{-27}	1.2×10^{-2}
O ₂	1.27	5.8×10^{-3}	220	7.8×10^{-25}	$3.5 \times 10^{+0}$
O ₂	6.30	3.2×10^{-1}	19	3.2×10^{-27}	1.4×10^{-2}
—					
O ₃	0.256	3.9×10^{-2}	6.5	1.2×10^{-17}	$1.1 \times 10^{+2}$
O ₃	0.600	1.2×10^{-1}	5.0	4.8×10^{-21}	4.4×10^{-2}
O ₃	2.48	2.1×10^{-3}	1100	1.5×10^{-21}	1.3×10^{-2}
O ₃	3.27	6.9×10^{-3}	470	1.2×10^{-20}	1.1×10^{-1}
O ₃	3.59	4.7×10^{-2}	77	1.8×10^{-21}	1.6×10^{-2}
O ₃	4.74	8.7×10^{-2}	54	7.6×10^{-20}	6.9×10^{-1}
O ₃	5.80	1.6×10^{-1}	37	3.8×10^{-21}	3.4×10^{-2}
O ₃	9.58	3.5×10^{-1}	27	7.3×10^{-19}	$6.7 \times 10^{+0}$
O ₃	14.3	$1.0 \times 10^{+0}$	14	2.6×10^{-20}	2.3×10^{-1}
—					
CH ₄	0.510	5.0×10^{-3}	100	4.3×10^{-27}	1.5×10^{-7}
CH ₄	0.542	5.0×10^{-3}	110	4.6×10^{-26}	1.5×10^{-7}
CH ₄	0.576	8.0×10^{-3}	72	1.3×10^{-26}	1.5×10^{-7}
CH ₄	0.598	8.0×10^{-3}	75	9.0×10^{-27}	1.5×10^{-7}
CH ₄	0.619	8.0×10^{-3}	77	2.2×10^{-25}	1.5×10^{-7}
CH ₄	0.667	1.5×10^{-2}	44	5.6×10^{-26}	1.5×10^{-7}
CH ₄	0.703	1.1×10^{-2}	64	1.1×10^{-25}	1.5×10^{-7}
CH ₄	0.726	1.0×10^{-2}	73	1.4×10^{-24}	1.5×10^{-7}
CH ₄	0.798	2.5×10^{-2}	32	4.4×10^{-25}	1.5×10^{-7}
CH ₄	0.840	1.0×10^{-2}	84	3.3×10^{-25}	1.5×10^{-7}
CH ₄	0.861	1.1×10^{-2}	78	1.9×10^{-24}	1.5×10^{-7}
CH ₄	0.887	1.8×10^{-2}	49	1.1×10^{-23}	1.5×10^{-7}
CH ₄	1.00	3.7×10^{-2}	27	6.4×10^{-24}	1.5×10^{-7}
CH ₄	1.13	1.3×10^{-2}	87	3.2×10^{-22}	1.1×10^{-2}
CH ₄	1.16	7.4×10^{-3}	160	7.7×10^{-22}	2.6×10^{-2}
CH ₄	1.33	1.4×10^{-4}	9400	1.9×10^{-21}	2.6×10^{-2}
CH ₄	1.65	1.3×10^{-2}	120	1.8×10^{-20}	6.2×10^{-1}
CH ₄	1.67	1.4×10^{-3}	1200	1.4×10^{-20}	4.9×10^{-1}
CH ₄	1.68	1.3×10^{-2}	130	8.1×10^{-21}	2.8×10^{-1}
CH ₄	2.20	1.2×10^{-3}	1800	8.1×10^{-21}	2.8×10^{-1}
CH ₄	2.31	6.6×10^{-2}	35	2.9×10^{-20}	$1.0 \times 10^{+0}$
CH ₄	2.37	2.3×10^{-2}	100	3.7×10^{-20}	$1.3 \times 10^{+0}$
CH ₄	2.59	1.9×10^{-2}	130	2.5×10^{-21}	8.7×10^{-2}
CH ₄	3.32	9.4×10^{-2}	35	2.1×10^{-18}	$7.1 \times 10^{+1}$
CH ₄	7.66	2.3×10^{-1}	34	7.7×10^{-19}	$2.6 \times 10^{+1}$
—					
N ₂ O	1.52	1.1×10^{-2}	140	1.2×10^{-22}	7.9×10^{-4}
N ₂ O	1.67	1.3×10^{-2}	130	8.0×10^{-23}	5.1×10^{-4}
N ₂ O	1.70	1.4×10^{-2}	120	2.9×10^{-23}	1.8×10^{-4}
N ₂ O	1.77	1.5×10^{-2}	120	7.5×10^{-23}	4.8×10^{-4}
N ₂ O	1.96	1.8×10^{-2}	110	2.2×10^{-22}	1.4×10^{-3}
N ₂ O	1.99	2.0×10^{-2}	100	2.3×10^{-22}	1.5×10^{-3}

TABLE 2—*Continued*

Species	λ^a (μm)	$\Delta\lambda^b$ (μm)	$\lambda/\Delta\lambda$	Opacity ^c ($\text{cm}^2 \text{ molecule}^{-1}$)	Optical Depth ^d
N ₂ O	2.04	2.1×10^{-2}	100	4.0×10^{-23}	2.6×10^{-4}
N ₂ O	2.11	2.1×10^{-2}	100	3.3×10^{-21}	2.1×10^{-2}
N ₂ O	2.16	2.4×10^{-2}	91	4.6×10^{-22}	2.9×10^{-3}
N ₂ O	2.26	2.5×10^{-2}	90	5.2×10^{-21}	3.3×10^{-2}
N ₂ O	2.46	3.1×10^{-2}	78	2.2×10^{-22}	1.4×10^{-3}
N ₂ O	2.61	3.3×10^{-2}	80	6.6×10^{-21}	4.2×10^{-2}
N ₂ O	2.67	3.5×10^{-2}	75	3.1×10^{-21}	2.0×10^{-2}
N ₂ O	2.87	4.0×10^{-2}	71	1.5×10^{-19}	9.5×10^{-1}
N ₂ O	2.97	4.6×10^{-2}	65	7.3×10^{-21}	4.7×10^{-2}
N ₂ O	3.58	5.6×10^{-2}	63	2.5×10^{-20}	1.6×10^{-1}
N ₂ O	3.90	7.6×10^{-2}	52	1.1×10^{-19}	6.8×10^{-1}
N ₂ O	4.06	8.3×10^{-2}	49	2.5×10^{-20}	1.6×10^{-1}
N ₂ O	4.31	9.9×10^{-2}	43	2.2×10^{-21}	1.4×10^{-2}
N ₂ O	4.50	9.9×10^{-2}	45	4.4×10^{-18}	$2.8 \times 10^{+1}$
N ₂ O	5.32	8.7×10^{-2}	61	1.6×10^{-20}	1.0×10^{-1}
N ₂ O	5.72	1.4×10^{-1}	42	6.4×10^{-22}	4.1×10^{-3}
N ₂ O	6.12	2.0×10^{-1}	31	4.1×10^{-22}	2.6×10^{-3}
N ₂ O	7.78	3.1×10^{-1}	25	7.4×10^{-19}	$4.7 \times 10^{+0}$
N ₂ O	8.56	3.7×10^{-1}	25	2.6×10^{-20}	1.6×10^{-1}
N ₂ O	9.47	4.7×10^{-1}	20	2.7×10^{-23}	1.7×10^{-4}
N ₂ O	10.7	5.5×10^{-1}	19	1.4×10^{-22}	8.8×10^{-4}
N ₂ O	14.4	9.6×10^{-1}	15	7.4×10^{-22}	4.7×10^{-3}
N ₂ O	17.0	$1.1 \times 10^{+0}$	15	6.4×10^{-19}	$4.1 \times 10^{+0}$
—					
H ₂ O	0.653	1.0×10^{-2}	65	1.2×10^{-23}	$1.1 \times 10^{+0}$
H ₂ O	0.722	1.1×10^{-2}	64	1.3×10^{-22}	$1.2 \times 10^{+1}$
H ₂ O	0.823	1.5×10^{-2}	55	1.7×10^{-22}	$1.7 \times 10^{+1}$
H ₂ O	0.940	2.1×10^{-2}	45	2.2×10^{-21}	$2.1 \times 10^{+2}$
H ₂ O	1.14	2.9×10^{-2}	39	4.9×10^{-21}	$4.8 \times 10^{+2}$
H ₂ O	1.38	4.3×10^{-2}	32	6.6×10^{-20}	$6.5 \times 10^{+3}$
H ₂ O	1.89	8.9×10^{-2}	21	1.0×10^{-19}	$9.8 \times 10^{+3}$
H ₂ O	2.65	1.8×10^{-1}	15	8.5×10^{-19}	$8.3 \times 10^{+4}$
H ₂ O	3.17	3.0×10^{-1}	11	6.4×10^{-21}	$6.3 \times 10^{+2}$
H ₂ O	3.68	2.2×10^{-1}	17	5.2×10^{-23}	$5.0 \times 10^{+0}$
H ₂ O	6.27	$1.1 \times 10^{+0}$	5.7	1.2×10^{-18}	$1.2 \times 10^{+5}$
—					
CO ₂	1.43	9.8×10^{-3}	150	2.6×10^{-22}	$1.8 \times 10^{+0}$
CO ₂	1.58	1.1×10^{-2}	140	7.6×10^{-23}	5.3×10^{-1}
CO ₂	1.61	1.2×10^{-2}	130	7.6×10^{-23}	5.3×10^{-1}
CO ₂	1.96	1.7×10^{-2}	110	1.9×10^{-21}	$1.3 \times 10^{+1}$
CO ₂	2.01	1.9×10^{-2}	110	5.6×10^{-21}	$3.9 \times 10^{+1}$
CO ₂	2.06	1.7×10^{-2}	120	1.2×10^{-21}	$8.3 \times 10^{+0}$
CO ₂	2.69	3.4×10^{-2}	79	2.6×10^{-19}	$1.8 \times 10^{+3}$
CO ₂	2.77	3.6×10^{-2}	76	1.7×10^{-19}	$1.2 \times 10^{+3}$
CO ₂	4.26	8.6×10^{-2}	50	1.6×10^{-17}	$1.1 \times 10^{+5}$
CO ₂	7.31	2.5×10^{-1}	29	2.9×10^{-24}	2.1×10^{-2}
CO ₂	7.94	3.0×10^{-1}	27	2.6×10^{-24}	1.8×10^{-2}
CO ₂	9.40	4.2×10^{-1}	22	1.3×10^{-22}	9.4×10^{-1}
CO ₂	10.4	5.1×10^{-1}	20	8.5×10^{-23}	0.6×10^{-1}
CO ₂	15.0	9.6×10^{-1}	16	4.4×10^{-18}	$3.1 \times 10^{+4}$

Ozone (O_3), which is produced photochemically by O_2 and thus scales with atmospheric O_2 abundance, is an extremely useful biosignature in the context of Earth evolution. Ozone offers strong spectral features across a range of wavelengths, including diagnostic features in the mid-infrared (at $9.6\ \mu\text{m}$), the visible/near-infrared (the Chapuis band between 0.55 and $0.65\ \mu\text{m}$), and in the ultraviolet (the Hartley-Huggins bands centered near $0.26\ \mu\text{m}$). The latter of these is of particular note, as it is sensitive to extremely low peak O_3 abundances of ~ 1 ppm or less. Although all of these features would be extremely weak at the vanishingly low atmospheric O_2/O_3 levels characteristic of the Archean, the Hartley-Huggins band would have produced relatively strong, though not saturated, absorption at atmospheric pO_2 values approaching the lowest inferred for the mid-Proterozoic, while absorption at both the Hartley-Huggins and mid-infrared bands would have been relatively strong at the upper end of mid-Proterozoic pO_2 estimates (Segura et al. 2003; Reinhard et al. 2017a; Rugheimer & Kaltenegger 2018; Olson et al. 2018a). All of these features would have been relatively strong for the last ~ 500 million years of Earth’s evolutionary history, and possibly during the early Paleoproterozoic.

Methane (CH_4) has a number of spectral features, including many relatively weak features spanning the visible wavelength range, stronger near-infrared features at 1.65 , 2.3 , and $2.4\ \mu\text{m}$, and a strong mid-infrared band at $7.7\ \mu\text{m}$. The visible wavelength features between 0.6 and $1.0\ \mu\text{m}$ only have appreciable depth for atmospheric CH_4 abundances above $\sim 10^{-3}$ bar, suggesting that they may have been relatively strong during the Archean and may have been particularly promising biosignatures prior to the evolution of oxygenic photosynthesis (Kharecha et al. 2005; Ozaki et al. 2018). The stronger near-infrared methane features would likely have been prominent for the vast majority of the Archean (Reinhard et al. 2017a). For most of Earth’s history subsequent to the Archean absorption by CH_4 in the mid-infrared at $7.7\ \mu\text{m}$ would have been relatively strong. Indeed, this feature is apparent even at the very low atmospheric CH_4 abundance of the modern Earth (Des Marais et al. 2002). However, overlap with a significant water vapor band may render this feature challenging to detect in some cases.

Hydrocarbon hazes — which can be produced in reducing atmospheres with CH_4/CO_2 ratios above ~ 0.1 — also produce strong features and could represent a biosignature ‘proxy’ for biotic CH_4 production (Arney et al. 2016, 2018). Indeed, there is isotopic evidence for at least sporadic haze production on the Archean Earth (see Section 2.2.1), and photochemical models suggest that the surface CH_4 fluxes required to maintain both haze production and the clement climate state implied by Earth’s rock record are most consistent with biospheric CH_4 production. The most prominent features for haze include a broad ultraviolet/visible absorption feature and a band near $6.5\ \mu\text{m}$ in the mid-infrared. Both may have been relatively strong during the Archean, and the shortwave feature could have caused Earth

to present as a “Pale Orange Dot” early in its history (Arney et al. 2016). However, it is unlikely that Earth’s CH_4/CO_2 ratio has been high enough to produce haze after ~ 2.5 Ga.

Nitrous oxide (N_2O) is a potential atmospheric biosignature, in addition to being a powerful greenhouse gas and an important component of stratospheric ozone chemistry (Prather & Hsu 2010). On the modern Earth, natural (non-anthropogenic) sources of N_2O are dominated by microbial activity in terrestrial soils and productive regions of the surface ocean (Matson & Vitousek 1990; Hirsch et al. 2006). Under low oxygen concentrations, N_2O can be produced biologically during the metabolic oxidation of ammonium (NH_4^+) and nitrite (NO_2^-) and during the reduction of nitrate (NO_3^-) during incomplete denitrification (Bianchi et al. 2012; Freing et al. 2012). The inorganic reaction of nitric oxide (NO) with dissolved ferrous iron (Fe^{2+}) can also produce N_2O in a process referred to as “chemodenitrification” (Wullstein & Gilmour 1966). The source NO for this reaction can be derived from either biological nitrogen fixation or abiotically through the breakdown of atmospheric N_2 by lightning. Still, N_2O is considered a putative biosignature because production of N_2O from the latter is likely to be relatively small (Schumann & Huntrieser 2007). Importantly, the photochemical stability of N_2O is a relatively strong function of atmospheric O_2 (Levine et al. 1979; Kasting & Donahue 1980) — for example, sustaining a modern atmospheric N_2O abundance at a plausible Proterozoic atmospheric pO_2 of $\sim 1\%$ of the present atmospheric level requires a surface N_2O flux of roughly 30 times that on the modern Earth for a Sun-like star (Roberson et al. 2011; Stanton et al. 2018). This suggests that through Earth’s history atmospheric N_2O abundance would broadly have tracked the abundance of atmospheric O_2 and O_3 . Because even modern Earth-like N_2O abundances produce relatively weak spectral features (Schwieterman et al. 2018, and Table 2), N_2O is often not a primary focus of biosignature detectability studies.

Finally, water vapor (H_2O) and carbon dioxide (CO_2), while essential to many biological functions, are also critical signposts of a habitable world. The former will be present in the lower atmosphere of any world with stable surface liquid water, and the latter is key to maintaining surface habitability through its properties as a greenhouse gas and its role in the carbonate-silicate cycle. The spectrum of modern Earth is strongly sculpted by water vapor absorption features throughout the red-visible, near-infrared, and mid-infrared, and these same features would have produced strong spectral features on Earth during all non-snowball periods of its evolution. However, even in extremely cold Snowball Earth scenarios, the water vapor bands spanning the near-infrared at $6.3\ \mu\text{m}$ would remain apparent. Carbon dioxide has several strong features at longer near-infrared wavelengths (most notably at $4.3\ \mu\text{m}$) and in the mid-infrared (at $15\ \mu\text{m}$). Earlier in Earth’s history, where higher levels of CO_2 would have been required to maintain habitable surface conditions, carbon dioxide features at shorter near-infrared wavelengths would have appeared

TABLE 2—*Continued*

Species	λ^a (μm)	$\Delta\lambda^b$ (μm)	$\lambda/\Delta\lambda$	Opacity ^c ($\text{cm}^2 \text{ molecule}^{-1}$)	Optical Depth ^d
---------	----------------------------------	--	-------------------------	---	----------------------------

^aFeature central wavelength.

^bFeature full-width at half-max (assuming $p = 1$ bar and $T = 288$ K).

^cPeak opacity at assumed pressure and temperature.

^dAssuming modern Earth (vertical) column densities and adopting peak opacity values.

much stronger (e.g., bands near 1.6 and 2 μm ; Meadows 2008; Arney et al. 2016; Rugheimer & Kaltenegger 2018).

4. OBSERVING EARTH FROM AFAR

Observational data for the distant Earth provide a critical opportunity to study the spectral appearance of an ocean-bearing, inhabited world. As is discussed below, such data enable investigations into the remote characterization of the physical and chemical state of our planet through applications of Solar System planetary exploration techniques. Zooming even further out, though, observations where Earth is treated as a single pixel — a Pale Blue Dot — provide insights into how we will, one day, study photometric and spectroscopic observations of potentially Earth-like exoplanets for signs of habitability and life.

4.1. Earth as a Planet: The *Galileo* Experiment

The *Pioneer 10/11* (launched 1972; Baker et al. 1975; Gehrels 1976; Ingersoll et al. 1976; Kliore & Woiceshyn 1976) and *Voyager 1/2* missions (launched 1977; Kohlhasse & Penzo 1977; Hanel et al. 1977) enabled the initial exploration of key approaches to analyzing spacecraft flyby data for many Solar System worlds. Instruments and techniques for either acquiring or interpreting spatially-resolved observations of planets and moons using photometry or spectroscopy at wavelengths spanning the ultraviolet through the infrared were among the important developments. From these observations planetary scientists were able to infer details about atmospheric chemistry and composition, cloud and aerosol formation and distribution, atmospheric thermal structure and circulation, surface chemical and thermal properties (for worlds with thin atmospheres), as well as planetary energy balance.

Flybys of Earth by the *Galileo* spacecraft (launched 1989; Johnson et al. 1992) in December of 1990 and 1992 afforded planetary scientists the first opportunity to analyze our planet using the same tools and techniques that had been (and would be) applied throughout the Solar System. During the flybys, data were acquired using the Near-Infrared

Mapping Spectrometer (NIMS; Carlson et al. 1992), the Solid-State Imaging system (SSI; Belton et al. 1992), the Ultraviolet Spectrometer (UVS; Hord et al. 1992), and the Plasma Wave Subsystem (PWS; Gurnett et al. 1992). Critically, spatially-resolved imagery from the SSI was provided across eight filters (Belton et al. 1992, their Table II), and spatially-resolved spectra were acquired by NIMS over 0.7–5.2 μm (at a wavelength resolution, $\Delta\lambda$, of 0.025 μm longward of 1 μm , and 0.0125 μm shortward of 1 μm).

Figure 4 shows a sampling of SSI images of Earth from the first Earth flyby and a time sequence of SSI images of Earth and the Moon that were acquired after the second Earth flyby. Many images from the second Earth flyby suffered from saturation defects. Reconstructed NIMS images from both Earth flybys are shown in Figure 5, where certain instrument and mapping defects can be seen. Here, the 4.0 μm images highlight a wavelength range with relatively little atmospheric opacity and where thermal emission dominates. By contrast, the 2.75 μm image (located within a H_2O absorption band) contains both reflected and thermal contributions, which, for example, results in reflective clouds only being seen in the sunlit portions of the images.

In a landmark study, Sagan et al. (1993) used the *Galileo* flyby data to ascertain key details about the surface and atmospheric state of our planet. Spectra from the NIMS instrument contain information about surface and atmospheric chemistry, and can also indicate surface thermal conditions at longer wavelengths. Thus, Sagan et al. (1993) argued that reflective polar caps seen in SSI images were water ice, and that the surface of the planet spanned the freezing point of water (covering at least 240–290 K). Additionally, the darkest regions in the SSI images showed signs of specular reflection, indicating that these regions were liquid oceans. Finally, clearsky soundings of H_2O absorption features indicated a surface with large relative humidity (i.e., near the condensation point). Taken altogether, these lines of evidence clearly indicate that the world under investigation is habitable, or capable of maintaining liquid water on its surface.

Drossart et al. (1993) retrieved abundances of key atmospheric constituents (CO_2 , H_2O , CO , O_3 , CH_4 , and N_2O)

via simple parameterized fits to resolved NIMS observations (see Figure 6). Here, model spectra were generated by adopting scaled Earth-like profiles for trace atmospheric species. Thermal structure profiles were derived using the 4.3 μm CO_2 band, which rely on this gas having a well-mixed vertical profile (i.e., a near-constant mixing ratio with altitude). For a well-mixed gas, variation in an infrared absorption band can be attributed to thermal structure rather than variation in abundance with altitude.

Observations from the NIMS instrument also indicated large column densities of O_2 in Earth’s atmosphere (Sagan et al. 1993). It was estimated that diffusion-limited escape of hydrogen (produced from H_2O photolysis) would require many billions of years to build up atmospheric oxygen to the observed levels, implying an alternative source. Using the abundances derived in Drossart et al. (1993), it was shown that atmospheric CH_4 was in a state of extreme disequilibrium with no known geological source that could supply CH_4 at the rate required to maintain the observed concentrations. Certain surface regions of the planet imaged in multiple SSI filters demonstrated a sharp increase in reflectivity at wavelengths beyond 700 nm, known from ground-truth investigations to be the vegetation “red edge” (a rapid increase in reflectivity near 0.7 μm that is related to pigments). Thus, multiple lines of evidence point towards the potential for biological activity to be shaping the surface and atmospheric properties of Earth³.

Of course, the strongest evidence for Earth being inhabited came from the PWS dataset (Sagan et al. 1993). Here, radio emissions from our planet were monitored as a function of time and frequency throughout the *Galileo* encounter. Narrow-band emissions between 4–5 MHz (i.e., in the high frequency portion of the radio spectrum where a variety of radio communications occur), isolated in both frequency and time, were interpreted as radio transmissions from an intelligent species on our planet. In other words, an observational approach championed in the search for extraterrestrial intelligence (SETI) — listening at radio frequencies — yielded the least ambiguous evidence for the inhabitation of Earth from the *Galileo* flyby dataset.

In the words of Sagan et al. (1993), the *Galileo* Earth datasets offered a “unique control experiment on the ability of flyby spacecraft to detect life at various stages of evolutionary development.” Combining lines of evidence that spanned the ultraviolet, visible, infrared, and radio spectral regimes, the *Galileo* observations indicated a habitable planet with a diversity of surface environments and whose atmosphere (and, thus, spectrum) is strongly influenced by life. In the context of exoplanets, however, the key question becomes: Which habitability and life signatures are lost when Earth is studied not as a resolved source but as a distant, unresolved target?

4.2. Observing the Pale Blue Dot

A more accurate model for future observations of Earth-like exoplanets is not the *Galileo* flyby observations, but instead the famous “Pale Blue Dot” photograph of Earth taken by the *Voyager 1* spacecraft (see Figure 7). Here — even for future large telescopes — observations will not be able to spatially resolve features on the disk of an exoplanet (although time-domain data can be used to obtain some spatial resolution; e.g., Cowan et al. 2009; Majeau et al. 2012). The resolution of a telescope is limited by the physics of light diffraction to an angular size of roughly λ/D , where λ is wavelength and D is telescope diameter. For a 10-meter class telescope observing at visible wavelengths (i.e., near 500 nm), the angular resolution is at best 5×10^{-8} radians (or about 10 milli-arcseconds). Even for our nearest stellar neighbors (e.g., α Centauri at 1.3 parsecs) this corresponds to a spatial resolution of 2×10^6 km, or about three times the radius of our Sun.

Unresolved observations of planets are sometimes referred to as being “disk-integrated.” Here, the entire three-dimensional complexity of a planet is effectively collapsed into a single pixel. For worlds like Earth, this means that cloud-free regions of the planet are blended with cloudy regions, warm equatorial zones are observationally mixed with cold polar caps, and continents become unresolved from oceans. Additionally, viewing geometry plays an important role, as the portions of the planet near the limb will contribute less overall flux to an observation (since these areas are of smaller solid angular size), and, in reflected light, regions near the day/night terminator will also contribute relatively little flux owing to their lower insolation.

If we wish to extend the analysis techniques applied to the *Galileo* Earth flyby observations to an *unresolved* Pale Blue Dot, we must look towards either observational datasets for an unresolved Earth, or towards datasets or products that can mimic an unresolved Earth. There are, in general, three approaches to obtaining (or constructing) such disk-integrated observations of our planet. First, one can observe light reflected from Earth from the portion of the Moon that is not illuminated by the Sun (i.e., so-called “Earthshine” observations; Danjon 1928; Dubois 1947; Woolf et al. 2002; Pallé et al. 2003; Turnbull et al. 2006). Second, one can use higher spatial resolution observations from satellites in Earth orbit to piece together a more integrated view of Earth (Hearty et al. 2009; Macdonald & Cowan 2019). Finally, spacecraft observations of the distant Earth — like those acquired by *Galileo* — can be integrated over the planetary disk to yield exoplanet-like datasets. We discuss each of these approaches below, highlighting the advantages and disadvantages of each technique.

³The *Galileo* Earth dataset has also been investigated for signs of shadowing caused by trees (Doughty & Wolf 2016), whose vertical structures create distinct bi-directional reflectance distribution functions that have been proposed as a biosignature for Earth-like exoplanets (Doughty & Wolf 2010).

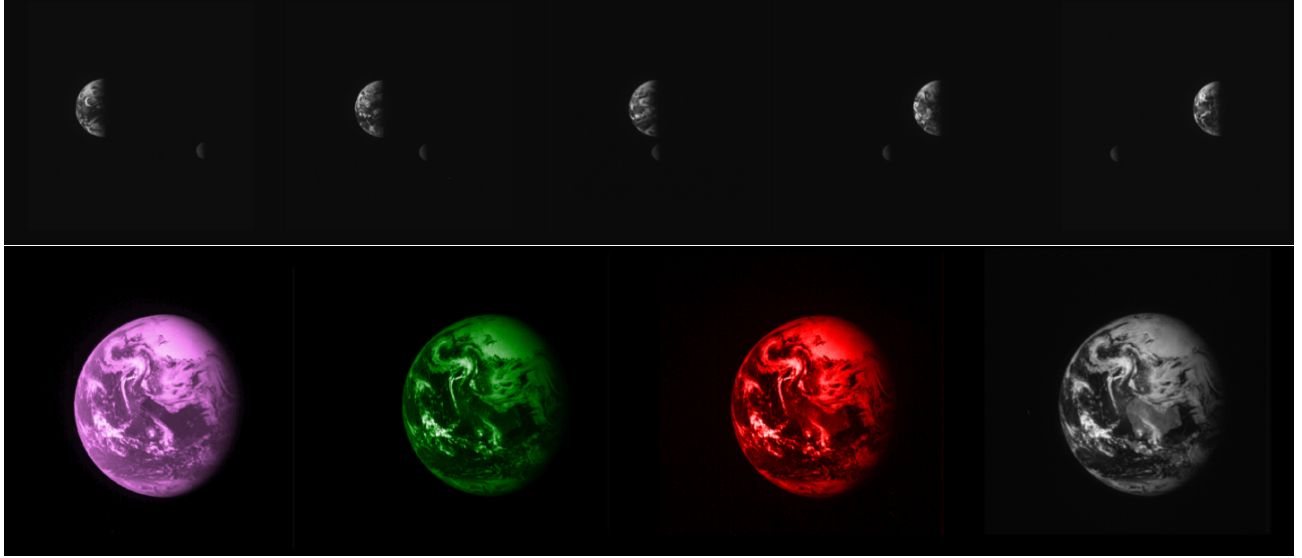


Fig. 4.— Top: Time sequence of Earth and the Moon acquired with the SSI “infrared” filter (961–1011 nm) after the second *Galileo* flyby (December, 1992). Bottom: Images of Earth acquired with the SSI from the first *Galileo* flyby (December, 1990). Filters from left to right are violet (382–427 nm), green (527–592 nm), red (641–701 nm), and “infrared”. The sub-observer point in each image is approximately identical, and Australia is the landmass near the center of the images. For all images south is oriented “up,” as it was in the true flyby geometry.

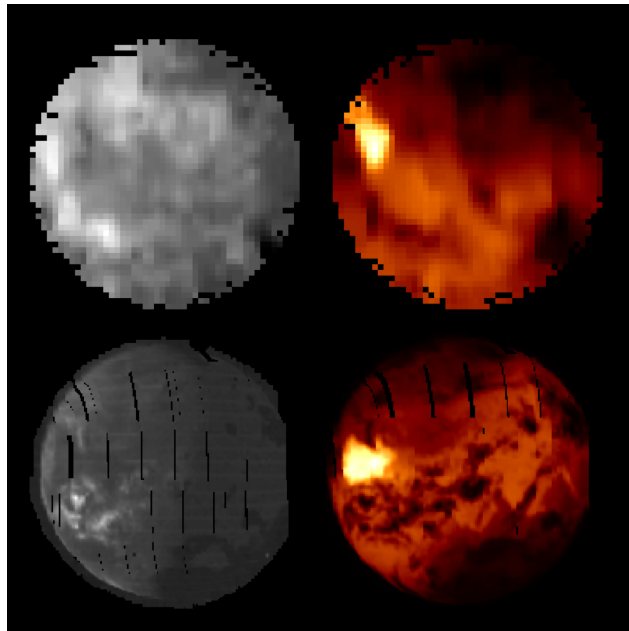


Fig. 5.— Reconstructed images of Earth using NIMS observations from the first (top) and second (bottom) *Galileo* Earth flybys. Images in the left column are at $2.75\ \mu\text{m}$ while images in the right column are at $4.0\ \mu\text{m}$. The bright (warm) source seen in both $4.0\ \mu\text{m}$ images is likely Australia. The spacecraft was nearer to Earth in the second flyby dataset, thereby providing better resolution across the disk.

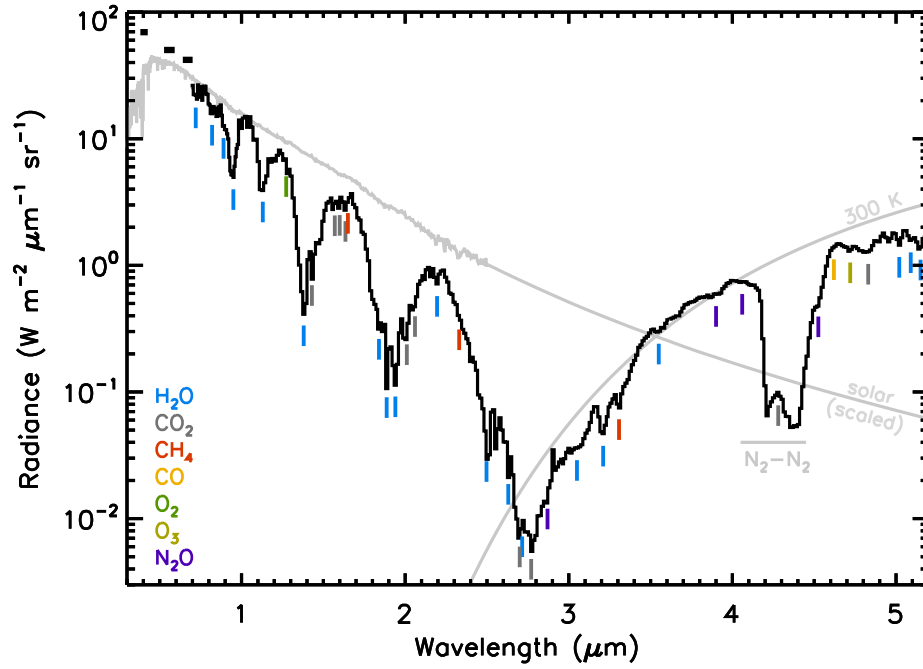


Fig. 6.— Spatially-resolved spectrum of Earth from the second *Galileo* flyby, acquired for a small region of the planet in the Indian Ocean and near the terminator at the time of observation. Visible SSI photometry (in the violet, green, and red filters) and NIMS spectroscopy are both shown, and key absorption bands are indicated. Reflected light contributes significantly below about 3 μm , while thermal emission dominates at longer wavelengths. Light gray curves indicate a scaled solar spectrum and a 300 K blackbody.

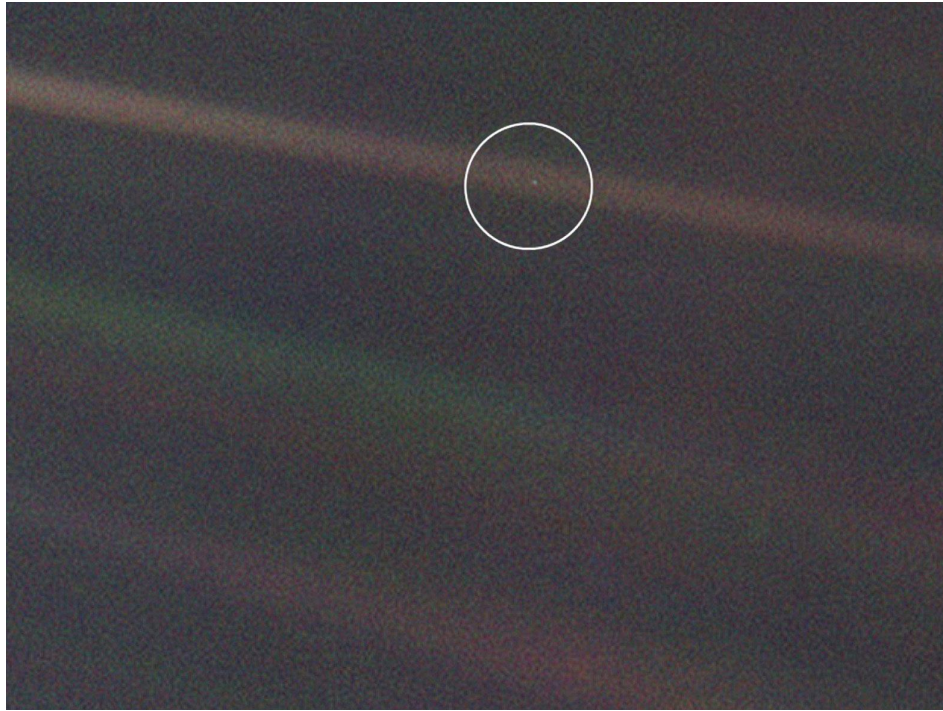


Fig. 7.— The famous “Pale Blue Dot” image of Earth, acquired by the *Voyager 1* spacecraft from a distance of 40 au. Image credit: NASA/JPL-Caltech.

4.2.1. Earthshine

Using Earthshine from the dark portion of the Moon — which is illuminated by Earth but not the Sun — has a long history of revealing key details about our planet. In the *Dialogue Concerning the Two Chief World Systems*, Galileo used Earthshine to deduce that “seas would appear darker, and [...] land brighter” when observed from a distance (Galilei 1632). In the first multi-year Earthshine monitoring experiment, described in Danjon (1928) and continued by Dubois (1947), the broadband visual reflectivity of Earth was shown to vary by several tens of percent at a given phase angle (i.e., the planet-star-observer angle), and cloud variability was identified as the likely driver of these variations.

Modern Earthshine observations (Goode et al. 2001; Woolf et al. 2002; Pallé et al. 2004b) have reached an impressive level of precision. Achieving this precision requires corrections for airmass effects, the lunar phase function (i.e., how the Moon scatters light into varied directions), and variations in reflectivity across the lunar surface. Nevertheless, it is now common for Earthshine measurements to achieve 1% precision on a given night (Qiu et al. 2003). Such high-quality photometric observations have revealed variability in the visible reflectivity of Earth at daily, monthly, seasonal, and decadal timescales (Goode et al. 2001; Pallé et al. 2003, 2004a, 2009a; Pallé et al. 2016). Figure 8 shows a collection of phase-dependent visual (400–700 nm) apparent albedo measurements from Earthshine measurements. Apparent albedo (A_{app}) is defined by normalizing an observed planetary flux to that from a perfectly reflecting Lambert sphere (i.e., a sphere whose surface reflects light equally well into all directions) observed at the same phase angle, or,

$$A_{\text{app}} = \frac{3 F_p}{2 F_s} \frac{\pi}{\sin \alpha + (\pi - \alpha) \cos \alpha}, \quad (1)$$

where α is the star-planet-observer (i.e., phase) angle, F_p is the emergent planetary flux at the top of the atmosphere, F_s is the solar/stellar flux at normal incidence on the top of the planetary atmosphere, and the flux quantities can either be wavelength-dependent (resulting in a wavelength-dependent apparent albedo) or integrated. (Note that the factor of $3/2$ comes from the conversion between geometric and spherical albedo.) Thus, a Lambert sphere would have a constant apparent albedo as a function of phase. Critically, then, the non-constant apparent albedo of Earth demonstrated in Figure 8 reveals a weak back scattering peak at small phase angles, a region of Lambert-like scattering at intermediate phase angles, and a strong forward scattering peak at large phase angles.

Spectroscopic studies of Earthshine (Woolf et al. 2002) offer additional insights into Earth as an exoplanet (Figure 9), beyond those obtained through photometric Earthshine investigations. Using spectroscopic Earthshine data collected over several weeks or months, Arnold et al. (2002)

and Seager et al. (2005) showed that the aforementioned vegetation red edge signature is variable in the reflectance spectrum of Earth, and can lead to sharp reflectivity increases at the 10% level in the 600–800 nm range. A red edge-focused Earthshine study by Montañés-Rodríguez et al. (2006) found no strong signature in spectroscopic data from a single night, which highlighted the importance of cloud cover both in setting the overall brightness of Earth and in masking surface reflectance features. In Earthshine observations that spanned 0.7–2.4 μm , Turnbull et al. (2006) noted a plethora of absorption features that were indicative of life, habitability, and geological activity. Also, after accounting for how the lunar surface de-polarizes radiation, polarization-sensitive spectroscopic Earthshine observations have explored the degree to which a spectrum of Earth can be polarized (0–20%, depending on wavelength) as well as the impact of cloud cover on this signature (Sterzik et al. 2012; Miles-Páez et al. 2014). Finally, by investigating the Earthshine spectrum at extremely high spectral resolution ($\lambda/\Delta\lambda$; also referred to as the spectral resolving power) González-Merino et al. (2013) uncovered narrow spectral features due to atomic sodium in Earth’s atmosphere that are either of terrestrial or meteoritic origin.

Of course, Earth-like planets around other stars may not be solely investigated using reflected-light techniques (e.g., Snellen et al. 2013), especially in the case of potentially habitable worlds orbiting M dwarf hosts where transit or secondary eclipse observations would be the preferred approach. Impressively, observational techniques developed for Earthshine data collection have been re-purposed to enable observations of the transmission spectrum of Earth’s atmosphere. By observing the Moon during a lunar eclipse, Pallé et al. (2009b) were able to measure light that had been transmitted through our atmosphere and reflected by the lunar surface. These observations revealed signatures of key atmospheric and biosignature gases, and even included narrow features due to ionized calcium as well as broad pressure-induced features from O_2 and N_2 (the latter of which is typically difficult to detect due to its general lack of rotational-vibrational features). A follow-up analysis of these data by García Muñoz et al. (2012) showed that refractive effects in transit spectra of Earth twins would limit the atmospheric depths probed (during mid-transit) to be above about 10 km, thus providing limited information from the surface and tropospheric environments. Also, additional high-resolution transmission spectra acquired using Earthshine-related techniques have revealed variability in the depths of H_2O absorption features (Yan et al. 2015), likely tied to the condensable nature of this gas in our atmosphere.

Finally, while Earthshine techniques have been proven to be both powerful and versatile, this approach does have its shortcomings. First, due to the ground-based nature of the observations, full diurnal cycles in the reflectivity of Earth cannot be observed except during polar night (Briot et al. 2013). Second, it is often difficult to calibrate Earthshine observations in a fashion that reveals the absolute bright-

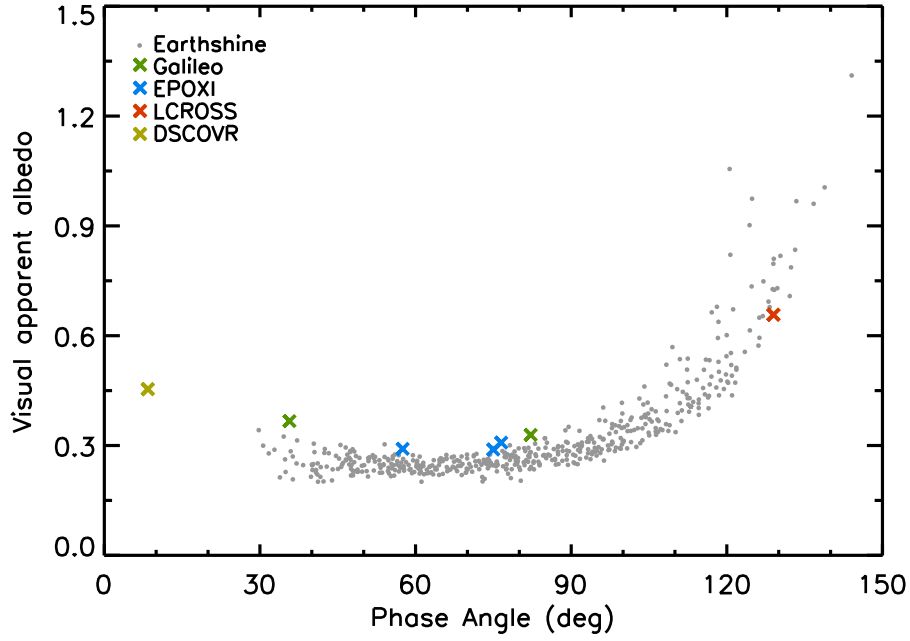


Fig. 8.— Measurements of the phase-dependent visual (400–700 nm) apparent albedo of Earth from Earthshine data spanning several years (from Pallé et al. 2003), and from several spacecraft missions. Apparent albedo values larger than unity indicate stronger directional scattering than can be produced by a sphere whose surface reflects light isotropically (i.e., a Lambert sphere). The *DSCOVR* datapoint is derived from the available four narrowband channels that span the visible range since an integrated 400–700 nm observation cannot be produced from *DSCOVR* data.

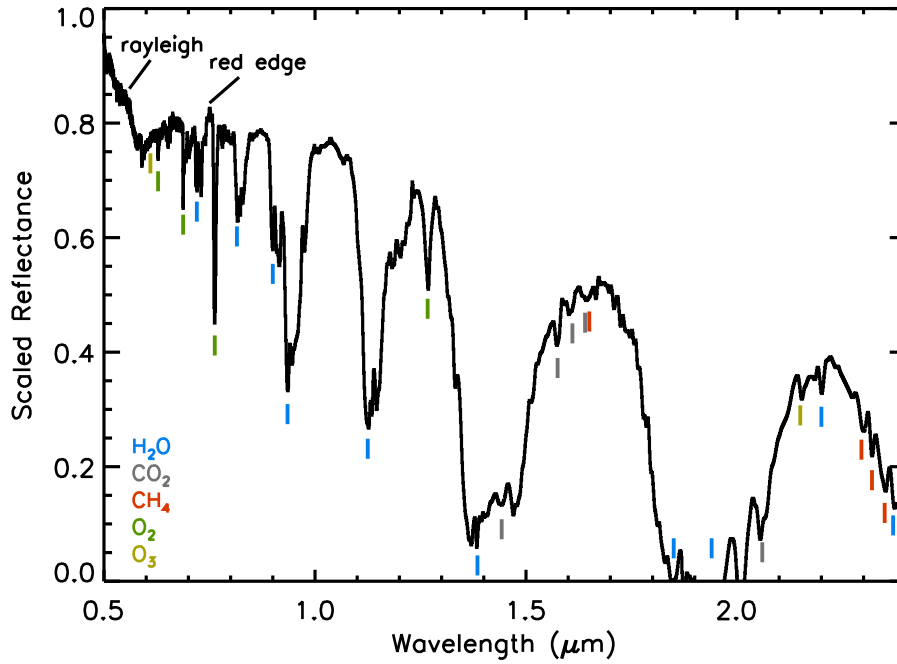


Fig. 9.— Scaled reflectance spectrum of Earth at visible and near-infrared wavelengths measured from Earthshine. Key absorption and reflection features are indicated. Data courtesy M. Turnbull from Turnbull et al. (2006).

ness of our planet. Thus, some Earthshine datasets are only reported as a scaled reflectance value, and these products are of lower utility when it comes to exoplanet detectability and characterization studies. Finally, Earthshine cannot be used to observe thermal emission from Earth since the Moon is also self-luminous at infrared wavelengths.

4.2.2. Orbit

A large suite of satellites are continuously monitoring the Earth system from space. While most of these Earth-observing satellites only resolve a small patch of our planet in any individual observation, the collective dataset from these satellites benefits from extensive temporal, spatial, and spectral coverage. Thus “stitching” together spatially-resolved radiance measurements from one (or several) observing platform(s) can enable a view of the entire disk of Earth. This approach was pioneered by Hearty et al. (2009), who used spatially-resolved thermal radiance observations from the Atmospheric Infrared Sounder (AIRS) instrument (aboard NASA’s *Aqua* satellite; Aumann et al. 2003) to create disk-integrated infrared spectra of Earth (Figure 10).

The practice of stitching together resolved radiance measurements from an Earth-observing satellite is, unfortunately, not straightforward. Temporal gaps sometimes exist in these datasets where a given latitude/longitude patch of Earth has not been observed in a given 24 hr period. Thus, if the goal is to produce a snapshot of Earth at a given time, an interpolation of existing radiance observations across time must be performed. As the Earth climate system (as well as top-of-atmosphere radiances) is non-linear, this interpolation introduces some uncertainties.

The greater challenge to deriving whole-Earth views from resolved satellite observations, though, stems from viewing geometry constraints. Most Earth-observing satellites are designed to acquire observations in the nadir (i.e., direct downward) direction. For satellites observing in reflected light, the range of solar incidence angles can also be limited, especially over any given several-day period. Thus, when stitching together a whole-disk observation, data for certain viewing geometries (e.g., patches located near the limb, where the observing geometry is quite distinct from nadir-looking) may not exist. In this case, assumptions must be adopted for how radiance will vary with the emission angle and/or the solar incidence angle. For example, Hearty et al. (2009) adopted a limb darkening law to transform radiances acquired at nadir to radiances appropriate for other emission angles.

An alternative approach to using directly-observed radiances from satellites is, instead, to adopt a collection of satellite-derived “scene” models. These scene models describe the viewing geometry-dependent brightness of different surface categories for Earth (e.g., ocean or desert) under different cloud coverage scenarios. In other words, these models specify the bi-directional reflectance distribution

functions for a large variety of surface type and cloud coverage combinations. Scene models can be derived from satellite observations (Suttles et al. 1988) or can be designed to fit satellite observations (Manalo-Smith et al. 1998). Combining data that describe the time-dependent distribution of clouds, snow, and ice on Earth with a set of scene models then enables the recreation of whole-disk views of our planet (Ford et al. 2001; Pallé et al. 2003; Oakley & Cash 2009). Integrating these three-dimensional models over the planetary disk then yields the brightness (or reflectivity) of the Pale Blue Dot. One key shortcoming of the scene model approach, however, is that such models are rarely spectrally resolved, and instead specify a broadband reflectivity or brightness. Thus, such models cannot produce spectra of the disk-integrated Earth, and, instead, focus on computing broadband lightcurves for the Pale Blue Dot.

Solar occultation observations acquired from Earth orbit provide a direct measurement of the transmittance along a slant path through the atmosphere. Initially such datasets (Abrams et al. 1999; Bovensmann et al. 1999; Bernath et al. 2005) provided an excellent model validation for tools designed to simulate transit spectra of Earth-like exoplanets (Kaltenegger & Traub 2009; Misra et al. 2014b). However, as was recognized by Robinson et al. (2014) and Dalba et al. (2015), occultation observations from orbit can be directly translated into transit spectra. Using data from the Canadian Atmospheric Chemistry Experiment - Fourier Transform Spectrometer (ACE-FTS; Bernath et al. 2005), Schreier et al. (2018) created transit spectra of Earth spanning 2.2–13.3 μm and demonstrated that signatures of chlorofluorocarbons appeared in the occultation-derived transit observations, in addition to more-standard features of H_2O , CO_2 , CH_4 , N_2O , N_2 , NO_2 , and O_2 (see also, Macdonald & Cowan 2019).

4.2.3. Spacecraft

The ideal approach for mimicking direct observations of Earth-like exoplanets is, of course, to acquire photometry and/or spectroscopy for a truly distant Earth. Such observations must be taken from distances beyond low-Earth or geostationary orbit, as the entire disk of the planet is not entirely visible from these vantages (e.g., only about 85% of the disk is observable from geostationary orbit). Thus, views of Earth from spacecraft at lunar distances or from Earth-Sun Lagrange points, or observations from interplanetary spacecraft, are all excellent sources. Until the recent launch of the Deep Space Climate Observatory (DSOVR; Biesecker et al. 2015) mission to the Earth-Sun L1 point, no dedicated mission existed for observing Earth from a great distance. Thus, the majority of the spacecraft observations relevant to Earth as an exoplanet came from missions sent to other Solar System worlds.

While spacecraft observations of the distant Earth are ideal for exoplanet-themed investigations, this approach is not without its shortcomings. First, it is difficult to find time

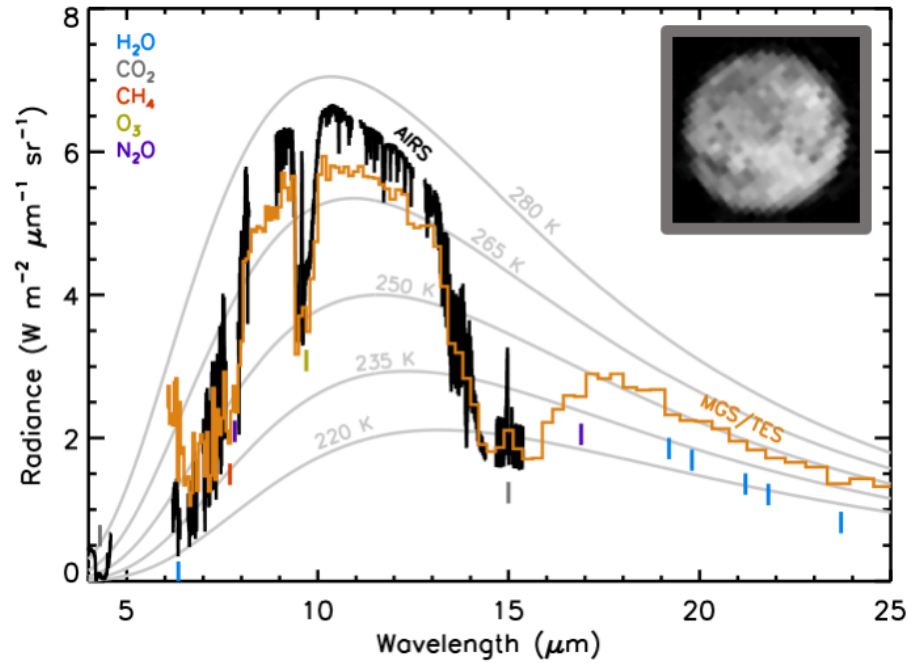


Fig. 10.— Disk-integrated thermal infrared spectra of Earth from the AIRS instrument (Hearty et al. 2009) and from the *Mars Global Surveyor* Thermal Emission Spectrometer (MGS/TES; Christensen & Pearl 1997), where differences are due to the combined effects of seasons, climate, clouds, and viewing geometry. Key features are labeled and blackbody spectra at different emitting temperatures are shown. Inset is a broadband thermal infrared (6–10 μm) image of Earth from the *LCROSS* mission (Robinson et al. 2014).

during the main phase of a mission to dedicate towards observations of non-primary targets such as Earth. This means that the temporal coverage of spacecraft datasets for the distant Earth is poor, with many of these datasets acquired during the cruise phase of a mission. Second, and most unfortunately, spacecraft datasets for the distant Earth often remain unpublished. In these circumstances, the data may have been acquired only for press or outreach purposes, or it might be that analysis and publication of these data are seen as a distraction from the main goals of a mission. Unpublished datasets are known to exist (both from private communications and press releases) for a number of other missions including: *Cassini*, *Clementine*, *Lunar Reconnaissance Orbiter*, *Mars Express*, *Mars Reconnaissance Orbiter*, *MESSENGER*, *OSIRIS-REx*, *SELENE/Kaguya*, and *Venus Express*.

A detailing of published spacecraft-acquired datasets that are relevant to Earth as an exoplanet is shown in Table 3, emphasizing photometric and spectroscopic observations that span the ultraviolet, visible, and infrared wavelengths. Beyond the previously-discussed *Galileo* Earth flyby observations, key datasets also come from a snapshot thermal infrared spectrum acquired by the *Mars Global Surveyor* Thermal Emission Spectrometer (MGS/TES), visible photometry and near-infrared spectroscopy spanning 24 hr on five separate dates from the *EPOXI* mission (which repurposed the *Deep Impact* flyby spacecraft), visible spectroscopy and infrared photometry and spectroscopy taken over brief intervals on three separate dates by the *Lunar*

Crater Observation and Sensing Satellite (LCROSS), and the aforementioned *DSCOVR* data (which include images taken in 10 narrowband channels spanning ultraviolet and visible wavelengths, and bolometric measurements in several channels spanning 0.2–100 μm). The *EPOXI* dataset has been used to analyze key spectral features for Earth in the near-infrared range and to quantify the vegetation red edge signature in disk-integrated observations (Livenood et al. 2011; Robinson et al. 2011), and to investigate mapping techniques for unresolved objects (Cowan et al. 2009; Fujii et al. 2011; Cowan et al. 2011). In Robinson et al. (2014), the *LCROSS* Earth observations were used to quantify the impact of ocean glint and ozone absorption on phase-dependent disk-integrated visible spectroscopic data for the Pale Blue Dot. A digest of ultraviolet, visible, and near-infrared observations is shown in Figure 11.

Finally, while existing datasets have made many valuable contributions to our understanding of the appearance of the Pale Blue Dot, major gaps still exist in our observational coverage. Regarding Table 3, it is obvious that spacecraft observations of Earth in reflected light at crescent phases (i.e., phase angles from roughly 145–180°) are lacking — only a single dataset, from the *LCROSS* mission (Robinson et al. 2014), exists for all phase angles beyond quadrature (which occurs at a phase angle of 90°, where the planet is half illuminated). Thermal infrared observations at moderate to high spectral resolution are also not represented. Additionally, no datasets span a continuous timeframe of longer than roughly 24 hr, which hinders studies of rota-

tional variability. Lastly, excepting the few *LCROSS* pointings (Robinson et al. 2014), existing visible-wavelength datasets only contain photometry, so spectroscopy below about 1 μm is not well represented.

5. MODELING THE PALE BLUE DOT

Techniques for simulating observations of the distant Earth provide a complementary approach to spacecraft, orbital, and Earthshine observations. Especially once validated against observational datasets, models of the disk-integrated Earth enable the exploration of the Pale Blue Dot across a wide range of wavelengths and spectral resolutions, and can also fill in the various gaps that exist between different observational approaches. Currently, a hierarchy of Earth models exists, spanning simple reflectance tools to complex three-dimensional models whose outputs cover the ultraviolet through the far-infrared.

5.1. One-Dimensional Approaches

One-dimensional models of the Pale Blue Dot capture the vertical structure of Earth’s atmosphere, but omit any latitudinal or longitudinal structure in the atmosphere and surface. Such simplifications enable these one-dimensional approaches to be computationally efficient, and often allow for higher spectral resolution in model outputs. Nevertheless, key details about the fractional distribution of clouds and various surface types on Earth must be accounted for, either through data-informed weighting factors or through tuning parameters.

Traub & Jucks (2002) presented one of the earliest models of the Pale Blue Dot. This one-dimensional tool spanned the ultraviolet through thermal infrared, and included absorption and emission from key atmospheric species. Radiation multiple scattering was neglected, and modeled observations in reflected light were generated by linearly combining spectral components (including Rayleigh, clear sky, high cloud, and others). At visible wavelengths, disk-integrated observations were simulated using a single solar zenith angle (i.e., the Sun was placed at a zenith angle of 60° over a plane-parallel atmosphere). Both Woolf et al. (2002) and Turnbull et al. (2006) used the Traub & Jucks (2002) model to analyze Earthshine spectra. By fitting the reflected-light spectral components in the Traub & Jucks (2002) model to the Earthshine data, these authors determined that the most important aspects of their reflected-light observations were a clearsky component, a gray high cloud continuum, and Rayleigh scattering. More recently, the Traub & Jucks (2002) model has been used to study the spectral evolution of Earth through time (Kaltenegger et al. 2007; Rugheimer & Kaltenegger 2018), including a comparison to the previously mentioned *EPOXI* dataset (Rugheimer et al. 2013).

A multiple-scattering one-dimensional model, developed by Martín-Torres et al. (2003), was adopted by Montañés-Rodríguez et al. (2006) to help understand the signature of the vegetation red edge in Earthshine spectra. In this work, the good match between the Earthshine data and the simulations was attributed to the scattering treatment within the model. Also, the Montañés-Rodríguez et al. (2006) study developed a sophisticated approach to capturing the latitudinal and longitudinal distribution of clouds and surface types on Earth. Specifically, disk-averaged cloud and surface coverage maps were derived from Earth science data products, including appropriate weighting factors for the solar and lunar geometry.

5.2. Three-Dimensional Models

In general, three-dimensional models of the Pale Blue Dot compute the spatially-resolved radiance over the planetary disk, and then integrate this radiance over solid angle to produce a disk-integrated quantity. More formally, three-dimensional models of Earth aim to compute the integral of the projected area weighted intensity in the direction of an observer, which is written as,

$$F_\lambda(\hat{\mathbf{o}}, \hat{\mathbf{s}}) = \frac{R_E^2}{d^2} \int_{2\pi} I_\lambda(\hat{\mathbf{n}}, \hat{\mathbf{o}}, \hat{\mathbf{s}}) (\hat{\mathbf{n}} \cdot \hat{\mathbf{o}}) d\omega, \quad (2)$$

where F_λ is the disk-integrated specific flux density received from a world of radius R_E at a distance d from the observer, $I_\lambda(\hat{\mathbf{n}}, \hat{\mathbf{o}}, \hat{\mathbf{s}})$ is the location-dependent specific intensity in the direction of the observer, $d\omega$ is an infinitesimally small unit of solid angle on the globe, $\hat{\mathbf{n}}$ is a surface normal unit vector for the portion of the surface corresponding to $d\omega$, and $\hat{\mathbf{o}}$ and $\hat{\mathbf{s}}$ are unit vectors in the direction of the observer and the Sun, respectively (see Figure 12). The integral in Equation 2 is over the entire observable hemisphere (2π steradians) and the dot product at the end of the expression ensures that an element of area $R_E^2 d\omega$ near the limb is weighted less than an element of equal size near the sub-observer point. Note that, for reflected light, I_λ will be zero at locations on the night side of the world (i.e., where $\hat{\mathbf{n}} \cdot \hat{\mathbf{s}} < 0$), but is non-zero at all locations when considering thermal emission.

The most straightforward (quasi) three-dimensional models use empirical bi-directional reflectance distribution functions (e.g., the previously-mentioned scene models from Manalo-Smith et al. 1998) to specify the reflectivity of a patch on the disk as a function of viewing geometry. These three-dimensional tools can either be spectrally-resolved (Ford et al. 2001) or broadband (McCullough 2006; Pallé et al. 2003, 2008; Williams & Gaidos 2008; Oakley & Cash 2009). Atmospheric effects (e.g., gas absorption and scattering) are typically omitted, although Fujii et al. (2010) produced a three-dimensional reflectance model that blended wavelength-dependent bi-directional reflectance distribution functions from a variety of sources

TABLE 3
PUBLISHED SPACECRAFT DATASETS FOR EARTH AS AN EXOPLANET

Spacecraft	Date ^a	Phase Angle(s)	Wavelength (μm)	Resolution ^b	Source(s)
<i>Galileo</i>	1990-12-10	35°	0.38–5.2	Δλ = 0.01–0.44 μm (vis)	Sagan et al. (1993); Drossart et al. (1993)
	1992-12-09	82°		Δλ = 0.025 μm (NIR)	
	1992-12-16	89°			
<i>MGS/TES</i>	1996-11-23	n/a	6–50	— λ/Δλ = 15–170	Christensen & Pearl (1997)
<i>EPOXI</i>	2008-03-18	58°	0.37–4.54	Δλ ≈ 0.1 μm (vis)	Livengood et al. (2011); Cowan et al. (2011); Fujii et al. (2011); Robinson et al. (2011)
	2008-05-28	75°			
	2008-06-04	77°		λ/Δλ = 215–730 (NIR)	
	2009-03-27	87°			
	2009-10-04	86°			
<i>LCROSS</i>	2009-08-01	23°	0.26–13.5	— λ/Δλ = 300–800 (vis)	Robinson et al. (2014)
	2009-08-17	129°		Δλ = 0.3, 0.8 μm (NIR)	
	2009-09-18	75°		Δλ = 4, 7.5 μm (thermal)	
<i>DSCOVR</i>	ongoing	4–12°	0.318–0.780	— Δλ = 1–3 nm	Biesecker et al. (2015); Yang et al. (2018)

^aBased on UT at start of observations.

^bAbbreviating visible range ($\sim 0.4\text{--}1\ \mu\text{m}$) as “vis” and near-infrared range ($\sim 1\text{--}5\ \mu\text{m}$) as “NIR.”

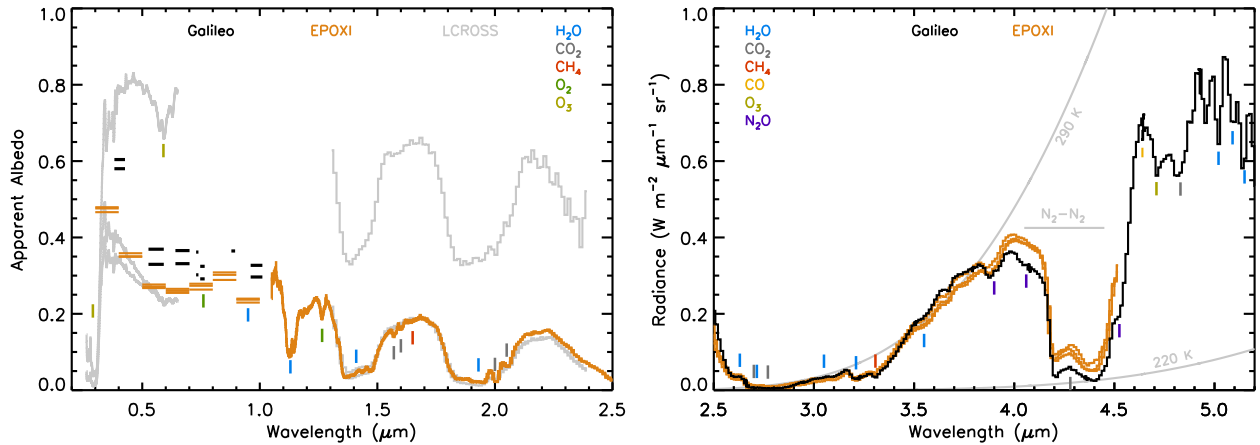


Fig. 11.— Summary of published observations of the distant Earth at ultraviolet, visible, and near-infrared wavelengths. The first figure presents spectra of Earth’s apparent albedo from *Galileo* (Sagan et al. 1993), *EPOXI* (Livengood et al. 2011), and *LCROSS* (Robinson et al. 2014). A crescent-phase observation from *LCROSS* is marked by large apparent albedo, which was driven primarily by forward scattering from a glint spot. The second figure presents near-infrared emission observations from *Galileo* and *EPOXI*, and blackbody spectra are provided. Key absorption features are indicated in both figures.

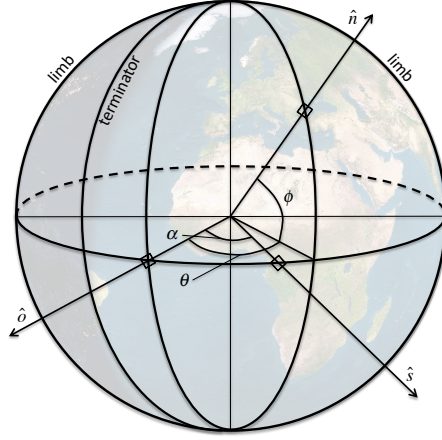


Fig. 12.— Geometry for modeling disk-integrated Earth observations. The surface normal vector, and the vectors in the direction of the observer and Sun are \hat{n} , \hat{o} , and \hat{s} , respectively. The angle α is the phase angle, while ϕ and θ are the coordinates of latitude and longitude, respectively. Earth view generated by the Earth and Moon Viewer, first implemented by J. Walker (<http://www.fourmilab.ch/cgi-bin/Earth>).

and also included an additive atmospheric Rayleigh scattering term. Time-dependent distributions of clouds and surface types are derived from Earth science datasets, such as the International Satellite Cloud Climatology Project (ISCCP; Schiffer & Rossow 1983).

The most complex three-dimensional tools for simulating observations of the distant Earth solve the full plane-parallel, multiple-scattering radiative transfer equation to determine the emergent radiance over the planetary disk. By including realistic atmospheric radiative effects, these fully multiple-scattering tools can more self-consistently capture gas and cloud absorption and scattering (Tinetti et al. 2006; Fujii et al. 2011; Robinson et al. 2011; Feng et al. 2018) as well as polarization effects (Stam 2008). Like the previously-discussed reflectance models, cloud and surface type coverages are typically derived from Earth science datasets, while cloud optical thicknesses must also be adopted from similar datasets to include in the multiple-scattering calculation. Such sophisticated three-dimensional models can serve as virtual “laboratories” for studying the Pale Blue Dot across a wide range of timescales, wavelengths, and viewing geometries (see Figure 13), insofar as they are validated against observations (that, admittedly, do not span all possible combinations of planetary phase, wavelength coverage, and spectral resolution; see Section 4). In any case, our observational analysis and models of the Pale Blue Dot must also be extended to confront the realization that Earth’s major characteristics and remotely observable properties have changed considerably throughout the course of planetary evolution.

6. DECIPHERING EXO-EARTH OBSERVATIONS

The observations and models discussed in previous sections provide insights into remote sensing approaches to understanding distant habitable worlds. At wavelengths spanning the ultraviolet through the infrared, and for both broadband photometry and spectroscopy across a range of resolutions, data (or simulated data) for the distant Earth — at any of its evolutionary stages — contain a great deal of information about the planetary environment. The sections below discuss the information content of observations of reflected light and of thermal emission. Additional information can be found in reviews by Meadows (2008), Kaltenegger et al. (2010), Kaltenegger et al. (2012), and Robinson (2018).

6.1. Visible Photometry

Single-instance broadband photometry of a distant Earth-like world provides limited information about the planetary environment. As Earthshine observations have shown (Qiu et al. 2003; Pallé et al. 2003), photometric data could constrain planetary albedo — which is central to an understanding of planetary energy balance — as long as planetary size and phase are known. (If the planetary radius is unknown, the planetary reflectivity and size are degenerate, although see Section 6.3 for a discussion of using thermal infrared observations to constrain the planetary radius.) Additionally, broad absorption features can be detected using photometric observations (e.g., as was the case for the 950 nm H_2O band in *EPOXI* observations; Livengood et al. 2011), although constraining atmospheric abundances from

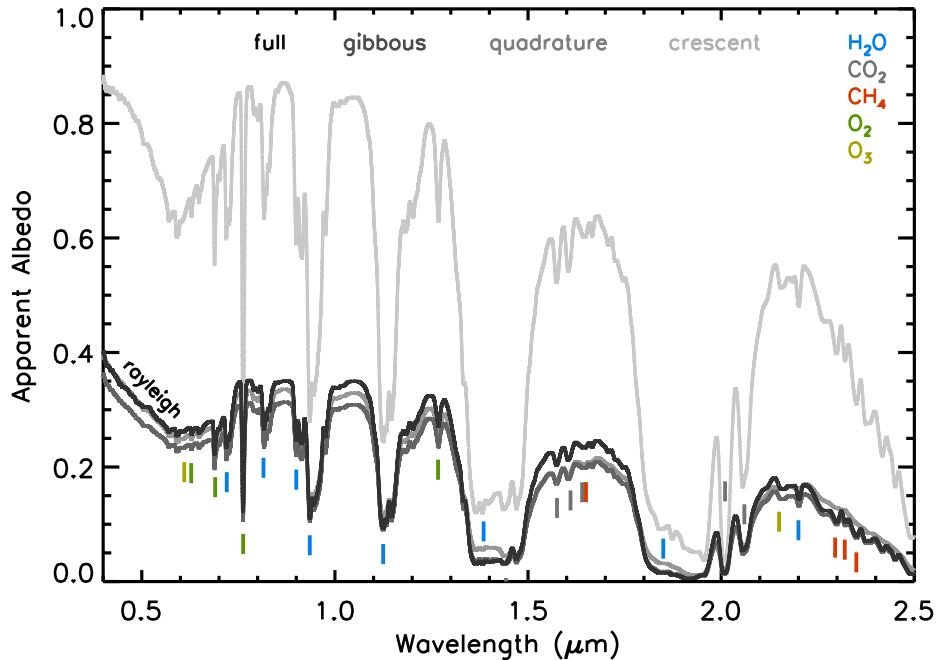


Fig. 13.— Simulations of Earth’s phase- and wavelength-dependent apparent albedo (from Robinson et al. 2010). Models are averaged over a full rotation at each phase, and the angles of the given phases are 0° (full), 45° (gibbous), 90° (quadrature), and 135° (crescent). Large apparent albedos at crescent phase are primarily due to ocean glint and cloud forward scattering. The similarity in apparent albedo scales for the quadrature, gibbous, and full spectra indicate that Earth largely scatters like a Lambert sphere across these phase angles. A slight enhancement in apparent albedo at full phase is due to cloud back scattering.

low-resolution observations is extremely challenging (Lupu et al. 2016). Planetary color derived from broadband observations has been suggested as a means of identifying exo-Earth candidates (Traub 2003), and, regarding Figure 3, visible photometry could differentiate a hazy Archean Earth from a non-hazy Earth at all other evolutionary stages, even at low signal-to-noise. Distinguishing our planet from certain non-Earth-like planets might be more problematic for Earth at any geological phase other than the Phanerozoic (Krissansen-Totton et al. 2016b) and could be confused by planetary phase effects as well as our lack of knowledge on realistic colors of temperate or cool exoplanets.

Disk-integrated photometric observations that resolve the rotation of an exo-Earth yield much more powerful diagnostics than single-instance photometry (Figure 14). When acquired over multiple days (rotations), the rotation rate of the planet can be determined from diurnal variability (which is typically 10–20%; Ford et al. 2001; Livenood et al. 2011), even in the presence of evolving weather patterns (Pallé et al. 2008; Oakley & Cash 2009). Once the rotation rate of an exo-Earth is known, the correspondence between time and sub-observer longitude enables longitudinally-resolved mapping (Cowan et al. 2009; Fujii et al. 2010; Kawahara & Fujii 2010; Fujii et al. 2011; Fujii & Kawahara 2012; Cowan & Strait 2013; Lustig-Yaeger et al. 2018), although degeneracies can occur in mapping approaches, especially with regard to spectral unmixing (Fujii et al. 2017). Additionally, studying photometric vari-

ability inside absorption bands of well-mixed gases (e.g., O_2) as compared to variability inside bands of other species (e.g., H_2O) can reveal condensation processes in planetary atmospheres (Fujii et al. 2013). Depending on the optical thickness of a potential haze in the atmosphere of the Archean Earth (Arney et al. 2016), it might be necessary to push photometric observations to red or near-infrared wavelengths to have surface and near-surface sensitivity in lightcurves.

Photometric exo-Earth observations resolved at both rotational and orbital timescales could reveal additional information about the planetary surface. Due to the obliquity of the planetary rotational axis (that could be constrained from lightcurves; Schwartz et al. 2016; Kawahara 2016), and depending on orbital inclination, maps resolved in latitude and longitude could be produced from high-quality data (Fujii & Kawahara 2012; Cowan et al. 2013). Even in the absence of rotationally-resolved photometry, surface oceans — whose presence directly confirms the habitability of an exoplanet — could be detected via the effect of specular reflectance on a planetary phase curve (McCullough 2006; Williams & Gaidos 2008), especially at red and near-infrared wavelengths where observations at large phase angles are less strongly impacted by Rayleigh scattering and, thus, have better surface sensitivity (Robinson et al. 2010; Zugger et al. 2011) (observations at these wavelengths would also be less influenced by any hazes on the Archean Earth; Arney et al. 2016). Additionally, scattering at the Brewster angle will

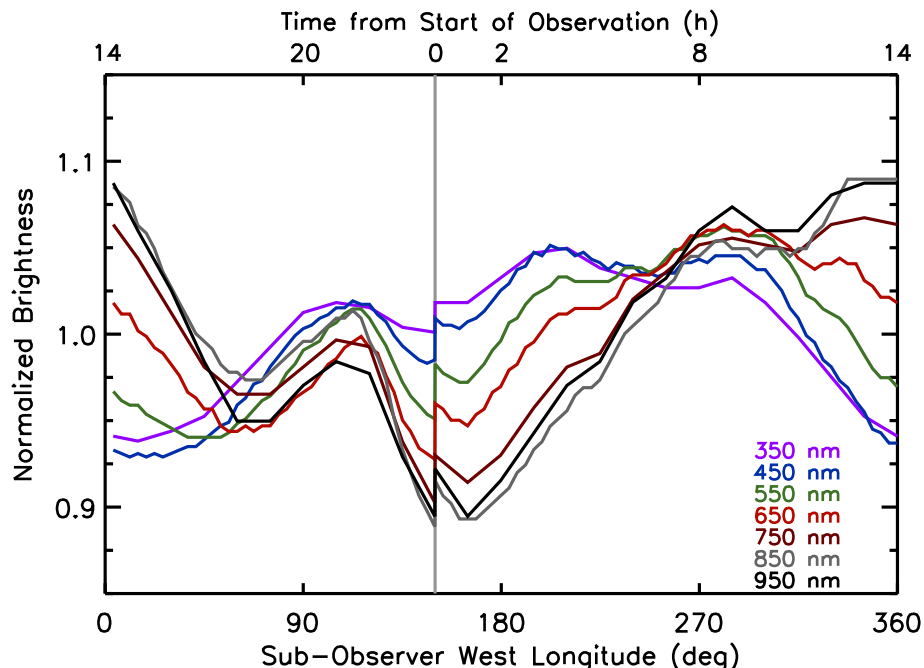


Fig. 14.— Full-rotation lightcurves for Earth from the March 2008 *EPOXI* dataset in all shortwave filters. Filter bandpasses are 100 nm wide, and filter center wavelengths are indicated. Overall brightness is driven largely by clouds at shorter wavelengths and by both clouds and continents at longer wavelengths (Robinson et al. 2011). Variability is primarily due to Earth’s rotation, however differences in brightness after a full rotation are due to longer-term evolution of cloud patterns.

maximize the polarization signature from an exo-ocean and could be detected in the polarization phase curve of an exo-Earth (McCullough 2006; Stam 2008; Williams & Gaidos 2008; Zugger et al. 2010). Finally, polarization and reflectance phase curves for Earth-like exoplanets can also reveal cloud properties through scattering effects (Bailey 2007; Karalidi et al. 2011, 2012; Karalidi & Stam 2012), although little work has been done to understand how photochemical hazes (e.g., like those that may have been present on the Archean Earth) would impact polarimetric observations.

6.2. Visible Spectroscopy

Spectroscopic observations in reflected light provide powerful information about the atmospheric and surface environment of the Pale Blue Dot at any stage in its evolution. In addition to the insights offered from photometry (as spectra can always be degraded to lower resolution), observations at even moderate spectral resolution enable the detection of trace atmospheric gases. For example, Drossart et al. (1993) used near-infrared *Galileo* data to constrain the abundances of CO_2 , H_2O , CO , O_3 , CH_4 , and N_2O in the atmosphere of Earth. While the Drossart et al. (1993) study used spatially-resolved observations, the same gaseous absorption features appear in the disk-integrated *EPOXI* dataset (Livengood et al. 2011).

Beyond trace gas detection, spectroscopic reflected-light observations can also constrain atmospheric pressure — a

key determinant of habitability — through Rayleigh scattering effects, broadening of gas absorption lines and bands, and through collision-induced absorption and dimer features. Pressure-induced absorption features due to O_2 and N_2 occur throughout the near-infrared (and into the mid-infrared; Misra et al. 2014a; Schwieterman et al. 2015). Of course, interpretation of Rayleigh scattering features and pressure-broadened absorption bands is not straightforward. The former depends on surface gravity and atmospheric mean molecular weight and can be masked by surface or haze absorption at blue wavelengths (see Figure 3), while the latter is impacted by the composition of the background atmosphere (e.g., Hedges & Madhusudhan 2016). However, despite difficulties associated with detection, constraining O_2 and N_2 levels in the atmosphere of an Earth-like exoplanet would be key to deciphering the disequilibrium signature of $\text{N}_2\text{-O}_2\text{-H}_2\text{O}$ (Krissansen-Totton et al. 2016a).

Feng et al. (2018) investigated retrievals of planetary and atmospheric properties for the modern Pale Blue Dot from visible-wavelength (0.4–1.0 μm) spectroscopy at a variety of spectral resolutions and signal-to-noise ratios. Here, firm constraints on key gas mixing ratios (for H_2O , O_3 , and O_2), total atmospheric pressure, and planetary radius could be achieved with simulated Earth observations at a V-band signal-to-noise ratio of 20 and spectral resolution of 140. Thus, observations of this quality for modern exo-Earth twin could be sufficient to indicate that the planet is either super-Earth or Earth-sized and that O_2 is a major

atmospheric constituent, which is strong evidence that the planet may be inhabited.

Low resolution, low signal-to-noise ultraviolet observations of an Earth-like planet could rapidly distinguish the ozone-free Archean Earth from Earth at different evolutionary stages, and the ultraviolet Hartley-Huggins band may have exhibited dramatic seasonal variations during the Proterozoic (Olson et al. 2018a). For the Archean, spectral models have demonstrated strong features due to methane and haze (Arney et al. 2016), but retrieval investigations have yet to show how observations of different quality and wavelength coverage could be used to infer methane and haze concentrations for an Archean Earth-like exoplanet. Here, and as opposed to a haze-free Earth, planetary radius may be difficult to constrain from reflected light observations as the size determination relies strongly on measuring a Rayleigh scattering feature. (Since the Rayleigh scattering properties of a gas are well-defined, the planet-to-star flux ratio in a Rayleigh scattering feature is dependent primarily on the planetary size and orbital distance.)

6.3. Thermal Infrared Observations

Owing to the great technical challenges posed by techniques for observing Earth-like planets around Sun-like stars at long wavelengths, relatively little attention has been focused on understanding disk-integrated observations of our planet at thermal infrared wavelengths. Nevertheless, infrared spectra of the distant Earth — even at relatively low spectral resolution — provide a great deal of information about the atmospheric and surface environment. Most fundamentally, and unlike reflected-light data, infrared observations can directly constrain the radius of an exo-Earth. The flux received from a true blackbody depends on its temperature, size, and distance. If the distance to a target star is known, and with the temperature constrained via Wien’s displacement law, the size of a planet can then be determined from low-resolution thermal infrared observations. Of course, Earth does not emit like a true blackbody, which would introduce some uncertainty into a fitted planetary radius.

Beyond planetary size, infrared gas absorption features, by definition, reveal the key greenhouse gases of a planetary atmosphere. For Earth, observations (Figure 10) plainly reveal signatures of CO₂, H₂O, O₃, CH₄, and N₂O (Christensen & Pearl 1997; Hearty et al. 2009). Regarding our evolving planet, the 9.7 μ m ozone band becomes apparent in Earth’s emission spectrum after the rise of oxygen and the carbon dioxide bands at 9.4, 10.4, and 15 μ m strongly track decreasing atmospheric CO₂ levels with time (Meadows 2008; Rugheimer & Kaltenegger 2018). Critically, these would be observable at modest resolving powers and characteristic spectral signal-to-noise ratios of 5 (Rugheimer & Kaltenegger 2018). Additionally, pressure-induced absorption features can be used to indicate bulk atmospheric composition and pressure, and one such feature

from N₂ has been detected in observations of the distant Earth near 4 μ m (Schwieterman et al. 2015).

Critically, as molecular absorption bands are pressure broadened, and because high-opacity regions of a molecular band probe lower atmospheric pressures than do low-opacity regions, infrared observations can be used to probe the thermal structure of the atmosphere and surface of an exo-Earth. This idea would apply for Earth at any stage in its evolution, even for a hazy Archean Earth as such hydrocarbon aerosols are typically transparent at infrared wavelengths (Arney et al. 2016). Finally, thermal infrared lightcurves could also reveal variability due to weather (and associated condensational processes), rotation, and seasons (Hearty et al. 2009; Selsis et al. 2011; Robinson 2011; Gómez-Leal et al. 2012; Cowan et al. 2012).

Using spatially-resolved *Galileo*/NIMS Earth observations, along with adopted *a priori* knowledge of total atmospheric pressure and the CO₂ mixing ratio, Drossart et al. (1993) derived the thermal structures of cloud-free regions on Earth from the 4.3 μ m CO₂ band. More recently, von Paris et al. (2013) used retrieval techniques on simulated infrared observations of a distant, modern Earth to show that low-resolution ($\lambda/\Delta\lambda = 20$) observations at signal-to-noise ratios of 10–20 could constrain thermal structure and atmospheric composition reasonably well. However, like the Drossart et al. (1993) retrievals, the results from von Paris et al. (2013) emphasize a cloud-free atmosphere. Thus, it remains unclear how realistic patchy clouds would influence our ability to understand the atmosphere and surface of an exo-Earth from thermal infrared observations, and how this might impact attempts to characterize exo-Earths in different thermal states (e.g., a snowball state versus a clement or hothouse state).

7. SUMMARY

Exoplanetary science is rapidly progressing towards its long-term goal of discovering and characterizing Earth-like planets around our nearest stellar neighbors. We now know that exoplanets, including potentially habitable Earth-sized worlds, are quite common, and small worlds orbiting within the Habitable Zone of nearby cool stars have already been discovered. Advances in observational technologies, especially with regards to exoplanet direct imaging techniques, will enable the detection of Pale Blue Dots around other stars, potentially in the not-too-distant future.

Flybys of Earth by the *Galileo* spacecraft in the early 1990s enabled the remote detection of habitability and life on our planet using planetary science remote sensing techniques. A combination of spatially-resolved visible and near-infrared spectral observations argued conclusively for the presence of liquid water on Earth’s surface. These same datasets indicated an atmosphere that was in a state of strong chemical disequilibrium — a sign of life — and observations at radio wavelengths contained features that indicated the presence of intelligent organisms.

More recently, a variety of observational approaches have yielded datasets that, effectively, allow us to view Earth as a distant exoplanet. While observations from spacecraft at or beyond the Moon’s orbit are ideal for understanding habitability and life signatures from the Pale Blue Dot, such data are rarely acquired. Critically, satellite and Earthshine observations complement, and fill in certain gaps between, spacecraft data for the distant Earth.

Beyond observational datasets, models have proved effective tools for simulating and characterizing Earth as an exoplanet. These tools span a wide range of complexities, including one-dimensional (vertical) spectral simulators, simple reflectance tools that capture the broadband reflectivity of Earth at visible wavelengths, and complex three-dimensional models that can simulate observations of the distant Earth at arbitrary viewing geometry across wavelengths that span the ultraviolet through the thermal infrared. Especially in the absence of frequent spacecraft observations, models of the Pale Blue Dot can serve as testing grounds for proposed approaches to detecting and characterizing Earth-like exoplanets.

Geological and bio-geochemical studies of the long-term evolution of Earth reveal a world that, while being continuously habitable and inhabited, has progressed through a variety of surface and atmospheric states. Abundances of key atmospheric constituents, including biosignature gases, have varied by many orders of magnitude. As these gases imprint information about their concentrations on spectra of Earth, applying the aforementioned spectral simulation tools to the Pale Blue Dot at different geologic epochs reveals planetary spectra (and associated biosignatures) quite distinct from modern Earth. Especially for the Archean Earth, the term “Pale Blue Dot” may not even apply.

Combining an understanding of remote sensing techniques relevant to exoplanets with knowledge of the conditions on the current and ancient Earth yields insights into approaches for detecting and studying Earth-like worlds around other stars. Broadband observations have the potential to reveal habitable environments on ocean-bearing exoplanets, and time-resolved photometry can be used to extract spatial information from spatially-unresolved data. More powerfully, spectroscopic observations at moderate resolutions can uncover key details about the surface and atmospheric state on a potentially Earth-like planet, including fundamental details relevant to life detection. Only by uncovering the key signatures that indicate the habitability and inhabitation of Earth — at any point in its evolution — can we properly design the observational tools needed to discover and fully characterize other Earths.

Acknowledgments. This research has made use of the Planetary Data System (PDS) and USGS Integrated Software for Imagers and Spectrometers (ISIS). TR gratefully acknowledges support from NASA through the Sagan Fellowship Program executed by the NASA Exoplanet Science Institute and through the Exoplanets Research Program (award #80NSSC18K0349). Both TR and CR would like to acknowledge support from the NASA Astrobiology

Institute, both through a grant to the Virtual Planetary Laboratory (under Cooperative Agreement No. NNA13AA93A) and to the University of California, Riverside “Alternative Earths” team. The results reported herein benefited from collaborations and/or information exchange within NASA’s Nexus for Exoplanet System Science (NExSS) research coordination network sponsored by NASA’s Science Mission Directorate. We thank M. Turnbull, P. Christensen, T. Hearty, E. Pallé, E. Schwieterman, and G. Arney for openly sharing data used in this chapter. Both authors also thank V. Meadows, G. Arney, N. Cowan and an anonymous reviewer for detailed and constructive comments on versions of this manuscript.

REFERENCES

- Abrams, M. C., Goldman, A., Gunson, M. R., Rinsland, C. P., & Zander, R. (1999). Observations of the Infrared Solar Spectrum from Space by the ATMOS Experiment. *Appl. Opt.*, *35*, 2747.
- Anglada-Escudé, G., Amado, P. J., Barnes, J., Berdiñas, Z. M., Butler, R. P., Coleman, G. A. L., de La Cueva, I., Dreizler, S., Endl, M., Giesers, B., Jeffers, S. V., Jenkins, J. S., Jones, H. R. A., Kiraga, M., Kürster, M., López-González, M. J., Marvin, C. J., Morales, N., Morin, J., Nelson, R. P., Ortiz, J. L., Ofir, A., Paardekooper, S.-J., Reiners, A., Rodríguez, E., Rodríguez-López, C., Sarmiento, L. F., Strachan, J. P., Tsapras, Y., Tuomi, M., & Zechmeister, M. (2016). A terrestrial planet candidate in a temperate orbit around Proxima Centauri. *Nature*, *536*, 437–440.
- Arney, G., Domagal-Goldman, S. D., Meadows, V. S., Wolf, E. T., Schwieterman, E., Charnay, B., Claire, M., Hébrard, E., & Trainer, M. G. (2016). The Pale Orange Dot: The Spectrum and Habitability of Hazy Archean Earth. *Astrobiology*, *16*, 873–899.
- Arney, G. N., Domagal-Goldman, S. D., & Meadows, V. S. (2018). Organic Haze as a Biosignature in Anoxic Earth-like Atmospheres. *Astrobiology*, *18*, 311–329.
- Arnold, L., Gillet, S., Lardiére, O., Riaud, P., & Schneider, J. (2002). A test for the search for life on extrasolar planets. Looking for the terrestrial vegetation signature in the Earthshine spectrum. *Astron. Astrophys.*, *392*, 231–237.
- Aumann, H. H., Chahine, M. T., Gautier, C., Goldberg, M. D., Kalnay, E., McMillin, L. M., Revercomb, H., Rosenkranz, P. W., Smith, W. L., Staelin, D. H., Strow, L. L., & Susskind, J. (2003). AIRS/AMSU/HSB on the aqua mission: design, science objectives, data products, and processing systems. *IEEE Transactions on Geoscience and Remote Sensing*, *41*, 253–264.
- Azmy, K., Kendall, B., Creaser, R. A., Heaman, L., & de Oliveira, T. F. (2008). Global correlation of the Vazante

- Group, São Francisco Basin, Brazil: Re-Os and U-Pb radiometric age constraints. *Precambrian Research*, 164, 160–172.
- Bachan, A., & Kump, L. R. (2015). The rise of oxygen and siderite oxidation during the Lomagundi Event. *Proceedings of the National Academy of Science*, 112, 6562–6567.
- Bailey, J. (2007). Rainbows, Polarization, and the Search for Habitable Planets. *Astrobiology*, 7, 320–332.
- Baker, A. L., Baker, L. R., Beshore, E., Blenman, C., Castillo, N. D., Chen, Y.-P., Doose, L. R., Elston, J. P., Fountain, J. W., & Goffeen, D. L. (1975). The imaging photopolarimeter experiment on Pioneer 11. *Science*, 188, 468–472.
- Barstow, J. K., Aigrain, S., Irwin, P. G. J., Kendrew, S., & Fletcher, L. N. (2016). Telling twins apart: exo-Earths and Venuses with transit spectroscopy. *Mon. Not. R. Astron. Soc.*, 458, 2657–2666.
- Bartdorff, O., Wallmann, K., Latif, M., & Semenov, V. (2008). Phanerozoic evolution of atmospheric methane. *Global Biogeochemical Cycles*, 22, GB1008.
- Batalha, N., Kalirai, J., Lunine, J., Clampin, M., & Lindler, D. (2015). Transiting Exoplanet Simulations with the James Webb Space Telescope. *ArXiv e-prints*, 1507:02655.
- Batalha, N. M. (2014). Exploring exoplanet populations with NASA's Kepler Mission. *Proceedings of the National Academy of Science*, 111, 12647–12654.
- Bean, J. L., Kempton, E. M.-R., & Homeier, D. (2010). A ground-based transmission spectrum of the super-earth exoplanet gj 1214b. *Nature*, 468(7324), 669–672.
- Beerling, D., Berner, R. A., Mackenzie, F. T., Harfoot, M. B., & Pyle, J. A. (2009). Methane and the CH₄ related greenhouse effect over the past 400 million years. *American Journal of Science*, 309, 97–113.
- Beichman, C., Benneke, B., Knutson, H., Smith, R., Lagage, P.-O., Dressing, C., Latham, D., Lunine, J., Birkmann, S., Ferruit, P., et al. (2014). Observations of transiting exoplanets with the James Webb Space Telescope (JWST). *PASP*, 126(946), 1134–1173.
- Bekker, A. (2001). Chemostratigraphy of the Paleoproterozoic Duitschland Formation, South Africa: implications for coupled climate change and carbon cycling. *American Journal of Science*, 301, 261–285.
- Bekker, A., & Holland, H. D. (2012). Oxygen overshoot and recovery during the early Paleoproterozoic. *Earth and Planetary Science Letters*, 317, 295–304.
- Belcher, C. M., & McElwain, J. C. (2008). Limits for Combustion in Low O₂ Redefine Paleoaotmospheric Predictions for the Mesozoic. *Science*, 321, 1197.
- Bellefroid, E.J., v. S. Hood, A., Hoffman, P.F., Thomas, M.D., Reinhard, C.T. & Planavsky, N.J. (2018). Constraints on Paleoproterozoic atmospheric oxygen levels. *Proceedings of the National Academy of Sciences, USA*, 115, 8104–8109.
- Belton, M. J. S., Klaasen, K. P., Clary, M. C., Anderson, J. L., Anger, C. D., Carr, M. H., Chapman, C. R., Davies, M. E., Greeley, R., & Anderson, D. (1992). The Galileo Solid-State Imaging Experiment. *Space Sci. Rev.*, 60, 413–455.
- Bergman, N. M. (2004). COPSE: A new model of biogeochemical cycling over Phanerozoic time. *American Journal of Science*, 304, 397–437.
- Bernath, P. F., McElroy, C. T., Abrams, M. C., Boone, C. D., Butler, M., Camy-Peyret, C., Carleer, M., Clerbaux, C., Coheur, P.-F., Colin, R., DeCola, P., DeMazière, M., Drummond, J. R., Dufour, D., Evans, W. F. J., Fast, H., Fussen, D., Gilbert, K., Jennings, D. E., Llewellyn, E. J., Lowe, R. P., Mahieu, E., McConnell, J. C., McHugh, M., McLeod, S. D., Michaud, R., Midwinter, C., Nassar, R., Nichitiu, F., Nowlan, C., Rinsland, C. P., Rochon, Y. J., Rowlands, N., Semeniuk, K., Simon, P., Skelton, R., Sloan, J. J., Soucy, M.-A., Strong, K., Tremblay, P., Turnbull, D., Walker, K. A., Walkty, I., Wardle, D. A., Wehrle, V., Zander, R., & Zou, J. (2005). Atmospheric Chemistry Experiment (ACE): Mission overview. *Geophys. Res. Lett.*, 32, L15S01.
- Berner, R. A. (1991). A model for atmospheric CO₂ over Phanerozoic time. *American Journal of Science*, 291, 339–376.
- Berner, R. A. (2006). Geological nitrogen cycle and atmospheric N₂ over Phanerozoic time. *Geology*, 34, 413.
- Bianchi, D., Dunne, J. P., Sarmiento, J. L., Galbraith, E. D. (2012). Data-based estimates of suboxia, denitrification, and N₂O production in the ocean and their sensitivities to dissolved O₂. *Global Biogeochemical Cycles*, 26.
- Biesecker, D. A., Reinard, A., Cash, M. D., Johnson, J., Burek, M., de Koning, C. A., Szabo, A., Koval, A., Kasper, J. C., Stevens, M. L., Case, A. W., Berberich, K., & Mulligan, P. (2015). Presenting DSCOVR: The First NOAA Mission to Leave Earth Orbit. *AGU Fall Meeting Abstracts*, (pp. SH12A–06).
- Blake, R. E., Chang, S. J., & Lepland, A. (2010). Phosphate oxygen isotopic evidence for a temperate and biologically active Archaean ocean. *Nature*, 464, 1029–1032.
- Borucki, W. J., Koch, D., Basri, G., Batalha, N., Brown, T., Caldwell, D., Caldwell, J., Christensen-Dalsgaard, J.,

- Cochran, W. D., DeVore, E., Dunham, E. W., Dupree, A. K., Gautier, T. N., Geary, J. C., Gilliland, R., Gould, A., Howell, S. B., Jenkins, J. M., Kondo, Y., Latham, D. W., Marcy, G. W., Meibom, S., Kjeldsen, H., Lissauer, J. J., Monet, D. G., Morrison, D., Sasselov, D., Tarter, J., Boss, A., Brownlee, D., Owen, T., Buzasi, D., Charbonneau, D., Doyle, L., Fortney, J., Ford, E. B., Holman, M. J., Seager, S., Steffen, J. H., Welsh, W. F., Rowe, J., Anderson, H., Buchhave, L., Ciardi, D., Walkowicz, L., Sherry, W., Horch, E., Isaacson, H., Everett, M. E., Fischer, D., Torres, G., Johnson, J. A., Endl, M., MacQueen, P., Bryson, S. T., Dotson, J., Haas, M., Kolodziejczak, J., Van Cleve, J., Chandrasekaran, H., Twicken, J. D., Quintana, E. V., Clarke, B. D., Allen, C., Li, J., Wu, H., Tenenbaum, P., Verner, E., Bruhweiler, F., Barnes, J., & Prsa, A. (2010). Kepler Planet-Detection Mission: Introduction and First Results. *Science*, 327, 977–.
- Bovensmann, H., Burrows, J. P., Buchwitz, M., Frerick, J., Noël, S., Rozanov, V. V., Chance, K. V., & Goede, A. P. H. (1999). SCIAMACHY: Mission Objectives and Measurement Modes. *Journal of Atmospheric Sciences*, 56, 127–150.
- Briot, D., Arnold, L., & Jacquemoud, S. (2013). Present and Future Observations of the Earthshine from Antarctica. In M. G. Burton, X. Cui, & N. F. H. Tothill (Eds.) *Astrophysics from Antarctica*, vol. 288 of *IAU Symposium*, (pp. 214–217).
- Brown, T. M. (2001). Transmission spectra as diagnostics of extrasolar giant planet atmospheres. *The Astrophysical Journal*, 553(2), 1006.
- Budyko, M. I. (1969). The effect of solar radiation variations on the climate of the earth. *Tellus*, 21, 611–619.
- Buick, R. (2007). Did the proterozoic Canfield ocean cause a laughing gas greenhouse? *Geobiology*, 5(2), 97–100.
- Burke, C. J., Christiansen, J. L., Mullally, F., Seader, S., Huber, D., Rowe, J. F., Coughlin, J. L., Thompson, S. E., Catanzarite, J., Clarke, B. D., Morton, T. D., Caldwell, D. A., Bryson, S. T., Haas, M. R., Batalha, N. M., Jenkins, J. M., Tenenbaum, P., Twicken, J. D., Li, J., Quintana, E., Barclay, T., Henze, C. E., Borucki, W. J., Howell, S. B., & Still, M. (2015). Terrestrial Planet Occurrence Rates for the Kepler GK Dwarf Sample. *Astrophys. J.*, 809, 8.
- Burrows, A. (2014). Scientific Return of Coronagraphic Exoplanet Imaging and Spectroscopy Using WFIRST. *ArXiv e-prints*, 1412.6097.
- Canfield, D. E. (2005). THE EARLY HISTORY OF ATMOSPHERIC OXYGEN: Homage to Robert M. Garrels. *Annual Review of Earth and Planetary Sciences*, 33, 1–36.
- Canfield, D. E., Ngombi-Pemba, L., Hammarlund, E. U., Bengtson, S., Chaussidon, M., Gauthier-Lafaye, F., Menunier, A., Riboulleau, A., Rollion-Bard, C., Rouxel, O., Asael, D., Pierson-Wickmann, A.-C., & El Albani, A. (2013). Oxygen dynamics in the aftermath of the Great Oxidation of Earth's atmosphere. *Proceedings of the National Academy of Science*, 110, 16736–16741.
- Canfield, D. E., Poulton, S. W., & Narbonne, G. M. (2007). Late-Neoproterozoic Deep-Ocean Oxygenation and the Rise of Animal Life. *Science*, 315, 92.
- Carlson, R. W., Weissman, P. R., Smythe, W. D., & Mahoney, J. C. (1992). Near-Infrared Mapping Spectrometer Experiment on Galileo. *Space Sci. Rev.*, 60, 457–502.
- Cash, W., Schindhelm, E., Arenberg, J., Lo, A., Polidan, R., Kasdin, J., Vanderbei, R., Kilston, S., & Noecker, C. (2007). External Occulters for Direct Observation of Exoplanets: An Overview. In *UV/Optical/IR Space Telescopes: Innovative Technologies and Concepts III*, vol. 6687 of *Proc. SPIE*, (p. 668712).
- Cassan, A., Kubas, D., Beaulieu, J. P., Dominik, M., Horne, K., Greenhill, J., Wambsganss, J., Menzies, J., Williams, A., Jorgensen, U. G., Udalski, A., Bennett, D. P., Albrow, M. D., Batista, V., Brilliant, S., Caldwell, J. A. R., Cole, A., Coutures, C., Cook, K. H., Dieters, S., Prester, D. D., Donatowicz, J., Fouque, P., Hill, K., Kains, N., Kane, S., Marquette, J. B., Martin, R., Pollard, K. R., Sahu, K. C., Vinter, C., Warren, D., Watson, B., Zub, M., Sumi, T., Szymanski, M. K., Kubiak, M., Poleski, R., Soszynski, I., Ulaczyk, K., Pietrzynski, G., & Wyrzykowski, L. (2012). One or more bound planets per milky way star from microlensing observations. *Nature*, 481(7380), 167–169.
- Catling, D. C. (2006). Comment on "A Hydrogen-Rich Early Earth Atmosphere". *Science*, 311, 38a.
- Catling, D. C., & Claire, M. W. (2005). How Earth's atmosphere evolved to an oxic state: A status report. *Earth and Planetary Science Letters*, 237, 1–20.
- Catling, D. C., Claire, M. W., & Zahnle, K. J. (2007). Anaerobic methanotrophy and the rise of atmospheric oxygen. *Philosophical Transactions of the Royal Society of London Series A*, 365, 1867–1888.
- Catling, D. C., Zahnle, K. J., & McKay, C. P. (2001). Biogenic Methane, Hydrogen Escape, and the Irreversible Oxidation of Early Earth. *Science*, 293, 839–843.
- Charbonneau, D., Brown, T. M., Noyes, R. W., & Gilliland, R. L. (2002). Detection of an Extrasolar Planet Atmosphere. *Astrophys. J.*, 568, 377–384.
- Charnay, B., Forget, F., Wordsworth, R., Leconte, J., Millour, E., Codron, F., & Spiga, A. (2013). Exploring the faint young Sun problem and the possible climates of the

- Archean Earth with a 3-D GCM. *Journal of Geophysical Research (Atmospheres)*, 118, 10.
- Charnay, B., Le Hir, G., Fluteau, F., Forget, F., & Catling, D. C. (2017). A warm or a cold early Earth? New insights from a 3-D climate-carbon model. *Earth and Planetary Science Letters*, 474, 97–109.
- Christensen, P. R., & Pearl, J. C. (1997). Initial data from the Mars Global Surveyor thermal emission spectrometer experiment: Observations of the Earth. *J. Geophys. Res.*, 102, 10875–10880.
- Claire, M. W., Catling, D. C., & Zahnle, K. J. (2006). Biogeochemical modeling of the rise in atmospheric oxygen. *Geobiology*, 4, 239–269.
- Cole, D. B., Reinhard, C. T., Wang, X., Gueguen, B., Halverson, G. P., Gibson, T., Hodgskiss, M. S. W., McKenzie, N. R., Lyons, T. W., & Planavsky, N. J. (2016). A shale-hosted Cr isotope record of low atmospheric oxygen during the Proterozoic. *Geology*, 44, 555–558.
- Cowan, N. B., Agol, E., Meadows, V. S., Robinson, T., Livengood, T. A., Deming, D., Lisse, C. M., A'Hearn, M. F., Wellnitz, D. D., Seager, S., Charbonneau, D., & the EPOXI Team (2009). Alien Maps of an Ocean-bearing World. *Astrophys. J.*, 700, 915–923.
- Cowan, N. B., Fuentes, P. A., & Haggard, H. M. (2013). Light curves of stars and exoplanets: estimating inclination, obliquity and albedo. *Mon. Not. R. Astron. Soc.*, 434, 2465–2479.
- Cowan, N. B., Greene, T., Angerhausen, D., Batalha, N. E., Clampin, M., Colón, K., Crossfield, I. J. M., Fortney, J. J., Gaudi, B. S., Harrington, J., Iro, N., Lillie, C. F., Linsky, J. L., Lopez-Morales, M., Mandell, A. M., & Stevenson, K. B. (2015). Characterizing Transiting Planet Atmospheres through 2025. *PASP*, 127, 311–327.
- Cowan, N. B., Robinson, T., Livengood, T. A., Deming, D., Agol, E., A'Hearn, M. F., Charbonneau, D., Lisse, C. M., Meadows, V. S., Seager, S., Shields, A. L., & Wellnitz, D. D. (2011). Rotational Variability of Earth's Polar Regions: Implications for Detecting Snowball Planets. *Astrophys. J.*, 731, 76–.
- Cowan, N. B., & Traut, T. E. (2013). Determining Reflectance Spectra of Surfaces and Clouds on Exoplanets. *Astrophys. J. Lett.*, 765, L17.
- Cowan, N. B., Voigt, A., & Abbot, D. S. (2012). Thermal Phases of Earth-like Planets: Estimating Thermal Inertia from Eccentricity, Obliquity, and Diurnal Forcing. *Astrophys. J.*, 757, 80.
- Cox, G. M., Halverson, G. P., Minarik, W. G., Le Heron, D. P., Macdonald, F. A., Bellefroid, E. J., & Strauss, J. V. (2013). Neoproterozoic iron formation: An evaluation of its temporal, environmental and tectonic significance. *Chemical Geology*, 362, 232–249.
- Crowe, S. A., Paris, G., Katsev, S., Jones, C., Kim, S.-T., Zerkle, A. L., Nomosatryo, S., Fowle, D. A., Adkins, J. F., Sessions, A. L., Farquhar, J., & Canfield, D. E. (2014). Sulfate was a trace constituent of Archean seawater. *Science*, 346, 735–739.
- Daines, S. J., & Lenton, T. M. (2016). The effect of widespread early aerobic marine ecosystems on methane cycling and the Great Oxidation. *Earth and Planetary Science Letters*, 434, 42–51.
- Daines, S. J., Mills, B. J. W., & Lenton, T. M. (2017). Atmospheric oxygen regulation at low Proterozoic levels by incomplete oxidative weathering of sedimentary organic carbon. *Nature Communications*, 8, 14379.
- Dalba, P. A., Muirhead, P. S., Fortney, J. J., Hedman, M. M., Nicholson, P. D., & Veyette, M. J. (2015). The Transit Transmission Spectrum of a Cold Gas Giant Planet. *Astrophys. J.*, 814, 154.
- Danjon, A. (1928). Recherches sur la photométrie de la lumière cendrée et l'albedo de la terre. *Ann. Obs. Strasbourg*, 2, 165–180.
- de Wit, J., Wakeford, H. R., Lewis, N. K., Delrez, L., Gillon, M., Selsis, F., Leconte, J., Demory, B.-O., Bolmont, E., Bourrier, V., Burgasser, A. J., Grimm, S., Jehin, E., Lederer, S. M., Owen, J. E., Stamenković, V., & Triaud, A. H. M. J. (2018). Atmospheric reconnaissance of the habitable-zone Earth-sized planets orbiting TRAPPIST-1. *Nature Astronomy*, 2, 214–219.
- de Wit, M. J., & Furnes, H. (2016). 3.5-Ga hydrothermal fields and diamictites in the Barberton Greenstone Belt–Paleoarchean crust in cold environments. *Science Advances*, 2, e1500368–e1500368.
- Delabroye, A., & Vecoli, M. (2010). The end-Ordovician glaciation and the Hirnantian Stage: A global review and questions about Late Ordovician event stratigraphy. *Earth Science Reviews*, 98, 269–282.
- Deming, D., Seager, S., Winn, J., Miller-Ricci, E., Clampin, M., Lindler, D., Greene, T., Charbonneau, D., Laughlin, G., Ricker, G., Latham, D., & Ennico, K. (2009). Discovery and Characterization of Transiting Super Earths Using an All-Sky Transit Survey and Follow-up by the James Webb Space Telescope. *PASP*, 121, 952–967.
- Des Marais, D. J., Harwit, M. O., Jucks, K. W., Kasting, J. F., Lin, D. N. C., Lunine, J. I., Schnieder, J., Seager, S., Traub, W. A., Woolf, N. J. (2002). Remote sensing of planetary properties and biosignatures on extrasolar terrestrial planets. *Astrobiology*, 2, 153–181.

- DeWitt, H. L., Trainer, M. G., Pavlov, A. A., Hasenkopf, C. A., Aiken, A. C., Jimenez, J. L., McKay, C. P., Toon, O. B., & Tolbert, M. A. (2009). Reduction in Haze Formation Rate on Prebiotic Earth in the Presence of Hydrogen. *Astrobiology*, 9, 447–453.
- Diamond-Lowe, H., Stevenson, K. B., Bean, J. L., Line, M. R., & Fortney, J. J. (2014). New Analysis Indicates No Thermal Inversion in the Atmosphere of HD 209458b. *Astrophys. J.*, 796, 66.
- Domagal-Goldman, S. D., Kasting, J. F., Johnston, D. T., & Farquhar, J. (2008). Organic haze, glaciations and multiple sulfur isotopes in the Mid-Archean Era. *Earth and Planetary Science Letters*, 269, 29–40.
- Doughty, C. E., & Wolf, A. (2010). Detecting Tree-like Multicellular Life on Extrasolar Planets. *Astrobiology*, 10, 869–879.
- Doughty, C. E., & Wolf, A. (2016). Detecting 3D Vegetation Structure with the Galileo Space Probe: Can a Distant Probe Detect Vegetation Structure on Earth? *PLoS ONE*, 11, e0167188.
- Dressing, C. D., & Charbonneau, D. (2013). The Occurrence Rate of Small Planets around Small Stars. *Astrophys. J.*, 767, 95.
- Dressing, C. D., & Charbonneau, D. (2015). The occurrence of potentially habitable planets orbiting M dwarfs estimated from the full Kepler dataset and an empirical measurement of the detection sensitivity. *Astrophys. J.*, 807, 45.
- Driese, S. G., Jirsa, M. A., Ren, M., Brantley, S. L., Sheldon, N. D., Parker, D., & Schmitz, M. (2011). Neoproterozoic paleoweathering of tonalite and metabasalt: Implications for reconstructions of 2.69Ga early terrestrial ecosystems and paleoatmospheric chemistry. *Precambrian Research*, 189, 1–17.
- Drossart, P., Rosenqvist, J., Encrenaz, T., Lellouch, E., Carlson, R. W., Baines, K. H., Weissman, P. R., Smythe, W. D., Kamp, L. W., & Taylor, F. W. (1993). Earth global mosaic observations with NIMS-Galileo. *Planet. Space Sci.*, 41, 551–561.
- Dubois, J. (1947). Sur l'albedo de la Terre. *Bulletin Astronomique*, 13, 193–196.
- Ehrenreich, D., Bonfils, X., Lovis, C., Delfosse, X., Forveille, T., Mayor, M., Neves, V., Santos, N. C., Udry, S., & Ségransan, D. (2014). Near-infrared transmission spectrum of the warm-Uranus GJ 3470b with the Wide Field Camera-3 on the Hubble Space Telescope. *Astron. Astrophys.*, 570, A89.
- Emmanuel, S., & Ague, J. J. (2007). Implications of present-day abiogenic methane fluxes for the early Archean atmosphere. *Geophys. Res. Lett.*, 34, L15810.
- Erwin, D. H. (1994). The Permo-Triassic extinction. *Nature*, 367, 231–236.
- Evans, D. A., Beukes, N. J., & Kirschvink, J. L. (1997). Low-latitude glaciation in the Palaeoproterozoic era. *Nature*, 386, 262–266.
- Farquhar, J., Bao, H., Thieme, M. (2000). Atmospheric influence of Earth's earliest sulfur cycle. *Science*, 289, 756–758.
- Feng, Y. K., Robinson, T. D., Fortney, J. J., Lupu, R. E., Marley, M. S., Lewis, N. K., Macintosh, B., & Line, M. R. (2018). Characterizing Earth Analogs in Reflected Light: Atmospheric Retrieval Studies for Future Space Telescopes. *Astron. J.*, 155, 200.
- Feulner, G. (2017). Formation of most of our coal brought Earth close to global glaciation. *Proceedings of the National Academy of Science*, 114, 11333–11337.
- Feulner, G. (2012). The faint young Sun problem. *Reviews of Geophysics*, 50.
- Fiorella, R. P., & Sheldon, N. D. (2017). Equable end Mesoproterozoic climate in the absence of high CO₂. *Geology*, 45, 231–234.
- Ford, E. B., Seager, S., & Turner, E. L. (2001). Characterization of extrasolar terrestrial planets from diurnal photometric variability. *Nature*, 412, 885–887.
- Foreman-Mackey, D., Hogg, D. W., & Morton, T. D. (2014). Exoplanet Population Inference and the Abundance of Earth Analogs from Noisy, Incomplete Catalogs. *Astrophys. J.*, 795, 64.
- Fox, G. E., Stackebrandt, E., Hespell, R. B., Gibson, J., Maniloff, J., Dyer, T. A., Wolfe, R. S., Balch, W. E., Tanner, R. S., Magrum, L. J., Zablen, L. B., Blakemore, R., Gupta, R., Bonen, L., Lewis, B. J., Stahl, D. A., Luehrsen, K. R., Chen, K. N., & Woese, C. R. (1980). The Phylogeny of Prokaryotes. *Science*, 209, 457–463.
- Fraine, J., Deming, D., Benneke, B., Knutson, H., Jordán, A., Espinoza, N., Madhusudhan, N., Wilkins, A., & Todorov, K. (2014). Water vapour absorption in the clear atmosphere of a Neptune-sized exoplanet. *Nature*, 513, 526–529.
- Freing, A., Wallace, D. W. R., Bange, H. W. (2012). Global oceanic production of nitrous oxide. *Philosophical Transactions of the Royal Society B*, 367, 1245–1255.
- Fujii, Y., & Kawahara, H. (2012). Mapping Earth Analogs from Photometric Variability: Spin-Orbit Tomography for Planets in Inclined Orbits. *Astrophys. J.*, 755, 101.

- Fujii, Y., Kawahara, H., Suto, Y., Fukuda, S., Nakajima, T., Livengood, T. A., & Turner, E. L. (2011). Colors of a Second Earth. II. Effects of Clouds on Photometric Characterization of Earth-like Exoplanets. *Astrophys. J.*, 738, 184.
- Fujii, Y., Kawahara, H., Suto, Y., Taruya, A., Fukuda, S., Nakajima, T., & Turner, E. L. (2010). Colors of a Second Earth: Estimating the Fractional Areas of Ocean, Land, and Vegetation of Earth-like Exoplanets. *Astrophys. J.*, 715, 866–880.
- Fujii, Y., Lustig-Yaeger, J., & Cowan, N. B. (2017). Rotational Spectral Unmixing of Exoplanets: Degeneracies between Surface Colors and Geography. *Astron. J.*, 154, 189.
- Fujii, Y., Turner, E. L., & Suto, Y. (2013). Variability of Water and Oxygen Absorption Bands in the Disk-integrated Spectra of Earth. *Astrophys. J.*, 765, 76.
- Gaillard, F., Scaillet, B., & Arndt, N. T. (2011). Atmospheric oxygenation caused by a change in volcanic degassing pressure. *Nature*, 478, 229–232.
- Galbraith, E. D., & Eggleston, S. (2017). A lower limit to atmospheric CO₂ concentrations over the past 800,000 years. *Nature Geoscience*, 10, 295–298.
- Galilei, G. (1632). *Dialogue Concerning the Two Chief Worlds Systems*. Giovanni Battista Landini.
- García Muñoz, A., Zapatero Osorio, M. R., Barrena, R., Montañés-Rodríguez, P., Martín, E. L., & Pallé, E. (2012). Glancing Views of the Earth: From a Lunar Eclipse to an Exoplanetary Transit. *Astrophys. J.*, 755, 103.
- Gardner, J. P., Mather, J. C., Clampin, M., Doyon, R., Greenhouse, M. A., Hammel, H. B., Hutchings, J. B., Jakobsen, P., Lilly, S. J., Long, K. S., Lunine, J. I., McCaughrean, M. J., Mountain, M., Nella, J., Rieke, G. H., Rieke, M. J., Rix, H.-W., Smith, E. P., Sonneborn, G., Stiavelli, M., Stockman, H. S., Windhorst, R. A., & Wright, G. S. (2006). The James Webb Space Telescope. *Space Sci. Rev.*, 123, 485–606.
- Gaucher, E. A., Govindarajan, S., & Ganesh, O. K. (2008). Palaeotemperature trend for Precambrian life inferred from resurrected proteins. *Nature*, 451, 704–707.
- Gaudi, B. S., Seager, S., Mennesson, B., Kiessling, A., Warfield, K. R., Habitable Exoplanet Observatory Science, & Technology Definition Team (2018). The Habitable Exoplanet Observatory. *Nature Astronomy*, 2, 600–604.
- Geboy, N. J., Kaufman, A. J., Walker, R. J., Misi, A., de Oliveira, T. F., Miller, K. E., Azmy, K., Kendall, B., & Poulton, S. W. (2013). Re-Os age constraints and new observations of Proterozoic glacial deposits in the Vazante Group, Brazil. *Precambrian Research*, 238, 199–213.
- Gehrels, T. (1976). The results of the imaging photopolarimeter on Pioneers 10 and 11. In T. Gehrels (Ed.) *Jupiter*, (pp. 531–563). University of Arizona Press.
- Gillon, M., Jehin, E., Lederer, S. M., Delrez, L., de Wit, J., Burdanov, A., Van Grootel, V., Burgasser, A. J., Triaud, A. H. M. J., Opitom, C., Demory, B.-O., Sahu, D. K., Bardalez Gagliuffi, D., Magain, P., & Queloz, D. (2016). Temperate Earth-sized planets transiting a nearby ultra-cool dwarf star. *Nature*, 533, 221–224.
- Gillon, M., Triaud, A. H. M. J., Demory, B.-O., Jehin, E., Agol, E., Deck, K. M., Lederer, S. M., de Wit, J., Burdanov, A., Ingalls, J. G., Bolmont, E., Leconte, J., Raymond, S. N., Selsis, F., Turbet, M., Barkaoui, K., Burgasser, A., Burleigh, M. R., Carey, S. J., Chaushev, A., Copperwheat, C. M., Delrez, L., Fernandes, C. S., Holdsworth, D. L., Kotze, E. J., Van Grootel, V., Almléaky, Y., Benkhaldoun, Z., Magain, P., & Queloz, D. (2017). Seven temperate terrestrial planets around the nearby ultracool dwarf star TRAPPIST-1. *Nature*, 542, 456–460.
- Glasspool, I. J., & Scott, A. C. (2010). Phanerozoic concentrations of atmospheric oxygen reconstructed from sedimentary charcoal. *Nature Geoscience*, 3, 627–630.
- Goldblatt, C., Claire, M. W., Lenton, T. M., Matthews, A. J., Watson, A. J., & Zahnle, K. J. (2009). Nitrogen-enhanced greenhouse warming on early Earth. *Nature Geoscience*, 2, 891–896.
- Goldblatt, C., Lenton, T. M., & Watson, A. J. (2006). Bistability of atmospheric oxygen and the Great Oxidation. *Nature*, 443, 683–686.
- Goldblatt, C., & Zahnle, K. J. (2011). Clouds and the Faint Young Sun Paradox. *Climate of the Past*, 7, 203–220.
- Gómez-Leal, I., Pallé, E., & Selsis, F. (2012). Photometric Variability of the Disk-integrated Thermal Emission of the Earth. *Astrophys. J.*, 752, 28.
- González-Merino, B., Pallé, E., Motalebi, F., Montañés-Rodríguez, P., & Kissler-Patig, M. (2013). Earthshine Observations at High Spectral Resolution: Exploring and Detecting Metal Lines in the Earth's Upper Atmosphere. *Mon. Not. R. Astron. Soc.*, 435, 2574–2580.
- Goode, P. R., Qiu, J., Yurchyshyn, V., Hickey, J., Chu, M., Kolbe, E., Brown, C. T., & Koonin, S. E. (2001). Earthshine Observations of the Earth's Reflectance. *Geophys. Res. Lett.*, 28, 1671–1674.
- Gough, D. O. (1981). Solar interior structure and luminosity variations. *Sol. Phys.*, 74, 21–34.

- Greber, N. D., Dauphas, N., Bekker, A., Ptáček, M. P., Bindeman, I. N., & Hofmann, A. (2017). Titanium isotopic evidence for felsic crust and plate tectonics 3.5 billion years ago. *Science*, 357, 1271–1274.
- Greene, T. P., Line, M. R., Montero, C., Fortney, J. J., Lustig-Yaeger, J., & Luther, K. (2016). Characterizing transiting exoplanet atmospheres with jwst. *Astrophys. J.*, 817(1), 17.
- Grillmair, C. J., Burrows, A., Charbonneau, D., Armus, L., Stauffer, J., Meadows, V., van Cleve, J., von Braun, K., & Levine, D. (2008). Strong water absorption in the day-side emission spectrum of the planet HD189733b. *Nature*, 456, 767–769.
- Gumsley, A. P., Chamberlain, K. R., Bleeker, W., Söderlund, U., de Kock, M. O., Larsson, E. R., & Bekker, A. (2017). Timing and tempo of the Great Oxidation Event. *Proceedings of the National Academy of Science*, 114, 1811–1816.
- Gurnett, D. A., Kurth, W. S., Shaw, R. R., Roux, A., Gendrin, R., Kennel, C. F., Scarf, F. L., & Shawhan, S. D. (1992). The Galileo Plasma Wave Investigation. *Space Sci. Rev.*, 60, 341–355.
- Guyon, O., Pluzhnik, E. A., Kuchner, M. J., Collins, B., & Ridgway, S. T. (2006). Theoretical Limits on Extrasolar Terrestrial Planet Detection with Coronagraphs. *Astrophys. J. Suppl.*, 167, 81–99.
- Halevy, I., & Bachan, A. (2017). The geologic history of seawater pH. *Science*, 355, 1069–1071.
- Hanel, R., Conrath, B., Kunde, V., Lowman, P., Maguire, W., Pearl, J., Pirraglia, J., Gautier, D., Gierasch, P., & Kumar, S. (1977). The Voyager infrared spectroscopy and radiometry investigation. *Space Sci. Rev.*, 21, 129–157.
- Hansen, C. J., Schwartz, J. C., & Cowan, N. B. (2014). Features in the broad-band eclipse spectra of exoplanets: signal or noise? *Mon. Not. R. Astron. Soc.*, 444, 3632–3640.
- Haqq-Misra, J., Kasting, J. F., & Lee, S. (2011). Availability of O₂ and H₂O₂ on Pre-Photosynthetic Earth. *Astrobiology*, 11, 293–302.
- Haqq-Misra, J., Kopparapu, R. K., Batalha, N. E., Harman, C. E., & Kasting, J. F. (2016). Limit Cycles Can Reduce the Width of the Habitable Zone. *Astrophys. J.*, 827, 120.
- Haqq-Misra, J. D., Domagal-Goldman, S. D., Kasting, P. J., & Kasting, J. F. (2008). A Revised, Hazy Methane Greenhouse for the Archean Earth. *Astrobiology*, 8, 1127–1137.
- Harada, M., Tajika, E., & Sekine, Y. (2015). Transition to an oxygen-rich atmosphere with an extensive overshoot triggered by the Paleoproterozoic snowball Earth. *Earth and Planetary Science Letters*, 419, 178–186.
- Hardisty, D. S., Lu, Z., Bekker, A., Diamond, C. W., Gill, B. C., Jiang, G., Kah, L. C., Knoll, A. H., Loyd, S. J., Osburn, M. R., Planavsky, N. J., Wang, C., Zhou, X., & Lyons, T. W. (2017). Perspectives on Proterozoic surface ocean redox from iodine contents in ancient and recent carbonate. *Earth and Planetary Science Letters*, 463, 159–170.
- Hearty, T., Song, I., Kim, S., & Tinetti, G. (2009). Mid-Infrared Properties of Disk Averaged Observations of Earth with AIRS. *Astrophys. J.*, 693, 1763–1774.
- Hedges, S. B. (2016). The origin and evolution of model organisms. *Nature Reviews Genetics*, 3, 838–849.
- Hedges, C., & Madhusudhan, N. (2016). Effect of pressure broadening on molecular absorption cross sections in exoplanetary atmospheres. *Mon. Not. R. Astron. Soc.*, 458, 1427–1449.
- Herrmann, A. D., Patzkowsky, M. E., & Pollard, D. (2004). The impact of paleogeography, pCO₂, poleward ocean heat transport and sea level change on global cooling during the Late Ordovician. *Palaeogeography, Palaeoclimatology, Palaeoecology*, 206, 59–74.
- Hessler, A. M., Lowe, D. R., Jones, R. L., & Bird, D. K. (2004). A lower limit for atmospheric carbon dioxide levels 3.2 billion years ago. *Nature*, 428, 736–738.
- Hirsch, A. I., Michalak, A. M., Bruhwiler, L. M., Peters, W., Dlugokencky, E. J., Tans, P. P. (2006). Inverse modeling estimates of the global nitrous oxide surface flux from 1998–2001. *Global Biogeochemical Cycles*, 20.
- Hoffman, P. F., Abbot, D. S., Ashkenazy, Y., Benn, D. I., Brocks, J. J., Cohen, P. A., Cox, G. M., Creveling, J. R., Donnadiou, Y., Erwin, D. H., Fairchild, I. J., Ferreira, D., Goodman, J. C., Halverson, G. P., Jansen, M. F., Le Hir, G., Love, G. D., Macdonald, F. A., Maloof, A. C., Partin, C. A., Ramstein, G., Rose, B. E. J., Rose, C. V., Sadler, P. M., Tziperman, E., Voigt, A., & Warren, S. G. (2017). Snowball Earth climate dynamics and Cryogenian geology-geobiology. *Science Advances*, 3, e1600983.
- Hoffman, P. F., Kaufman, A. J., Halverson, G. P., & Schrag, D. P. (1998). A Neoproterozoic Snowball Earth. *Science*, 281, 1342.
- Hoffman, P. F., & Schrag, D. P. (2002). The snowball Earth hypothesis: testing the limits of global change. *Terra Nova*, 14, 129–155.
- Holland, H. (1984). *The Chemical Evolution of the Atmosphere and Oceans*. Princeton University Press.

- Holland, H. D. (2002). Volcanic gases, black smokers, and the great oxidation event. *Geochim. Cosmochim. Acta*, 66, 3811–3826.
- Holland, H. D. (2009). Why the atmosphere became oxygenated: A proposal. *Geochim. Cosmochim. Acta*, 73, 5241–5255.
- Hönisch, B., Ridgwell, A., Schmidt, D. N., Thomas, E., Gibbs, S. J., Sluijs, A., Zeebe, R., Kump, L., Martindale, R. C., Greene, S. E., Kiessling, W., Ries, J., Zachos, J. C., Royer, D. L., Barker, S., Marchitto, T. M., Moyer, R., Pelejero, C., Ziveri, P., Foster, G. L., & Williams, B. (2012). The Geological Record of Ocean Acidification. *Science*, 335, 1058.
- Hord, C. W., McClintock, W. E., Stewart, A. I. F., Barth, C. A., Esposito, L. W., Thomas, G. E., Sandel, B. R., Hunten, D. M., Broadfoot, A. L., & Shemansky, D. E. (1992). Galileo Ultraviolet Spectrometer Experiment. *Space Sci. Rev.*, 60, 503–530.
- Hren, M. T., Tice, M. M., & Chamberlain, C. P. (2009). Oxygen and hydrogen isotope evidence for a temperate climate 3.42 billion years ago. *Nature*, 462, 205–208.
- Hu, R. (2014). Ammonia, Water Clouds and Methane Abundances of Giant Exoplanets and Opportunities for Super-Earth Exoplanets. *ArXiv e-prints*, 1412.7582.
- Hubbard, W., Fortney, J., Lunine, J., Burrows, A., Sudarsky, D., & Pinto, P. (2001). Theory of extrasolar giant planet transits. *The Astrophysical Journal*, 560(1), 413.
- Hunten, D. M. (1973). The Escape of Light Gases from Planetary Atmospheres. *Journal of Atmospheric Sciences*, 30, 1481–1494.
- Ingersoll, A. P., Muench, G., Neugebauer, G., & Orton, G. S. (1976). Results of the infrared radiometer experiment on Pioneers 10 and 11. In T. Gehrels (Ed.) *Jupiter*, (pp. 197–205). University of Arizona Press.
- Izon, G., Zerkle, A. L., Williford, K. H., Farquhar, J., Poulton, S. W., & Claire, M. W. (2017). Biological regulation of atmospheric chemistry en route to planetary oxygenation. *Proceedings of the National Academy of Science*, 114, E2571–E2579.
- Johnson, T. V., Yeates, C. M., & Young, R. (1992). Space Science Reviews Volume on Galileo Mission Overview. *Space Sci. Rev.*, 60, 3–21.
- Kah, L. C., & Riding, R. (2007). Mesoproterozoic carbon dioxide levels inferred from calcified cyanobacteria. *Geology*, 35, 799.
- Kaltenegger, L., Miguel, Y., & Rugheimer, S. (2012). Rocky exoplanet characterization and atmospheres. *International Journal of Astrobiology*, 11, 297–307.
- Kaltenegger, L., Selsis, F., Fridlund, M., Lammer, H., Beichman, C., Danchi, W., Eiroa, C., Henning, T., Herbst, T., Léger, A., Liseau, R., Lunine, J., Paresce, F., Penny, A., Quirrenbach, A., Röttgering, H., Schneider, J., Stam, D., Tinetti, G., & White, G. J. (2010). Deciphering Spectral Fingerprints of Habitable Exoplanets. *Astrobiology*, 10, 89–102.
- Kaltenegger, L., & Traub, W. (2009). Transits of earth-like planets. *The Astrophysical Journal*, 698, 519.
- Kaltenegger, L., Traub, W. A., & Jucks, K. W. (2007). Spectral Evolution of an Earth-like Planet. *Astrophys. J.*, 658, 598–616.
- Kanzaki, Y., & Murakami, T. (2015). Estimates of atmospheric CO₂ in the Neoproterozoic-Paleoproterozoic from paleosols. *Geochim. Cosmochim. Acta*, 159, 190–219.
- Karalidi, T., & Stam, D. M. (2012). Modeled flux and polarization signals of horizontally inhomogeneous exoplanets applied to Earth-like planets. *Astron. Astrophys.*, 546, A56.
- Karalidi, T., Stam, D. M., & Hovenier, J. W. (2011). Flux and polarisation spectra of water clouds on exoplanets. *Astron. Astrophys.*, 530, A69.
- Karalidi, T., Stam, D. M., & Hovenier, J. W. (2012). Looking for the rainbow on exoplanets covered by liquid and icy water clouds. *Astron. Astrophys.*, 548, A90.
- Karhu, J. A., & Holland, H. D. (1996). Carbon isotopes and the rise of atmospheric oxygen. *Geology*, 24, 867.
- Kasting, J. (2005). Methane and climate during the Precambrian era. *Precambrian Research*, 137, 119–129.
- Kasting, J. F. (1987). Theoretical constraints on oxygen and carbon dioxide concentrations in the Precambrian atmosphere. *Precambrian Research*, 34, 205–229.
- Kasting, J. F., & Donahue, T. M. (1980). The evolution of atmospheric ozone. *Journal of Geophysical Research*, 85, 3255–3263.
- Kasting, J. F., & Ackerman, T. P. (1986). Climatic consequences of very high carbon dioxide levels in the earth's early atmosphere. *Science*, 234, 1383–1385.
- Kasting, J. F., & Catling, D. (2003). Evolution of a Habitable Planet. *Annu. Rev. Astron. Astrophys.*, 41, 429–463.
- Kasting, J. F., & Walker, J. C. G. (1981). Limits on oxygen concentration in the prebiological atmosphere and the rate of abiotic fixation of nitrogen. *J. Geophys. Res.*, 86, 1147–1158.
- Kasting, J. F., Whitmire, D. P., & Reynolds, R. T. (1993). Habitable zones around main sequence stars. *Icarus*, 101, 108–128.

- Kaufman, A. J., & Xiao, S. (2003). High CO₂ levels in the Proterozoic atmosphere estimated from analyses of individual microfossils. *Nature*, 425, 279–282.
- Kavanagh, L., & Goldblatt, C. (2015). Using raindrops to constrain past atmospheric density. *Earth and Planetary Science Letters*, 413, 51–58.
- Kawahara, H. (2016). Frequency Modulation of Directly Imaged Exoplanets: Geometric Effect as a Probe of Planetary Obliquity. *Astrophys. J.*, 822, 112.
- Kawahara, H., & Fujii, Y. (2010). Global Mapping of Earth-like Exoplanets From Scattered Light Curves. *Astrophys. J.*, 720, 1333–1350.
- Kharecha, P., Kasting, J. K., & Siefert, J. (2005). A coupled atmosphere-ecosystem model of the early Archean Earth. *Geobiology*, 3, 53–76.
- Kliore, A. J., & Woiceshyn, P. M. (1976). Structure of the atmosphere of Jupiter from Pioneer 10 and 11 radio occultation measurements. In T. Gehrels (Ed.) *Jupiter*, (pp. 216–237). University of Arizona Press.
- Knauth, L. P., & Epstein, S. (1976). Hydrogen and oxygen isotope ratios in nodular and bedded cherts. *Geochim. Cosmochim. Acta*, 40, 1095–1108.
- Knutson, H. A., Benneke, B., Deming, D., & Homeier, D. (2014a). A featureless transmission spectrum for the Neptune-mass exoplanet GJ436b. *Nature*, 505, 66–68.
- Knutson, H. A., Dragomir, D., Kreidberg, L., Kempton, E. M.-R., McCullough, P. R., Fortney, J. J., Bean, J. L., Gillon, M., Homeier, D., & Howard, A. W. (2014b). Hubble Space Telescope Near-IR Transmission Spectroscopy of the Super-Earth HD 97658b. *Astrophys. J.*, 794, 155.
- Kohlhase, C. E., & Penzo, P. A. (1977). Voyager Mission Description. *Space Sci. Rev.*, 21, 77–101.
- Konhauser, K. O., Pecoits, E., Lalonde, S. V., Papineau, D., Nisbet, E. G., Barley, M. E., Arndt, N. T., Zahnle, K., & Kamber, B. S. (2009). Oceanic nickel depletion and a methanogen famine before the Great Oxidation Event. *Nature*, 458, 750–753.
- Kopp, R. E., Kirschvink, J. L., Hilburn, I. A., & Nash, C. Z. (2005). The Paleoproterozoic snowball Earth: A climate disaster triggered by the evolution of oxygenic photosynthesis. *Proceedings of the National Academy of Science*, 102, 11131–11136.
- Kopparapu, R. k., Hebrard, E., Belikov, R., Batalha, N. M., Mulders, G. D., Stark, C., Teal, D., Domagal-Goldman, S., & Mandell, A. (2018). Exoplanet Classification and Yield Estimates for Direct Imaging Missions. *Astrophys. J.*, 856, 122.
- Korenaga, J. (2013). Initiation and Evolution of Plate Tectonics on Earth: Theories and Observations. *Annual Review of Earth and Planetary Sciences*, 41, 117–151.
- Kreidberg, L. (2018). Exoplanet Atmosphere Measurements from Transmission Spectroscopy and Other Planet Star Combined Light Observations. In H. J. Deeg, & J. A. Belmonte (Eds.) *Handbook of Exoplanets*. Springer.
- Kreidberg, L., Bean, J. L., Désert, J.-M., Benneke, B., Deming, D., Stevenson, K. B., Seager, S., Berta-Thompson, Z., Seifahrt, A., & Homeier, D. (2014). Clouds in the atmosphere of the super-earth exoplanet gJ 1214b. *Nature*, 505(7481), 69–72.
- Krissansen-Totton, J., Arney, G. N., & Catling, D. C. (2018). Constraining the climate and ocean pH of the early Earth with a geological carbon cycle model. *Proceedings of the National Academy of Sciences*, 115, 4105–4110.
- Krissansen-Totton, J., Bergsman, D. S., & Catling, D. C. (2016a). On Detecting Biospheres from Chemical Thermodynamic Disequilibrium in Planetary Atmospheres. *Astrobiology*, 16, 39–67.
- Krissansen-Totton, J., Schwieterman, E. W., Charnay, B., Arney, G., Robinson, T. D., Meadows, V., & Catling, D. C. (2016b). Is the Pale Blue Dot Unique? Optimized Photometric Bands for Identifying Earth-like Exoplanets. *Astrophys. J.*, 817, 31.
- Kuhn, W. R., & Atreya, S. K. (1979). Ammonia photolysis and the greenhouse effect in the primordial atmosphere of the earth. *Icarus*, 37, 207–213.
- Kump, L. R., & Arthur, M. A. (1999). Interpreting carbon-isotope excursions: carbonates and organic matter. *Chemical Geology*, 161, 181–198.
- Kump, L. R., & Barley, M. E. (2007). Increased subaerial volcanism and the rise of atmospheric oxygen 2.5 billion years ago. *Nature*, 448, 1033–1036.
- Kump, L. R., Kasting, J. F., & Barley, M. E. (2001). Rise of atmospheric oxygen and the “upside-down” Archean mantle. *Geochemistry, Geophysics, Geosystems*, 2, 1025–10.
- Kurzweil, F., Claire, M., Thomazo, C., Peters, M., Hannington, M., & Strauss, H. (2013). Atmospheric sulfur rearrangement 2.7 billion years ago: Evidence for oxygenic photosynthesis. *Earth and Planetary Science Letters*, 366, 17–26.
- Laakso, T. A., & Schrag, D. P. (2017). A theory of atmospheric oxygen. *Geobiology*, 415, 366–384.

- Le Hir, G., Godd  ris, Y., Donnadi  u, Y., & Ramstein, G. (2008a). A geochemical modelling study of the evolution of the chemical composition of seawater linked to a “snowball” glaciation. *Biogeosciences*, 5, 253–267.
- Le Hir, G., Ramstein, G., Donnadi  u, Y., & Godd  ris, Y. (2008b). Scenario for the evolution of atmospheric pCO₂ during a snowball Earth. *Geology*, 36, 47–50.
- Lenton, T. M., Crouch, M., Johnson, M., Pires, N., & Dolan, L. (2012). First plants cooled the Ordovician. *Nature Geoscience*, 5, 86–89.
- Lenton, T. M., Daines, S. J., & Mills, B. J. W. (2018). COPSE reloaded: An improved model of biogeochemical cycling over Phanerozoic time. *Earth Science Reviews*, 33, 1–28.
- Lepland, A., Joosu, L., Kirsim  e, K., Prave, A. R., Romashkin, A. E.,   rne, A. E., Martin, A. P., Fallick, A. E., Somelar, P.,   praus, K., M  nd, K., Roberts, N. M. W., van Zuilen, M. A., Wirth, R., & Schreiber, A. (2014). Potential influence of sulphur bacteria on Palaeoproterozoic phosphogenesis. *Nature Geoscience*, 7, 20–24.
- Levine, J. S., Hays, P. B., Walker, J. C. G. (1979). The evolution and variability of atmospheric ozone over geological time. *Icarus*, 39, 295–309.
- Li, Z.-X., & Lee, C.-T. (2004). The constancy of upper mantle fO₂ through time inferred from V/Sc ratios in basalts. *Earth and Planetary Science Letters*, 228, 483–493.
- Line, M. R., Knutson, H., Deming, D., Wilkins, A., & Desert, J.-M. (2013). A Near-infrared Transmission Spectrum for the Warm Saturn HAT-P-12b. *Astrophys. J.*, 778, 183.
- Line, M. R., Knutson, H., Wolf, A. S., & Yung, Y. L. (2014). A Systematic Retrieval Analysis of Secondary Eclipse Spectra. II. A Uniform Analysis of Nine Planets and their C to O Ratios. *Astrophys. J.*, 783, 70.
- Livengood, T. A., Deming, L. D., A’Hearn, M. F., Charbonneau, D., Hewagama, T., Lisse, C. M., McFadden, L. A., Meadows, V. S., Robinson, T. D., Seager, S., & Wellnitz, D. D. (2011). Properties of an Earth-Like Planet Orbiting a Sun-Like Star: Earth Observed by the EPOXI Mission. *Astrobiology*, 11, 907–930.
- Luo, G., Ono, S., Beukes, N. J., Wang, D. T., Xie, S., & Summons, R. (2016). The loss of mass-independent fractionation in sulfur due to a Paleoproterozoic collapse of atmospheric methane. *Science Advances*, 2.
- Lupu, R. E., Marley, M. S., Lewis, N., Line, M., Traub, W. A., & Zahnle, K. (2016). Developing Atmospheric Retrieval Methods for Direct Imaging Spectroscopy of Gas Giants in Reflected Light. I. Methane Abundances and Basic Cloud Properties. *Astron. J.*, 152, 217.
- Lustig-Yaeger, J., Meadows, V. S., Tovar Mendoza, G., Schwieterman, E. W., Fujii, Y., Luger, R., & Robinson, T. D. (2018). Detecting Ocean Glint on Exoplanets Using Multiphase Mapping. *Astron. J.*, 156, 301.
- Lyons, T. W., Reinhard, C. T., & Planavsky, N. J. (2014). The rise of oxygen in Earth’s early ocean and atmosphere. *Nature*, 506, 307–315.
- Macdonald, E. J. R., & Cowan, N. B. (2019). An empirical infrared transit spectrum of Earth: opacity windows and biosignatures. *Mon. Not. R. Astron. Soc.*, 489(1), 196–204.
- Macintosh, B., Graham, J. R., Barman, T., De Rosa, R. J., Konopacky, Q., Marley, M. S., Marois, C., Nielsen, E. L., Pueyo, L., Rajan, A., Rameau, J., Saumon, D., Wang, J. J., Patience, J., Ammons, M., Arriaga, P., Artigau, E., Beckwith, S., Brewster, J., Bruzzone, S., Bulger, J., Burningham, B., Burrows, A. S., Chen, C., Chiang, E., Chilcote, J. K., Dawson, R. I., Dong, R., Doyon, R., Draper, Z. H., Duch  ne, G., Esposito, T. M., Fabrycky, D., Fitzgerald, M. P., Follette, K. B., Fortney, J. J., Gerard, B., Goodsell, S., Greenbaum, A. Z., Hibon, P., Hinkley, S., Cotten, T. H., Hung, L.-W., Ingraham, P., Johnson-Groh, M., Kalas, P., Lafreniere, D., Larkin, J. E., Lee, J., Line, M., Long, D., Maire, J., Marchis, F., Matthews, B. C., Max, C. E., Metchev, S., Millar-Blanchaer, M. A., Mittal, T., Morley, C. V., Morzinski, K. M., Murray-Clay, R., Oppenheimer, R., Palmer, D. W., Patel, R., Perrin, M. D., Poyneer, L. A., Rafikov, R. R., Rantakyr  , F. T., Rice, E. L., Rojo, P., Rudy, A. R., Ruffio, J.-B., Ruiz, M. T., Sadakuni, N., Saddlemyer, L., Salama, M., Savransky, D., Schneider, A. C., Sivaramakrishnan, A., Song, I., Soummer, R., Thomas, S., Vasisht, G., Wallace, J. K., Ward-Duong, K., Wiktorowicz, S. J., Wolff, S. G., & Zuckerman, B. (2015). Discovery and spectroscopy of the young jovian planet 51 Eri b with the Gemini Planet Imager. *Science*, 350, 64–67.
- Madhusudhan, N., & Seager, S. (2009). A Temperature and Abundance Retrieval Method for Exoplanet Atmospheres. *Astrophys. J.*, 707, 24–39.
- Magnabosco, C., Moore, K. R., Wolfe, J. M., & Fournier, G. P. (2018). Dating phototrophic microbial lineages with reticulate gene histories. *Geobiology*, 16, 179–189.
- Majeau, C., Agol, E., & Cowan, N. B. (2012). A Two-dimensional Infrared Map of the Extrasolar Planet HD 189733b. *Astrophys. J. Lett.*, 747, L20.
- Manalo-Smith, N., Smith, G. L., Tiwari, S. N., & Staylor, W. F. (1998). Analytic forms of bidirectional reflectance functions for application to Earth radiation budget studies. *J. Geophys. Res.*, 103, 19733–19752.
- Marley, M., Lupu, R., Lewis, N., Line, M., Morley, C., & Fortney, J. (2014). A Quick Study of the Characterization of Radial Velocity Giant Planets in Reflected

- Light by Forward and Inverse Modeling. *ArXiv e-prints*, 1412.8440.
- Marois, C., Macintosh, B., Barman, T., Zuckerman, B., Song, I., Patience, J., Lafrenière, D., & Doyon, R. (2008). Direct Imaging of Multiple Planets Orbiting the Star HR 8799. *Science*, 322, 1348.
- Martín-Torres, F. J., Kutepov, A., Dudhia, A., Gusev, O., & Feofilov, A. G. (2003). Accurate and Fast Computation of the Radiative Transfer Absorption Rates for the Infrared Bands in the Atmosphere of Titan. In *EGS/AGU/EUG Joint Assembly*, (p. 7735).
- Marty, B., Zimmermann, L., Pujol, M., Burgess, R., & Philippot, P. (2013). Nitrogen Isotopic Composition and Density of the Archean Atmosphere. *Science*, 342, 101–104.
- Matson, P. A., & Vitousek, P. M. (1990). Ecosystem approach to a global nitrous oxide budget. *BioScience*, 40, 667–672.
- Mawet, D., Pueyo, L., Lawson, P., Mugnier, L., Traub, W., Boccaletti, A., Trauger, J. T., Gladysz, S., Serabyn, E., Milli, J., Belikov, R., Kasper, M., Baudoz, P., Macintosh, B., Marois, C., Oppenheimer, B., Barrett, H., Beuzit, J.-L., Devaney, N., Girard, J., Guyon, O., Krist, J., Mennesson, B., Mouillet, D., Murakami, N., Poyneer, L., Savransky, D., Vérinaud, C., & Wallace, J. K. (2012). Review of Small-Angle Coronagraphic Techniques in the Wake of Ground-Based Second-Generation Adaptive Optics Systems. In *Space Telescopes and Instrumentation 2012: Optical, Infrared, and Millimeter Wave*, vol. 8442 of *Proc. SPIE*, (p. 844204).
- Mayor, M., & Queloz, D. (1995). A Jupiter-mass companion to a solar-type star. *Nature*, 378, 355–359.
- McCullough, P. R. (2006). Models of Polarized Light from Oceans and Atmospheres of Earth-like Extrasolar Planets. *ArXiv Astrophysics e-prints*, 0610518.
- Meadows, V. S. (2008). Planetary Environmental Signatures for Habitability and Life. In J. W. Mason (Ed.) *Exoplanets*, (p. 259). Springer.
- Meadows, V. S. (2011). Reflections on O₂ as a biosignature in exoplanetary atmospheres. *Astrobiology*, 17, 1022–1052.
- Melezhik, V. A., Huhma, H., Condon, D. J., Fallick, A. E., & Whitehouse, M. J. (2007). Temporal constraints on the Paleoproterozoic Lomagundi-Jatuli carbon isotopic event. *Geology*, 35, 655.
- Mennesson, B., Gaudi, S., Seager, S., Cahoy, K., Domagal-Goldman, S., Feinberg, L., Guyon, O., Kasdin, J., Marois, C., Mawet, D., Tamura, M., Mouillet, D., Prusti, T., Quirrenbach, A., Robinson, T., Rogers, L., Scowen, P., Somerville, R., Stapelfeldt, K., Stern, D., Still, M., Turnbull, M., Booth, J., Kiessling, A., Kuan, G., & Warfield, K. (2016). The Habitable Exoplanet (HabEx) Imaging Mission: preliminary science drivers and technical requirements. In *Space Telescopes and Instrumentation 2016: Optical, Infrared, and Millimeter Wave*, vol. 9904 of *Proc. SPIE*, (p. 99040L).
- Miles-Páez, P. A., Pallé, E., & Zapatero Osorio, M. R. (2014). Simultaneous Optical and Near-Infrared Linear Spectropolarimetry of the Earthshine. *Astron. Astrophys.*, 562, L5.
- Mills, B., Watson, A. J., Goldblatt, C., Boyle, R., & Lenton, T. M. (2011). Timing of Neoproterozoic glaciations linked to transport-limited global weathering. *Nature Geoscience*, 4, 861–864.
- Misra, A., Meadows, V., Claire, M., & Crisp, D. (2014a). Using Dimers to Measure Biosignatures and Atmospheric Pressure for Terrestrial Exoplanets. *Astrobiology*, 14, 67–86.
- Misra, A., Meadows, V., & Crisp, D. (2014b). The Effects of Refraction on Transit Transmission Spectroscopy: Application to Earth-like Exoplanets. *Astrophys. J.*, 792, 61.
- Mojzsis, S. J., Harrison, T. M., & Pidgeon, R. T. (2001). Oxygen-isotope evidence from ancient zircons for liquid water at the Earth’s surface 4,300Myr ago. *Nature*, 409, 178–181.
- Montañés-Rodríguez, P., Pallé, E., Goode, P. R., & Martín-Torres, F. J. (2006). Vegetation Signature in the Observed Globally Integrated Spectrum of Earth Considering Simultaneous Cloud Data: Applications for Extrasolar Planets. *Astrophys. J.*, 651, 544–552.
- Montañez, I. P., & Poulsen, C. J. (2013). The Late Paleozoic Ice Age: An Evolving Paradigm. *Annual Review of Earth and Planetary Sciences*, 41, 629–656.
- Nayak, M., Lupu, R., Marley, M. S., Fortney, J. J., Robinson, T., & Lewis, N. (2017). Atmospheric Retrieval for Direct Imaging Spectroscopy of Gas Giants in Reflected Light. II. Orbital Phase and Planetary Radius. *PASP*, 129(3), 034401.
- Nicklas, R. W., Puchtel, I. S., & Ash, R. D. (2018). Redox state of the Archean mantle: Evidence from V partitioning in 3.5–2.4 Ga komatiites. *Geochim. Cosmochim. Acta*, 222, 447–466.
- Nishizawa, M., Sano, Y., Ueno, Y., & Maruyama, S. (2007). Speciation and isotope ratios of nitrogen in fluid inclusions from seafloor hydrothermal deposits at ~3.5 Ga. *Earth and Planetary Science Letters*, 254, 332–344.
- Noecker, M. C., Zhao, F., Demers, R., Trauger, J., Guyon, O., & Jeremy Kasdin, N. (2016). Coronagraph instrument for WFIRST-AFTA. *Journal of Astronomical Telescopes, Instruments, and Systems*, 2(1), 011001.

- Oakley, P. H. H., & Cash, W. (2009). Construction of an Earth Model: Analysis of Exoplanet Light Curves and Mapping the Next Earth with the New Worlds Observer. *Astrophys. J.*, 700, 1428–1439.
- Olson, S. L., Reinhard, C. T., & Lyons, T. W. (2016). Limited role for methane in the mid-Proterozoic greenhouse. *Proceedings of the National Academy of Science*, 113, 11447–11452.
- Olson, S. L., Schwieterman, E. W., Reinhard, C. T., Ridgwell, A., Kane, S. R., Meadows, V. S., & Lyons, T. W. (2018). Atmospheric Seasonality as an Exoplanet Biosignature. *Astrophys. J. Lett.*, 858, L14.
- Olson, S. L., Schwieterman, E. W., Reinhard, C. T., & Lyons, T. W. (2018). Earth: Atmospheric evolution of a habitable planet. In H. J. Deeg, & J. A. Belmonte (Eds.) *Handbook of Exoplanets*. Springer.
- Ozaki, K., Tajika, E., Hong, P. K., Nakagawa, Y., & Reinhard, C. T. (2018). Effects of primitive photosynthesis on Earth's early climate system. *Nature Geoscience*, 11, 55–59.
- Pallé, E., Ford, E. B., Seager, S., Montañés-Rodríguez, P., & Vazquez, M. (2008). Identifying the Rotation Rate and the Presence of Dynamic Weather on Extrasolar Earth-like Planets from Photometric Observations. *Astrophys. J.*, 676, 1319–1329.
- Pallé, E., Goode, P. R., & Montañés-Rodríguez, P. (2009a). Interannual Variations in Earth's Reflectance 1999–2007. *Journal of Geophysical Research (Atmospheres)*, 114, D00D03.
- Pallé, E., Goode, P. R., Montañés-Rodríguez, P., & Koonin, S. E. (2004a). Changes in Earth's Reflectance over the Past Two Decades. *Science*, 304, 1299–1301.
- Pallé, E., Goode, P. R., Montañés-Rodríguez, P., Shumko, A., Gonzalez-Merino, B., Lombilla, C. M., Jimenez-Ibarra, F., Shumko, S., Sanroma, E., Hult, A., Miles-Paez, P., Murgas, F., Nowak, G., & Koonin, S. E. (2016). Earth's albedo variations 1998–2014 as measured from ground-based earthshine observations. *Geophys. Res. Lett.*, 43, 4531–4538.
- Pallé, E., Goode, P. R., Yurchyshyn, V., Qiu, J., Hickey, J., Montañés Rodríguez, P., Chu, M., Kolbe, E., Brown, C. T., & Koonin, S. E. (2003). Earthshine and the Earth's albedo: 2. Observations and simulations over 3 years. *Journal of Geophysical Research (Atmospheres)*, 108, 4710.
- Pallé, E., Montañés Rodríguez, P., Goode, P. R., Qiu, J., Yurchyshyn, V., Hickey, J., Chu, M.-C., Kolbe, E., Brown, C. T., & Koonin, S. E. (2004b). The Earthshine Project: Update on pPhotometric and Spectroscopic Measurements. *Advances in Space Research*, 34, 288–292.
- Pallé, E., Zapatero Osorio, M. R., Barrena, R., Montañés-Rodríguez, P., & Martín, E. L. (2009b). Earth's Transmission Spectrum from Lunar Eclipse Observations. *Nature*, 459, 814–816.
- Partin, C. A., Bekker, A., Planavsky, N. J., Scott, C. T., Gill, B. C., Li, C., Podkovyrov, V., Maslov, A., Konhauser, K. O., Lalonde, S. V., Love, G. D., Poulton, S. W., & Lyons, T. W. (2013). Large-scale fluctuations in Precambrian atmospheric and oceanic oxygen levels from the record of U in shales. *Earth and Planetary Science Letters*, 369, 284–293.
- Pavlov, A. A., Brown, L. L., & Kasting, J. F. (2001). UV shielding of NH₃ and O₂ by organic hazes in the Archean atmosphere. *J. Geophys. Res.*, 106, 23267–23288.
- Pavlov, A. A., & Kasting, J. F. (2002). Mass-Independent Fractionation of Sulfur Isotopes in Archean Sediments: Strong Evidence for an Anoxic Archean Atmosphere. *Astrobiology*, 2, 27–41.
- Pavlov, A. A., Kasting, J. F., Brown, L. L., Rages, K. A., & Freedman, R. (2000). Greenhouse warming by CH₄ in the atmosphere of early Earth. *J. Geophys. Res.*, 105, 11981–11990.
- Payne, J. L., Lehrmann, D. J., Wei, J., Orchard, M. J., Schrag, D. P., & Knoll, A. H. (2004). Large Perturbations of the Carbon Cycle During Recovery from the End-Permian Extinction. *Science*, 305, 506–509.
- Peterson, B. M., Fischer, D., & LUVOIR Science and Technology Definition Team (2017). The Large Ultraviolet/Optical/Infrared Surveyor (LUVOIR). In *American Astronomical Society Meeting Abstracts*, vol. 229 of *American Astronomical Society Meeting Abstracts*, (p. 405.04).
- Petigura, E. A., Marcy, G. W., & Howard, A. W. (2013). A Plateau in the Planet Population below Twice the Size of Earth. *Astrophys. J.*, 770, 69.
- Pierrehumbert, R. T., Abbot, D. S., Voigt, A., & Koll, D. (2011). Climate of the Neoproterozoic. *Annual Review of Earth and Planetary Sciences*, 39, 417–460.
- Planavsky, N., Bekker, A., Rouxel, O. J., Kamber, B., Hofmann, A., Knudsen, A., & Lyons, T. W. (2010). Rare Earth Element and yttrium compositions of Archean and Paleoproterozoic Fe formations revisited: New perspectives on the significance and mechanisms of deposition. *Geochim. Cosmochim. Acta*, 74, 6387–6405.
- Planavsky, N. J., Asael, D., Hofmann, A., Reinhard, C. T., Lalonde, S. V., Knudsen, A., Wang, X., Ossa Ossa, F., Pecoits, E., Smith, A. J. B., Beukes, N. J., Bekker, A., Johnson, T. M., Konhauser, K. O., Lyons, T. W., &

- Rouxel, O. J. (2014a). Evidence for oxygenic photosynthesis half a billion years before the Great Oxidation Event. *Nature Geoscience*, 7, 283–286.
- Planavsky, N. J., Bekker, A., Hofmann, A., Owens, J. D., & Lyons, T. W. (2012). Sulfur record of rising and falling marine oxygen and sulfate levels during the Lomagundi event. *Proceedings of the National Academy of Science*, 109, 18300–18305.
- Planavsky, N. J., Reinhard, C. T., Wang, X., Thomson, D., McGoldrick, P., Rainbird, R. H., Johnson, T., Fischer, W. W., & Lyons, T. W. (2014b). Low Mid-Proterozoic atmospheric oxygen levels and the delayed rise of animals. *Science*, 346, 635–638.
- Pont, F., Knutson, H., Gilliland, R., Moutou, C., & Charbonneau, D. (2008). Detection of atmospheric haze on an extrasolar planet: the 0.55–1.05 μm transmission spectrum of hd 189733b with the hubble space telescope. *Monthly Notices of the Royal Astronomical Society*, 385(1), 109–118.
- Prather, M. J., & Hsu, J. (2010). *Science*, 330, 952–954.
- Qiu, J., Goode, P., Pallé, E., Yurchyshyn, V., Hickey, J., Montanés-Rodríguez, P., Chu, M., Kolbe, E., Brown, C., & Koonin, S. (2003). Earthshine and the earth's albedo: 1. earthshine observations and measurements of the lunar phase function for accurate measurements of the earth's bond albedo. *J. Geophys. Res.*, 108(4709), 1999–2007.
- Rasmussen, B., Bekker, A., & Fletcher, I. R. (2013). Correlation of Paleoproterozoic glaciations based on U-Pb zircon ages for tuff beds in the Transvaal and Huronian Supergroups. *Earth and Planetary Science Letters*, 382, 173–180.
- Rasmussen, B., & Buick, R. (1999). Redox state of the Archean atmosphere: Evidence from detrital heavy minerals in ca. 3250–2750 Ma sandstones from the Pilbara Craton, Australia. *Geology*, 27, 115.
- Raymond, A., & Metz, C. (2004). Ice and Its Consequences: Glaciation in the Late Ordovician, Late Devonian, Pennsylvanian-Permian, and Cenozoic Compared. *Journal of Geology*, 112, 655–670.
- Reinhard, C. T., Olson, S. L., Schwieterman, E. W., & Lyons, T. W. (2017a). False Negatives for Remote Life Detection on Ocean-Bearing Planets: Lessons from the Early Earth. *Astrobiology*, 17, 287–297.
- Reinhard, C. T., Planavsky, N. J., Gill, B. C., Ozaki, K., Robbins, L. J., Lyons, T. W., Fischer, W. W., Wang, C., Cole, D. B., & Konhauser, K. O. (2017b). Evolution of the global phosphorus cycle. *Nature*, 541, 386–389.
- Reinhard, C. T., Planavsky, N. J., Robbins, L. J., Partin, C. A., Gill, B. C., Lalonde, S. V., Bekker, A., Konhauser, K. O., & Lyons, T. W. (2013). Proterozoic ocean redox and biogeochemical stasis. *Proceedings of the National Academy of Science*, 110, 5357–5362.
- Roberge, A., & Moustakas, L. A. (2018). The Large Ultraviolet/Optical/Infrared Surveyor. *Nature Astronomy*, 2, 605–607.
- Roberson, A. L., Roadt, J., Halevy, I., & Kasting, J. F. (2011). Greenhouse warming by nitrous oxide and methane in the Proterozoic Eon. *Geobiology*, 9, 313–320.
- Robert, F., & Chaussidon, M. (2006). A palaeotemperature curve for the Precambrian oceans based on silicon isotopes in cherts. *Nature*, 443, 969–972.
- Robinson, T. D. (2011). Modeling the Infrared Spectrum of the Earth-Moon System: Implications for the Detection and Characterization of Earthlike Extrasolar Planets and their Moonlike Companions. *Astrophys. J.*, 741, 51.
- Robinson, T. D. (2018). Characterizing Exoplanets for Habitability. In H. J. Deeg, & J. A. Belmonte (Eds.) *Handbook of Exoplanets*. Springer.
- Robinson, T. D., Ennico, K., Meadows, V. S., Sparks, W., Bussey, D. B. J., Schwieterman, E. W., & Breiner, J. (2014). Detection of Ocean Glint and Ozone Absorption Using LCROSS Earth Observations. *Astrophys. J.*, 787, 171.
- Robinson, T. D., Maltagliati, L., Marley, M. S., & Fortney, J. J. (2014). Titan solar occultation observations reveal transit spectra of a hazy world. *Proceedings of the National Academy of Sciences*, 111(25), 9042–9047.
- Robinson, T. D., Meadows, V. S., & Crisp, D. (2010). Detecting Oceans on Extrasolar Planets Using the Glint Effect. *Astrophys. J. Lett.*, 721, L67–L71.
- Robinson, T. D., Meadows, V. S., Crisp, D., Deming, D., A'Hearn, M. F., Charbonneau, D., Livengood, T. A., Seager, S., Barry, R. K., Hearty, T., Hewagama, T., Lisse, C. M., McFadden, L. A., & Wellnitz, D. D. (2011). Earth as an Extrasolar Planet: Earth Model Validation Using EPOXI Earth Observations. *Astrobiology*, 11, 393–408.
- Robinson, T. D., Stapelfeldt, K. R., & Marley, M. S. (2016). Characterizing Rocky and Gaseous Exoplanets with 2 m Class Space-based Coronagraphs. *PASP*, 128(2), 025003.
- Rodrigues, J. B., Pimentel, M. M., Buhn, B., Matteini, M., Dardenne, M. A., Alvarenga, C. J. S., & Armstrong, R. A. (2012). Provenance of the Vazante Group: New U-Pb, Sm-Nd, Lu-Hf isotopic data and implications for the tectonic evolution of the Neoproterozoic Brasília Belt. *Gondwana Research*, 21, 439–450.

- Rooney, A. D., Macdonald, F. A., Strauss, J. V., Dudás, F. Ö., Hallmann, C., & Selby, D. (2014). Re-Os geochronology and coupled Os-Sr isotope constraints on the Sturtian snowball Earth. *Proceedings of the National Academy of Science*, 111, 51–56.
- Rooney, A. D., Strauss, J. V., Brandon, A. D., & Macdonald, F. A. (2015). A Cryogenian chronology: Two long-lasting synchronous Neoproterozoic glaciations. *Geology*, 43, 459–462.
- Rosing, M. T., Rose, N. M., Bridgwater, D., & Thomsen, H. S. (1996). Earliest part of Earth's stratigraphic record: A reappraisal of the >3.7 Ga Isua (Greenland) supracrustal sequence. *Geology*, 24, 43.
- Royer, D. L. (2001). Stomatal density and stomatal index as indicators of paleoatmospheric CO₂ concentration. *Review of Palaeobotany and Palynology*, 114, 1–28.
- Royer, D. L. (2014). Atmospheric CO₂ and O₂ during the phanerozoic: Tools, patterns, and impacts. In Holland, H. D., & Turekian, K. K. (Eds.) *Treatise on Geochemistry*, (pp. 251–267). Elsevier.
- Royer, D. L., Berner, R. A., Montañez, I. P., Tabor, N. J., & Beerling, D. J. (2004). CO₂ as a primary driver of Phanerozoic climate. *GSA Today*, 14, 4–10.
- Royer, D. L., Donnadieu, Y., Park, J., Kowalczyk, J., & Godderis, Y. (2014). Error analysis of CO₂ and O₂ estimates from the long-term geochemical model GEOCARBSULF. *American Journal of Science*, 314, 1259–1283.
- Rugheimer, S., & Kaltenegger, L. (2018). Spectra of Earth-like Planets through Geological Evolution around FGKM Stars. *Astrophys. J.*, 854, 19.
- Rugheimer, S., Kaltenegger, L., Zsom, A., Segura, A., & Sasselov, D. (2013). Spectral Fingerprints of Earth-like Planets Around FGK Stars. *Astrobiology*, 13, 251–269.
- Rye, R., & Holland, H. D. (1998). Paleosols and the evolution of atmospheric oxygen; a critical review. *American Journal of Science*, 298, 621–672.
- Rye, R., Kuo, P. H., & Holland, H. D. (1995). Atmospheric carbon dioxide concentrations before 2.2 billion years ago. *Nature*, 378, 603–605.
- Sagan, C., & Mullen, G. (1972). Earth and Mars: Evolution of Atmospheres and Surface Temperatures. *Science*, 177, 52–56.
- Sagan, C., Thompson, W. R., Carlson, R., Gurnett, D., & Hord, C. (1993). A Search for Life on Earth from the Galileo Spacecraft. *Nature*, 365, 715–721.
- Sahoo, S. K., Planavsky, N. J., Kendall, B., Wang, X., Shi, X., Scott, C., Anbar, A. D., Lyons, T. W., & Jiang, G. (2012). Ocean oxygenation in the wake of the Marinoan glaciation. *Nature*, 489, 546–549.
- Schiffer, R. A., & Rossow, W. B. (1983). The International Satellite Cloud Climatology Project (ISCCP): The First Project of the World Climate Research Programme. *Bulletin of the American Meteorological Society*, 64, 779.
- Schrag, D. P., Berner, R. A., Hoffman, P. F., & Halverson, G. P. (2002). On the initiation of a snowball Earth. *Geochemistry Geophysics Geosystems*, 3.
- Schreier, F., Städt, S., Hedelt, P., & Godolt, M. (2018). Transmission spectroscopy with the ACE-FTS infrared spectral atlas of Earth: A model validation and feasibility study. *Molecular Astrophysics*, 11, 1–22.
- Schröder, S., Bekker, A., Beukes, N. J., Strauss, H., & van Niekerk, H. S. (2008). Rise in seawater sulphate concentration associated with the Paleoproterozoic positive carbon isotope excursion: evidence from sulphate evaporites in the ~2.2–2.1 Gyr shallow-marine Lucknow Formation, South Africa. *Terra Nova*, 20, 108–117.
- Schumann, U., & Huntrieser, H. (2007). The global lightning-induced nitrogen oxides source. *Atmospheric Chemistry and Physics*, 7, 3823–3907.
- Schwartz, J. C., Sekowski, C., Haggard, H. M., Pallé, E., & Cowan, N. B. (2016). Inferring planetary obliquity using rotational and orbital photometry. *Mon. Not. R. Astron. Soc.*, 457, 926–938.
- Schwieterman, E. W., Kiang, N. Y., Parenteau, M. N., Harman, C. E., DasSarma, S., Fisher, T. M., Arney, G. N., Hartnett, H. E., Reinhard, C. T., Olson, S. L., Meadows, V. S., Cockell, C. S., Walker, S. I., Grenfell, J. L., Hegde, S., Rugheimer, S., Hu, R., Lyons, T. W. (2018). Exoplanet Biosignatures: A Review of Remotely Detectable Signs of Life. *Astrobiology*, 18, 663–708.
- Schwieterman, E. W., Robinson, T. D., Meadows, V. S., Misra, A., & Domagal-Goldman, S. (2015). Detecting and Constraining N₂ Abundances in Planetary Atmospheres Using Collisional Pairs. *Astrophys. J.*, 810, 57.
- Scott, A. C., & Glasspool, I. J. (2006). The diversification of Paleozoic fire systems and fluctuations in atmospheric oxygen concentration. *Proceedings of the National Academy of Science*, 103, 1086–10865.
- Scott, C., Wing, B. A., Bekker, A., Planavsky, N. J., Medvedev, P., Bates, S. M., Yun, M., & Lyons, T. W. (2014). Pyrite multiple-sulfur isotope evidence for rapid expansion and contraction of the early Paleoproterozoic seawater sulfate reservoir. *Earth and Planetary Science Letters*, 389, 95–104.

- Seager, S., & Sasselov, D. (2000). Theoretical transmission spectra during extrasolar giant planet transits. *The Astrophysical Journal*, 537(2), 916.
- Seager, S., Turnbull, M., Sparks, W., Thomson, M., Shaklan, S. B., Roberge, A., Kuchner, M., Kasdin, N. J., Domagal-Goldman, S., Cash, W., Warfield, K., Lisman, D., Scharf, D., Webb, D., Trabert, R., Martin, S., Cady, E., & Heneghan, C. (2015). The Exo-S Probe Class Starshade Mission. In *Techniques and Instrumentation for Detection of Exoplanets VII*, vol. 9605 of *Proc. SPIE*, (p. 96050W).
- Seager, S., Turner, E. L., Schafer, J., & Ford, E. B. (2005). Vegetation's Red Edge: A Possible Spectroscopic Biosignature of Extraterrestrial Plants. *Astrobiology*, 5, 372–390.
- Segura, A., Krelove, K., Kasting, J. F., Sommerlatt, D., Meadows, V., Crisp, D., Cohen, M., & Mlawer, E. (2003). Ozone Concentrations and Ultraviolet Fluxes on Earth-Like Planets Around Other Stars. *Astrobiology*, 3, 689–708.
- Sellers, W. D. (1969). A Global Climatic Model Based on the Energy Balance of the Earth-Atmosphere System. *Journal of Applied Meteorology*, 8, 392–400.
- Selsis, F., Wordsworth, R. D., & Forget, F. (2011). Thermal Phase Curves of Nontransiting Terrestrial Exoplanets. I. Characterizing Atmospheres. *Astron. Astrophys.*, 532, A1.
- Shaklan, S. B., Noecker, M. C., Glassman, T., Lo, A. S., Dumont, P. J., Kasdin, N. J., Cady, E. J., Vanderbei, R., & Lawson, P. R. (2010). Error Budgeting and Tolerancing of Starshades for Exoplanet Detection. In *Space Telescopes and Instrumentation 2010: Optical, Infrared, and Millimeter Wave*, vol. 7731 of *Proc. SPIE*, (p. 77312G).
- Sheen, A. I., Kendall, B., Reinhard, C. T., Creaser, R. A., Lyons, T. W., Bekker, A., Poulton, S. W., & Anbar, A. D. (2018). A model for the oceanic mass balance of rhenium and implications for the extent of Proterozoic ocean anoxia. *Geochim. Cosmochim. Acta*, 227, 75–95.
- Sheldon, N. D. (2006). Precambrian Paleosols and Atmospheric CO₂ Levels. *Precambrian Research*, 147, 148–155.
- Sheldon, N. D. (2013). Causes and consequences of low atmospheric pCO₂ in the Late Mesoproterozoic. *Chemical Geology*, 362, 224–231.
- Sing, D., Désert, J.-M., Lecavelier Des Etangs, A., Ballester, G., Vidal-Madjar, A., Parmentier, V., Hebrard, G., & Henry, G. (2009). Transit spectrophotometry of the exoplanet hd 189733b. i. searching for water but finding haze with hst nicmos. *Astronomy and Astrophysics*, 505, 891–899.
- Sing, D. K., Fortney, J. J., Nikolov, N., Wakeford, H. R., Kataria, T., Evans, T. M., Aigrain, S., Ballester, G. E., Burrows, A. S., Deming, D., Désert, J.-M., Gibson, N. P., Henry, G. W., Huitson, C. M., Knutson, H. A., Lecavelier Des Etangs, A., Pont, F., Showman, A. P., Vidal-Madjar, A., Williamson, M. H., & Wilson, P. A. (2016). A continuum from clear to cloudy hot-Jupiter exoplanets without primordial water depletion. *Nature*, 529, 59–62.
- Skemer, A. J., Hinz, P. M., Esposito, S., Burrows, A., Leisenring, J., Skrutskie, M., Desidera, S., Mesa, D., Arcidiacono, C., Mannucci, F., Rodigas, T. J., Close, L., McCarthy, D., Kulesa, C., Agapito, G., Apai, D., Argomedo, J., Bailey, V., Boutsia, K., Briguglio, R., Brusa, G., Busoni, L., Claudi, R., Eisner, J., Fini, L., Follette, K. B., Garnavich, P., Gratton, R., Guerra, J. C., Hill, J. M., Hoffmann, W. F., Jones, T., Krejny, M., Males, J., Masciadri, E., Meyer, M. R., Miller, D. L., Morzinski, K., Nelson, M., Pinna, E., Puglisi, A., Quanz, S. P., Quiros-Pacheco, F., Riccardi, A., Stefanini, P., Vaitheeswaran, V., Wilson, J. C., & Xompero, M. (2012). First Light LBT AO Images of HR 8799 bcde at 1.6 and 3.3 μm : New Discrepancies between Young Planets and Old Brown Dwarfs. *Astrophys. J.*, 753, 14.
- Sleep, N. H., & Zahnle, K. (2001). Carbon dioxide cycling and implications for climate on ancient Earth. *J. Geophys. Res.*, 106, 1373–1400.
- Snellen, I. A. G., de Kok, R. J., Le Poole, R., Brogi, M., & Birkby, J. (2013). Finding extraterrestrial life using ground-based high-dispersion spectroscopy. *Astrophys. J.*, 764, 182.
- Som, S. M., Buick, R., Hagadorn, J. W., Blake, T. S., Perreault, J. M., Harnmeijer, J. P., & Catling, D. C. (2016). Earth's air pressure 2.7 billion years ago constrained to less than half of modern levels. *Nature Geoscience*, 9, 448–451.
- Som, S. M., Catling, D. C., Harnmeijer, J. P., Polivka, P. M., & Buick, R. (2012). Air density 2.7 billion years ago limited to less than twice modern levels by fossil raindrop imprints. *Nature*, 484, 359–362.
- Spergel, D., Gehrels, N., Breckinridge, J., Donahue, M., Dressler, A., Gaudi, B., Greene, T., Guyon, O., Hirata, C., Kalirai, J., et al. (2013). Wide-field infrared survey telescope-astronomy focused telescope assets wfirst-afta final report. *arXiv*, arXiv:1305.5422.
- Stam, D. M. (2008). Spectropolarimetric signatures of Earth-like extrasolar planets. *Astron. Astrophys.*, 482, 989–1007.
- Stanton, C. L., Reinhard, C. T., Kasting, J. F., Ostrom, N. E., Haslun, J. A., Lyons, T. W., & Glass, J. B. (2018). Nitrous oxide from chemodenitrification: A possible

- missing link in the proterozoic greenhouse and the evolution of aerobic respiration. *Geobiology*, 16(6), 597–609.
- Stark, C. C., Cady, E. J., Clampin, M., Domagal-Goldman, S., Lismann, D., Mandell, A. M., McElwain, M. W., Roberge, A., Robinson, T. D., Savransky, D., Shaklan, S. B., & Stapelfeldt, K. R. (2016). A Direct Comparison of ExoEarth Yields for Starshades and Coronagraphs. In *Space Telescopes and Instrumentation 2016: Optical, Infrared, and Millimeter Wave*, vol. 9904 of *Proc. SPIE*, (p. 99041U).
- Sterzik, M. F., Bagnulo, S., & Palle, E. (2012). Biosignatures as Revealed by Spectropolarimetry of Earthshine. *Nature*, 483, 64–66.
- Stevenson, K. B. (2016). Quantifying and Predicting the Presence of Clouds in Exoplanet Atmospheres. *Astrophys. J. Lett.*, 817, L16.
- Stevenson, K. B., Harrington, J., Nymeyer, S., Madhusudan, N., Seager, S., Bowman, W. C., Hardy, R. A., Deming, D., Rauscher, E., & Lust, N. B. (2010). Possible thermochemical disequilibrium in the atmosphere of the exoplanet GJ 436b. *Nature*, 464, 1161–1164.
- Stüeken, E. E., Kipp, M. A., Koehler, M. C., Schwieterman, E. W., Johnson, B., & Buick, R. (2016). Modeling pN₂ through Geological Time: Implications for Planetary Climates and Atmospheric Biosignatures. *Astrobiology*, 16, 949–963.
- Suttles, J. T., Green, R. N., Minnis, P., Smith, G. L., Staylor, W. F., Wielicki, B. A., Walker, I., Young, D., Taylor, V., & Stowe, L. (Eds.) (1988). *Angular Radiation Models for Earth-Atmosphere System: Volume 1 - Shortwave Radiation*. NASA Scientific and Technical Information Division: Reference Publication 1184.
- Swain, M. R., Vasisht, G., & Tinetti, G. (2008). The presence of methane in the atmosphere of an extrasolar planet. *Nature*, 452, 329–331.
- Swain, M. R., Vasisht, G., Tinetti, G., Bouwman, J., Chen, P., Yung, Y., Deming, D., & Deroo, P. (2009). Molecular Signatures in the Near-Infrared Dayside Spectrum of HD 189733b. *Astrophys. J. Lett.*, 690, L114–L117.
- Tang, D., Shi, X., Wang, X., & Jiang, G. (2016a). Extremely low oxygen concentration in mid-Proterozoic shallow seawaters. *Precambrian Research*, 276, 145–157.
- Tang, M., Chen, K., & Rudnick, R. L. (2016b). Archean upper crust transition from mafic to felsic marks the onset of plate tectonics. *Science*, 351, 372–375.
- Thomson, D., Rainbird, R. H., Planavsky, N., Lyons, T. W., & Bekker, A. (2015). Chemostratigraphy of the Shaler Supergroup, Victoria Island, NW Canada: A record of ocean composition prior to the Cryogenian glaciations. *Precambrian Research*, 263, 232–245.
- Tian, F., Kasting, J. F., & Zahnle, K. (2011). Revisiting HCN formation in Earth's early atmosphere. *Earth and Planetary Science Letters*, 308, 417–423.
- Tian, F., Toon, O. B., & Pavlov, A. A. (2006). Response to Comment on "A Hydrogen-Rich Early Earth Atmosphere". *Science*, 311, 38b.
- Tian, F., Toon, O. B., Pavlov, A. A., & De Sterck, H. (2005). A Hydrogen-Rich Early Earth Atmosphere. *Science*, 308, 1014–1017.
- Tice, M. M., & Lowe, D. R. (2004). Photosynthetic microbial mats in the 3,416-Myr-old ocean. *Nature*, 431, 549–552.
- Tinetti, G., Meadows, V. S., Crisp, D., Fong, W., Fishbein, E., Turnbull, M., & Bibring, J.-P. (2006). Detectability of Planetary Characteristics in Disk-Averaged Spectra. I: The Earth Model. *Astrobiology*, 6, 34–47.
- Tohver, E., D'Agrella-Filho, M. S., & Trindade, R. I. F. (2006). Paleomagnetic record of Africa and South America for the 1200–500Ma interval, and evaluation of Rodinia and Gondwana assemblies. *Precambrian Research*, 147, 193–222.
- Trainer, M. G., Pavlov, A. A., Curtis, D. B., McKay, C. P., Worsnop, D. R., Delia, A. E., Toohey, D. W., Toon, O. B., & Tolbert, M. A. (2004). Haze Aerosols in the Atmosphere of Early Earth: Manna from Heaven. *Astrobiology*, 4, 409–419.
- Trainer, M. G., Pavlov, A. A., Dewitt, H. L., Jimenez, J. L., McKay, C. P., Toon, O. B., & Tolbert, M. A. (2006). Inaugural Article: Organic haze on Titan and the early Earth. *Proceedings of the National Academy of Science*, 103, 18035–18042.
- Traub, W. A. (2003). The Colors of Extrasolar Planets. In D. Deming, & S. Seager (Eds.) *Scientific Frontiers in Research on Extrasolar Planets*, vol. 294 of *Astronomical Society of the Pacific Conference Series*, (pp. 595–602).
- Traub, W. A., Breckinridge, J., Greene, T. P., Guyon, O., Jeremy Kasdin, N., & Macintosh, B. (2016). Science Yield Estimate with the Wide-Field Infrared Survey Telescope Coronagraph. *Journal of Astronomical Telescopes, Instruments, and Systems*, 2(1), 011020.
- Traub, W. A., & Jucks, K. W. (2002). A Possible Aeronomy of Extrasolar Terrestrial Planets. In M. Mendillo, A. Nagy, & J. H. Waite (Eds.) *Atmospheres in the Solar System: Comparative Aeronomy*, (p. 369). American Geophysical Union.
- Traub, W. A., & Oppenheimer, B. R. (2010). Direct Imaging of Exoplanets. In S. Seager (Ed.) *Exoplanets*, (pp. 111–156). University of Arizona Press, Tucson.

- Turnbull, M. C., Traub, W. A., Jucks, K. W., Woolf, N. J., Meyer, M. R., Gorlova, N., Skrutskie, M. F., & Wilson, J. C. (2006). Spectrum of a Habitable World: Earthshine in the Near-Infrared. *Astrophys. J.*, 644, 551–559.
- Ueno, Y., Yamada, K., Yoshida, N., Maruyama, S., & Isozaki, Y. (2006). Evidence from fluid inclusions for microbial methanogenesis in the early Archaean era. *Nature*, 440, 516–519.
- Ushikubo, T., Kita, N. T., Cavosie, A. J., Wilde, S. A., Rudnick, R. L., & Valley, J. W. (2008). Lithium in Jack Hills zircons: Evidence for extensive weathering of Earth's earliest crust. *Earth and Planetary Science Letters*, 272, 666–676.
- Vázquez, M., Pallé, E., & Rodríguez, P. (2010). *The Earth as a Distant Planet: A Rosetta Stone for the Search of Earth-Like Worlds*. Astronomy and Astrophysics Library. Springer.
- Veevers, J. J., & Powell, C. M. (1987). Late Paleozoic glacial episodes in Gondwanaland reflected in transgressive-regressive depositional sequences in Euramerica. *Geological Society of America Bulletin*, 98, 475.
- Viljoen, M. J., & Viljoen, R. P. (1969). Evidence for the existence of a mobile extrusive peridotitic magma from the Komati Formation of the Overacht Group. *Geological Society of South Africa Special Publications*, 2, 87–112.
- von Paris, P., Hedelt, P., Selsis, F., Schreier, F., & Trautmann, T. (2013). Characterization of Potentially Habitable Planets: Retrieval of Atmospheric and Planetary Properties from Emission Spectra. *Astron. Astrophys.*, 551, A120.
- Walker, J. C. G., Hays, P. B., & Kasting, J. F. (1981). A negative feedback mechanism for the long-term stabilization of Earth's surface temperature. *Journal of Geophysical Research*, 86, 9776–9782.
- Williams, D. M., & Gaidos, E. (2008). Detecting the glint of starlight on the oceans of distant planets. *Icarus*, 195, 927–937.
- Wolf, E. T., & Toon, O. B. (2010). Fractal Organic Hazes Provided an Ultraviolet Shield for Early Earth. *Science*, 328, 1266.
- Wolf, E. T., & Toon, O. B. (2013). Hospitable Archean Climates Simulated by a General Circulation Model. *Astrobiology*, 13, 656–673.
- Wolf, E. T., & Toon, O. B. (2014). Controls on the Archean Climate System Investigated with a Global Climate Model. *Astrobiology*, 14, 241–253.
- Wolfe, J. M., & Fournier, G. P. (2018). Horizontal gene transfer constrains the timing of methanogen evolution. *Nature Ecology & Evolution*.
- Wolff, E., & Spahni, R. (2007). Methane and nitrous oxide in the ice core record. *Philosophical Transactions of the Royal Society of London Series A*, 365, 1775–1792.
- Woolf, N. J., Smith, P. S., Traub, W. A., & Jucks, K. W. (2002). The Spectrum of Earthshine: A Pale Blue Dot Observed from the Ground. *Astrophys. J.*, 574, 430–433.
- Wordsworth, R., & Pierrehumbert, R. (2013). Hydrogen-Nitrogen Greenhouse Warming in Earth's Early Atmosphere. *Science*, 339, 64.
- Wordsworth, R., & Pierrehumbert, R. (2014). Abiotic oxygen-dominated atmospheres on terrestrial habitable zone planets. *The Astrophysical Journal Letters*, 785.
- Wullstein, L. H., & Gilmour, C. M. (1966). Non-enzymatic formation of nitrogen gas. *Nature*, 210, 1150–1151.
- Xiong, J., Fischer, W. M., Inoue, K., Nakahara, M., & Bauer, C. E. (2000). Molecular Evidence for the Early Evolution of Photosynthesis. *Science*, 289, 1724–1730.
- Yan, F., Fosbury, R. A. E., Petr-Gotzens, M. G., Zhao, G., Wang, W., Wang, L., Liu, Y., & Pallé, E. (2015). High-Resolution Transmission Spectrum of the Earth's Atmosphere: Seeing Earth as an Exoplanet Using a Lunar Eclipse. *International Journal of Astrobiology*, 14, 255–266.
- Yang, W., Marshak, A., Várnai, T., & Knyazikhin, Y. (2018). EPIC Spectral Observations of Variability in Earth's Global Reflectance. *Remote Sensing*, 10, 254.
- Young, G. (2001). Paleoproterozoic Huronian basin: product of a Wilson cycle punctuated by glaciations and a meteorite impact. *Sedimentary Geology*, 141, 233–254.
- Young, G. M., Brunn, V. V., Gold, D. J. C., & Minter, W. E. L. (1998). Earth's Oldest Reported Glaciation: Physical and Chemical Evidence From the Archean Mozaan Group (~2.9 Ga) of South Africa. *Journal of Geology*, 106, 523–538.
- Zachos, J., Pagani, M., Sloan, L., Thomas, E., & Billups, K. (2001). Trends, Rhythms, and Aberrations in Global Climate 65 Ma to Present. *Science*, 292, 686–693.
- Zachos, J. C., Dickens, G. R., & Zeebe, R. E. (2008). An early Cenozoic perspective on greenhouse warming and carbon-cycle dynamics. *Nature*, 451, 279–283.
- Zahnle, K. J. (1986). Photochemistry of methane and the formation of hydrocyanic acid (HCN) in the Earth's early atmosphere. *J. Geophys. Res.*, 91, 2819–2834.
- Zahnle, K. J., Claire, M. W., & Catling, D. C. (2006). The loss of mass-independent fractionation in sulfur due to a Paleoproterozoic collapse of atmospheric methane. *Geobiology*, 4, 271–283.

- Zbinden, E. A., Holland, H. D., Feakes, C. R., & Dobos, S. K. (1988). The sturgeon falls paleosol and the composition of the atmosphere 1.1 Ga BP. *Precambrian Research*, 42, 141–163.
- Zerkle, A. L., Claire, M. W., Domagal-Goldman, S. D., Farquhar, J., & Poulton, S. W. (2012). A bistable organic-rich atmosphere on the Neoarchaeon Earth. *Nature Geoscience*, 5, 359–363.
- Zhao, M., Reinhard, C. T., & Planavsky, N. (2018). Terrestrial methane fluxes and Proterozoic climate. *Geology*, 46, 139–142.
- Zugger, M. E., Kasting, J. F., Williams, D. M., Kane, T. J., & Philbrick, C. R. (2010). Light Scattering from Exoplanet Oceans and Atmospheres. *Astrophys. J.*, 723, 1168–1179.
- Zugger, M. E., Kasting, J. F., Williams, D. M., Kane, T. J., & Philbrick, C. R. (2011). Searching for Water Earths in the Near-Infrared. *Astrophys. J.*, 739, 12.